

---

# Initial and final state effects in attosecond photoemission delays from W(110)

Stephan Heinrich

---



München 2021



---

# **Initial and final state effects in attosecond photoemission delays from W(110)**

**Stephan Heinrich**

---

Dissertation  
an der Fakultät für Physik  
der Ludwig–Maximilians–Universität  
München

vorgelegt von  
Stephan Heinrich  
aus Wasserburg am Inn

München, den 02.03.2021

Erstgutachter: Prof. Dr. Ulf Kleineberg

Zweitgutachter: Prof. Dr. Reinhard Kienberger

Tag der mündlichen Prüfung: 16.04.2021

## Zusammenfassung

Attosekunden-Photoelektronenspektroskopie (PES) erlaubt das Beobachten der Elektronendynamik in Gasen, Festkörpern und Molekülen auf ihrer natürlichen Zeitskala. Spektrale Verbreiterung durch Raumladungseffekte begrenzte bisher die Energieauflösung oder den nutzbaren Photoelektronenfluss bei Attosekunden-PES-Experimenten an Festkörpern. Hohe Pulswiederholungsraten im Megahertz-Bereich können dieses Problem lösen, da der durchschnittliche Photoelektronenfluss auf viele Laserpulse verteilt wird. Herkömmliche Lasersysteme liefern allerdings bei diesen Pulswiederholungsraten nicht die nötige Pulsenergie für die Erzeugung hoher Harmonischer (HHG).

Aus diesem Grund wurde eine Quelle für Attosekundenpulszüge entwickelt, bei der hohe Harmonische in einem Überhöhungsresonator erzeugt werden und die mit bis zu  $60 \mu\text{W}$  Ausgangsleistung im extrem ultravioletten (XUV) Spektralbereich bei bis zu  $100 \text{ eV}$  Photonenenergie und  $18.4 \text{ MHz}$  neue Standards für HHG bei hohen Repetitionsraten setzt. Die einzigartigen Eigenschaften dieser XUV-Quelle wurden im Rahmen dieser Arbeit genutzt, um die zeitlichen Abläufe der Photoemission zum ersten Mal bei MHz Repetitionsrate zu untersuchen.

Zu diesem Zweck wurden PES-Experimente an einem W(110) Kristall durchgeführt. Es wurde experimentell bestätigt, dass trotz der hohen Photoelektronenzählrate von bis zu  $10^6 \text{ 1/s}$  keine Raumladungs-Effekte die PES-Messungen beeinträchtigen. Die Kombination aus hoher Energieauflösung und winkelaufgelöster Photoelektronendetektion ermöglichte das Unterscheiden von *sp*- und *d*-Bändern in den Photoelektronenspektren. Zeitaufgelöste Messungen offenbarten eine Verzögerung von  $39 \pm 18 \text{ as}$  für Photoemission aus *d*-Bändern im Vergleich zu *sp*-Bändern. Dies ist in Übereinstimmung mit theoretischen Vorhersagen und Messungen an Gasatomen und tiefer liegenden Zuständen in Festkörpern.

Desweiteren ermöglichten die hohen Photonenenergien der HHG-Quelle die ersten Messungen mit Attosekundenpulszügen, bei denen Photoemissionszeiten von Valenzelektronen mit denen von stark gebundenen inneren Elektronen referenziert wurden. Dadurch konnte bei W(110) ein starker Anstieg der Photoemissionszeit von  $148 \pm 40 \text{ as}$  bei  $62 \text{ eV}$  kinetischer Energie nachgewiesen werden. Dieses Phänomen konnte mithilfe eines theoretischen Modells zum Einfluss von elektronischen Endzuständen reproduziert und erklärt werden. Breitbandige zeitaufgelöste Messungen wiesen einen weiteren Anstieg bei  $43 \text{ eV}$  kinetischer Energie nach, der ebenfalls mit dem entwickelten Modell übereinstimmt.

Die hohe Energieauflösung, die winkelaufgelöste Detektion und die Möglichkeit, innere Elektronenzustände anzuregen, sind zudem ideal um verschiedene Festkörper zu unterscheiden. Dadurch konnte eine relative Verzögerung von  $242 \pm 64 \text{ as}$  für Photoemission von Wolfram gegenüber Wolframcarbid beobachtet werden. Die Abweichung wird einem geometrisch bedingten Unterschied in der mittleren Emissionstiefe der Elektronen zugeschrieben.

Die Erkenntnisse aus dieser Arbeit unterstreichen die Wichtigkeit von Anfangs- und Endzuständen für Photoemission und Elektronentransport in Festkörpern. Dies ebnet den Weg für die Untersuchung und das Verständnis von Ladungsspeicherung und -transport in neuartigen Materialien und (opto-) elektronischen Elementen auf atomarer Größenordnung.



## Abstract

Attosecond photoemission spectroscopy (PES) enables the observation of electron dynamics in gases, solids and molecules on their natural timescale. So far, space-charge induced spectral distortions severely limited the energy resolution or the photoelectron flux of attosecond PES experiments on solids. High pulse repetition rates in the MHz regime can overcome this dilemma because the average flux of photoelectrons is distributed over millions of laser shots per second. However, conventional laser systems at this repetition rate lack the necessary pulse energies for high harmonic generation (HHG).

Therefore, an enhancement-cavity based HHG source was developed, which sets new standards for high-repetition rate HHG with up to 60  $\mu\text{W}$  power of extreme ultraviolet light and photon energies exceeding 100 eV at 18.4 MHz pulse repetition rate. Within the scope of this thesis the unique characteristics of this system were employed to investigate the photoemission timing from solids in the first MHz attosecond PES experiments.

For this purpose, photoelectron spectroscopy experiments on a W(110) crystal have been conducted. At photoelectron count rates of up to  $10^6$  1/s it was experimentally confirmed that no space-charge effects impair the PES measurements. The high energy resolution in combination with angle-resolved photoelectron detection allowed for distinguishing the contributions from *sp* and *d* bands in the photoelectron spectra and revealed a photoemission delay of  $39 \pm 18$  as between them. This is in agreement with theoretical predictions and similar experiments on gas atoms and core states in solids.

Furthermore, the high photon energies provided by the source allowed for the first core-state referenced photoemission delay measurement on a solid utilizing attosecond pulse trains. By this method, a surge in photoemission delay of  $148 \pm 40$  as at 62 eV final electron kinetic energy in W(110) was found. It could be identified as a final-state induced delay and reproduced with an electron transport time model, which relies on the final-state group velocities. Broadband measurements at lower photon energies revealed another final-state induced increase in photoemission delay around 43 eV, which also is in agreement with the model.

The high energy resolution in combination with angle-resolved photoelectron detection and the ability to access deeply bound states are also ideal for distinguishing different materials. By these means a relative photoemission delay of  $242 \pm 64$  as from tungsten with respect to tungsten carbide was found. The delay is attributed to a geometrically induced difference in mean emission depth.

The findings presented in this thesis underscore the importance of both initial and final bands for photoemission and electron transport timing in solid materials. This paves the way to study and understand the process of charge storage and transport in novel materials and (opto-) electronic devices which approach atomic scales.



# Table of Contents

<b>Zusammenfassung</b>	<b>v</b>
<b>Abstract</b>	<b>vii</b>
<b>Table of Contents</b>	<b>ix</b>
<b>List of Figures</b>	<b>xiii</b>
<b>List of Publications</b>	<b>xv</b>
<b>1 Introduction</b>	<b>1</b>
<b>2 Theoretical background</b>	<b>5</b>
2.1 Ultrashort laser pulses . . . . .	5
2.1.1 Laser pulses in time and frequency . . . . .	5
2.1.2 Optical frequency combs . . . . .	6
2.2 High harmonic generation . . . . .	9
2.2.1 The three-step model of HHG . . . . .	9
2.2.2 HHG cutoff energy . . . . .	9
2.2.3 The generation of attosecond pulses . . . . .	11
2.2.4 Phase-matched HHG . . . . .	11
2.2.5 HHG at MHz repetition rate . . . . .	13
2.3 Enhancement cavities for HHG . . . . .	13
2.3.1 Power enhancement . . . . .	13
2.3.2 Intensity clamping in HHG cavities . . . . .	15
2.3.3 Design of a HHG enhancement cavity . . . . .	16
2.4 Attosecond photoelectron spectroscopy . . . . .	17
2.4.1 The photoemission process . . . . .	17
2.4.2 Laser dressed photoionization . . . . .	19
2.4.3 The attosecond streak camera . . . . .	22
2.4.4 The RABBITT-technique . . . . .	23
2.4.5 Attosecond streaking and RABBITT compared . . . . .	25

<b>3</b>	<b>Experimental setup</b>	<b>29</b>
3.1	Laser system . . . . .	29
3.2	Enhancement-cavity based high harmonic generation . . . . .	31
3.2.1	Enhancement cavity setup . . . . .	32
3.2.2	Intra-cavity high harmonic generation . . . . .	34
3.3	Attosecond beamline . . . . .	37
3.3.1	Vacuum and differential pumping . . . . .	37
3.3.2	Beam diagnostics and filter . . . . .	39
3.3.3	XUV transmission and reflectivity losses . . . . .	41
3.4	ARPES chamber . . . . .	42
3.4.1	Chamber setup overview . . . . .	42
3.4.2	Coaxial foil filter . . . . .	44
3.4.3	Double mirror interferometer . . . . .	45
3.4.4	Angle-resolved time-of-flight photoelectron detection . . . . .	49
3.4.5	Tungsten crystal preparation . . . . .	51
3.5	Measurement routine . . . . .	53
<b>4</b>	<b>Methodology - RABBITT analysis and illustration</b>	<b>55</b>
4.1	Spectrogram illustration . . . . .	55
4.2	Sideband delay evaluation and error bars . . . . .	56
4.3	Sideband delays introduced by XUV optics . . . . .	59
4.4	RABBITT Fourier analysis . . . . .	59
<b>5</b>	<b>Initial-state induced photoemission delays in tungsten</b>	<b>63</b>
5.1	Space-charge free photoemission spectroscopy . . . . .	63
5.2	Tungsten electronic band structure . . . . .	65
5.2.1	Brillouin zone and photoelectron detection geometry . . . . .	66
5.2.2	Density of states . . . . .	67
5.3	Intra-valence band referenced RABBITT . . . . .	69
5.3.1	XUV spectra for valence band photoemission spectroscopy . . . . .	69
5.3.2	Distinguishing photoemission from tungsten <i>sp</i> and <i>d</i> bands . . . . .	71
5.3.3	Initial state photoemission delays . . . . .	72
5.3.4	Excitation-dependent RABBITT spectrograms . . . . .	75
<b>6</b>	<b>Final-state induced photoemission delays in tungsten</b>	<b>77</b>
6.1	Final band group velocities in tungsten . . . . .	77
6.2	Tungsten core state RABBITT . . . . .	79
6.3	Resonant RABBITT sideband delays . . . . .	81
6.3.1	Final state photoemission delays . . . . .	83
6.3.2	Tungsten $4f$ doublet sideband overlap . . . . .	84
6.4	Photoemission delays in tungsten carbide . . . . .	88

## **TABLE OF CONTENTS**

---

**xi**

**7 Conclusion and outlook**

**91**

**References**

**93**

**Danksagung**

**111**



# List of Figures

2.1	The spectral phase of ultrashort laser pulses . . . . .	7
2.2	An optical frequency comb . . . . .	8
2.3	Three-step model of HHG . . . . .	10
2.4	Cavity power enhancement resonances . . . . .	14
2.5	Enhancement cavity intensity clamping . . . . .	16
2.6	Three-step model of photoemission . . . . .	19
2.7	Simulated attosecond streaking and RABBITT spectrogram . . . . .	21
2.8	Attosecond streak camera working principle . . . . .	23
2.9	RABBITT working principle . . . . .	24
3.1	Laser system setup . . . . .	30
3.2	Enhancement cavity setup . . . . .	33
3.3	HHG target in operation . . . . .	34
3.4	XUV spectra and photon flux . . . . .	36
3.5	Attosecond beamline setup . . . . .	38
3.6	XUV absorption and reflectivity losses along beampath . . . . .	42
3.7	ARPES chamber setup . . . . .	43
3.8	Coaxial foil filter/pellicle . . . . .	45
3.9	Double mirror IR focus profile and temporal overlap . . . . .	47
3.10	Double mirror interferometer drifts . . . . .	48
3.11	Time-of-flight photoelectron detection at MHz repetition rate . . . . .	50
3.12	Tungsten crystal annealing . . . . .	51
3.13	Sample crystal temperature during measurement . . . . .	52
4.1	RABBITT-spectrogram background subtraction . . . . .	56
4.2	RABBITT sideband delay evaluation . . . . .	58
4.3	XUV-optics induced sideband delays . . . . .	60
4.4	RABBITT Fourier analysis . . . . .	61
5.1	Space-charge effects in photoelectron spectra . . . . .	65
5.2	First Brillouin zone of a tungsten bcc crystal and angle acceptance . . . . .	67
5.3	Tungsten band structure and density of states . . . . .	68
5.4	Photoelectron spectrum as convolution of XUV and DOS . . . . .	69

---

5.5	XUV spectra and sideband intensities for shifted harmonics . . . . .	70
5.6	Static tungsten valence band photoelectron spectroscopy . . . . .	72
5.7	Tungsten valence band angle-resolved photoemission spectroscopy . . . . .	73
5.8	Intra-valence-band RABBITT delays . . . . .	74
5.9	Valence band RABBITT with different excitation spectra . . . . .	76
6.1	Tungsten final state band structure and group velocity . . . . .	78
6.2	Photoelectron and XUV spectrum for neon HHG . . . . .	80
6.3	Tungsten $4f$ RABBITT sideband delays . . . . .	82
6.4	Intra-sideband delay shift near a final state resonance . . . . .	84
6.5	Fourier delay fit in $4f$ -doublet RABBITT . . . . .	86
6.6	Tungsten carbide photoemission delays . . . . .	89

# List of Publications

## Journal articles

- **S. Heinrich**<sup>\*</sup>, T. Saule<sup>\*</sup>, M. Högner, Y. Cui, V. S. Yakovlev, I. Pupeza, and U. Kleineberg, “Attosecond intra-valence band dynamics and resonant-photoemission delays in W(110)”, manuscript submitted for publication (2021).
- M. Högner, T. Saule, **S. Heinrich**, N. Lilienfein, D. Esser, M. Trubetskov, V. Pervak, and I. Pupeza, “Cavity-enhanced noncollinear high-harmonic generation”, *Optics Express*, 27(14), 19675 - 19691 (2019).
- T. Saule<sup>\*</sup>, **S. Heinrich**<sup>\*</sup>, J. Schötz, N. Lilienfein, M. Högner, O. DeVries, M. Plötner, J. Weitenberg, D. Esser, J. Schulte, P. Rußbüldt, J. Limpert, M. Kling, U. Kleineberg and I. Pupeza, “High-flux ultrafast extreme-ultraviolet photoemission spectroscopy at 18.4 MHz pulse repetition rate”, *Nature Communications*, 10, 458 (2019).
- A. Guggenmos, Y. Cui, **S. Heinrich** and U. Kleineberg, “Attosecond Pulse Shaping by Multilayer Mirrors”, *Applied Sciences*, 8(12), 2503 (2018).

## Conference papers

- **S. Heinrich**, T. Saule, J. Schötz, N. Lilienfein, M. Högner, O. de Vries, M. Plötner, J. Weitenberg, D. Esser, J. Schulte, P. Russbueldt, J. Limpert, M. Kling, U. Kleineberg, and I. Pupeza, “Ultrafast Extreme-Ultraviolet Photoemission Spectroscopy at 18.4 MHz”, *Optical Society of America: Conference on Lasers and Electro-Optics Europe*, cg\_9\_4 (2019).
- **S. Heinrich**, T. Saule, M. Högner, I. Pupeza, and U. Kleineberg, “Attosecond Photoemission Spectroscopy at High Photon Energies and MHz Repetition Rate”, *Optical Society of America: Frontiers in Optics*, JTu4A.25 (2019).
- **S. Heinrich**, A. Guggenmos, F. Apfelbeck, M. Stanislawski, J. Schmidt, and U. Kleineberg, “(Angle Resolved) Photoemission Spectroscopy Utilizing Attosecond Pulse Trains in Argon and Tungsten”, *Optical Society of America: Frontiers in Optics*, FTh2B.3 (2017).

---

<sup>\*</sup> authors contributed equally

- A. Guggenmos, J. Schmidt, **S. Heinrich**, B. Nickel, F. Krausz, and U. Kleineberg, “Multi-layer Mirrors for VUV-XUV Attosecond Pump-Probe Experiments”, *Optical Society of America: Frontiers in Optics*, FM3A.3 (2015).

# Chapter 1

## Introduction

The advent of attosecond metrology at the beginning of this century pushed the limits of the observable to the natural timescales of electron motion. It traditionally relies on the generation of sub-femtosecond light pulses - mostly in the extreme ultraviolet (XUV) spectral range - by means of high harmonic generation (HHG) [1,2]. It was initiated almost simultaneously by two experiments for the characterization of attosecond pulse trains (APT) [3] and isolated attosecond pulses (IAP) [4] and went on to the investigation of electron dynamics in gas atoms [5–7]. Another milestone of attosecond metrology was the first photoemission delay measurement on a solid material in 2007 by Cavalieri et al. [8] which found that photoemission is not an instantaneous process but takes a different amount of time for valence band and deeper bound electronic core states. This observation was attributed to the transport time of the electrons within the solid [8,9]. Because absolute timing information cannot be extracted directly from attosecond pump-probe experiments, referencing photoemission from different initial states or materials has since then become a standard approach in attosecond physics [10–15].

Subsequently, the temporal accuracy of these measurements has been pushed to the zepto-second regime [16] and ever shorter IAPs down to a pulse duration of 43 as have been generated and characterized [17–20]. Intrinsically, the brevity of these pulses comes with a very broad spectrum in the frequency domain, with bandwidths of up to several tens of electronvolts. This precludes applications, where high energy resolution is required, such as distinguishing closely spaced final or initial states or measurements resolving the dispersion relations of solids.

Contrary to isolated attosecond pulses, attosecond pulse trains consist of well-separated high harmonics of typically only a few hundred meV spectral width and this substructure can enable measurements with meV-energy and attosecond time resolution at the same time. Therefore, APTs can resolve features that could not be observed with isolated attosecond pulses [13].

However, there is another serious obstacle for attosecond photoelectron spectroscopy (PES) measurements with high energy resolution, namely space-charge effects. Photoelectrons released by a laser pulse interact with each other via the Coulomb force which leads to shifts and spectral broadening of the spectra and can seriously impair the energy resolution [21–23]. Although space-charge effects can be mitigated by emitting only a few photoelectrons per laser

pulse, this comes at the cost of flux and therefore either unpractically long measurement times or a lower signal-to-noise ratio and reduced measurement precision.

To combine high average photoelectron flux and few released electrons per pulse, high pulse repetition rates are the obvious choice. However, high repetition rates at fixed average laser power result in low pulse energy, which is highly unfavorable for driving a nonlinear process like HHG.

Furthermore, the generation of attosecond pulse trains requires longer laser pulses than used for the generation of isolated attosecond pulses. Longer pulses make it significantly more challenging to reach the high laser peak intensities which are necessary for the generation of attosecond pulse trains with photon energies exceeding 40 eV, particularly at a pulse repetition rate with an acceptable amount of space-charge broadening. This prevents the access to deeply bound states in APT-based attosecond PES experiments, as it is desirable for self-referencing photoemission delay measurements with deeper bound electronic core states.

To overcome this dilemma, a novel type of HHG source was developed: Intracavity HHG offers high XUV photon flux at high pulse repetition rates and has now reached a maturity which allows for application in attosecond photoelectron spectroscopy [24, 25]. Whereas typical single-pass HHG systems have to operate at a repetition rate below 100 kHz to be able to reach the necessary pulse energies for efficient HHG, cavity-enhanced HHG relies on the enhancement of a laser pulse in a passive resonator, which allows for high laser pulse energies at multi-MHz pulse repetition rates and results in high XUV flux. Because the average flux of a MHz-HHG source is distributed over millions of pulses per second, only few photoelectrons are emitted per pulse. This enables quasi-space-charge free measurements with abundant statistics in comparably short measurement time.

In this work, the problem of achieving simultaneous high energy and time resolution at high flux and high photon energies are overcome in the first attosecond photoelectron spectroscopy experiment at MHz repetition rate by using an enhancement-cavity based HHG source. Up to  $10^6$  photoelectrons per second emitted from a tungsten (110) crystal were detected with a time-of-flight (ToF) electron spectrometer at practically space-charge free experimental conditions. The high flux enables the acquisition of photoelectron spectrograms which allow for photoemission delay measurements with an accuracy of a few attoseconds within an acquisition time of tens of minutes. Combined with the angular resolution offered by the electron spectrometer, different initial states within the tungsten valence band were identified and their relative photoemission delay was determined from the measurements.

Moreover, 14 years after the above-mentioned first core-state referenced photoemission delay measurement on a solid material was demonstrated with isolated attosecond pulses [8], this has now been achieved for the first time with attosecond pulse trains within the scope of this thesis, thanks to XUV photon energies of up to more than 100 eV. The high energy resolution of the APT-based approach made it possible to observe final-state related photoemission delays and a theoretical concept based on the group-velocity dependent photoelectron transport time was elaborated to explain this effect. Furthermore, different tungsten compounds could be distinguished by measuring the chemical shift of the electronic core-states and their relative photoemission timing was investigated.

The outline of this thesis is as follows: First, an introduction to the necessary theoretical background about ultrashort laser pulses, high harmonic generation, enhancement cavities and attosecond photoemission spectroscopy is provided. Special emphasis is placed on the similarities and differences between time-resolved photoelectron spectroscopy experiments with isolated attosecond pulses and attosecond pulse trains. Second, an overview over the experimental setup which was used for the measurements presented in this thesis is given. This includes the oscillator and laser amplifier system, the enhancement cavity and intra-cavity HHG setup, the attosecond beamline, which was set up in the context of this work, and the photoelectron spectroscopy setup. Next, the experimental results including the photoemission experiments on the tungsten valence band and  $4f$  core electronic states are presented as well as the theoretical studies conducted for their interpretation. Finally, the thesis is concluded by an outlook on potential future improvements and continuative photoelectron spectroscopy experiments, which could contribute to further strengthen and deepen our understanding of electronical properties and dynamics of solids.



# Chapter 2

## Theoretical background

This chapter provides the necessary theoretical background for the understanding of this thesis. First, an introduction to the theory of ultrashort laser pulses is given. Next, the fundamentals of high harmonic generation and enhancement cavities and the chances and challenges of combining them will be discussed. Furthermore, the principles of attosecond photoelectron spectroscopy utilizing isolated attosecond pulses and attosecond pulse trains will be reviewed and compared.

### 2.1 Ultrashort laser pulses

In contrast to continuous-wave operation, pulsed lasers enable experiments with adjustable pump-probe delay for the observation of time-dependent processes. Moreover, the full average laser output power is concentrated within the pulses which leads to an increase of peak powers and intensities by several orders of magnitude. Both these properties are crucial for attosecond physics and the nonlinear process of HHG.

#### 2.1.1 Laser pulses in time and frequency

Ultrashort laser pulses can be realized by creating a suitable fixed phase relation between the optical frequencies in a laser resonator, which supports a broad bandwidth. In such a mode locked laser interference between the longitudinal laser modes gives rise to laser pulses [26,27].

A laser pulse can be fully described either as electric field in time  $E(t)$  or in the frequency domain  $F(\omega)$ . Both representations are related to each other by Fourier transform [28, p. 250]:

$$E(t) = \frac{1}{2\pi} \int_{-\infty}^{+\infty} F(\omega) e^{i\omega t} \quad (2.1)$$

$$F(\omega) = \int_{-\infty}^{+\infty} E(t) e^{i\omega t} \quad (2.2)$$

Although the time domain seems to be more intuitive, oftentimes it is more useful to use the frequency representation. It is complex-valued and can be decomposed in an absolute value and a phase:

$$F(\omega) = \sqrt{S(\omega)} e^{i\varphi(\omega)} \quad (2.3)$$

Here,  $S(\omega) = |F(\omega)|^2$  denotes the power spectrum and  $\varphi(\omega)$  the spectral phase. The power spectrum is experimentally easily accessible, for example by means of a dispersive prism. The spectral phase is usually more difficult to obtain and can be determined by interference or derived from field-resolved measurements in the time domain.

Because the frequency dependency of  $\varphi(\omega)$  over the bandwidth of a laser pulse is usually comparably low, it is commonly expanded into a Taylor series around the central frequency  $\omega_0$  of the spectrum [29, p. 120]:

$$\varphi(\omega) = \varphi(\omega_0) + \varphi'(\omega_0) \cdot (\omega - \omega_0) + \varphi''(\omega_0) \cdot \frac{(\omega - \omega_0)^2}{2} + \mathcal{O}((\omega - \omega_0)^3) \quad (2.4)$$

The first derivative of the spectral phase  $\varphi' = d\varphi/d\omega$  is the group delay and  $\varphi'' = d^2\varphi/d\omega^2$  the group delay dispersion (GDD). Higher order terms can be neglected in many cases, but become more important the shorter and more broadband a pulse is.

The effects of the different phase terms on the temporal pulse shape are illustrated in Fig. 2.1: A constant phase offset changes the phase relation between field oscillations and temporal envelope and is therefore called carrier-envelope phase (CEP). A linear phase shifts the pulse in time but the envelope remains unchanged. The quadratic spectral phase of the GDD leads to a symmetric broadening of the pulse in the time domain with a linearly changing frequency which is often referred to as chirp. The more broadband a laser pulse is, the stronger is the effect of nonlinear spectral phase terms.

The minimum laser pulse duration for a given spectrum is hence achieved with a linear spectral phase. This bandwidth limit of a laser pulse can directly be related to its spectral width for a specific envelope shape by means of the time-bandwidth product. For a Gaussian pulse it is [28]:

$$\tau \cdot \Delta\omega = 2.77 \quad (2.5)$$

Here,  $\tau$  and  $\Delta\omega$  denote the full width at half-maximum (FWHM) of the laser pulse in the time and frequency domain.

The spectral phase of a laser pulse can for example be altered by propagation through a medium like glass or air or by reflection on so-called chirped mirrors which are designed to exhibit different optical path lengths for different frequencies. Pairs of prisms or optical gratings can also be used to manipulate the spectral phase.

### 2.1.2 Optical frequency combs

So far, a single isolated laser pulse has been treated. In practice, a laser generates a train of laser pulses at a certain pulse repetition frequency, which is dictated by the laser resonator. In

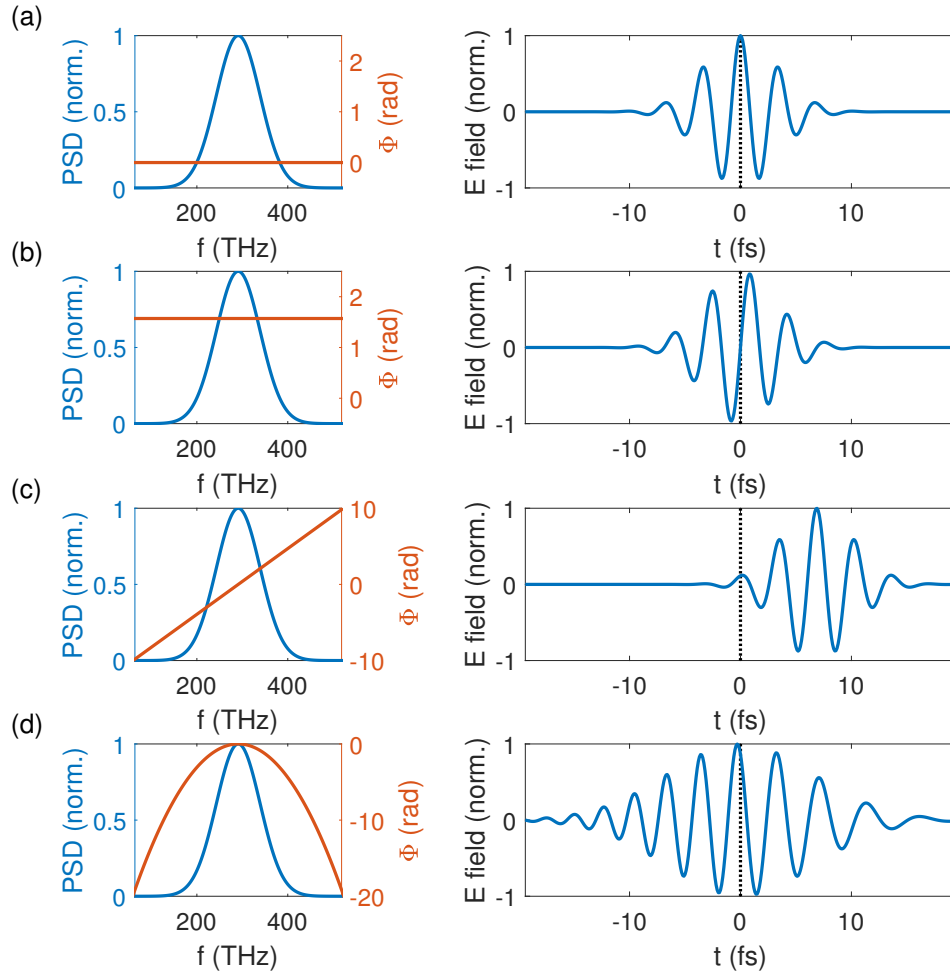


Figure 2.1: Laser pulses with identical intensity spectrum but different spectral phases (left panel) and the resulting temporal pulse shape (right panel). The spectral phases are **a)** zero, **b)** constant  $\pi/2$ , **c)** linear and **d)** quadratic.

the case of a standing-wave cavity the pulse repetition rate is [29, p. 325]:

$$f_{\text{rep}} = \frac{c}{2nL} \quad (2.6)$$

Here,  $n$  and  $L$  denote the refractive index and the length of the resonator and  $c$  the speed of light.

In a laser pulse train, the CEP usually changes from pulse to pulse by a certain carrier-envelope offset phase  $\Delta\phi_{\text{CEO}}$  due to intracavity dispersion and nonlinearities (Fig. 2.2a). This means, that a specific CEP reoccurs with a certain frequency [30]:

$$f_{\text{ceo}} = \frac{\Delta\phi_{\text{CEO}}}{2\pi} f_{\text{rep}} \quad (2.7)$$

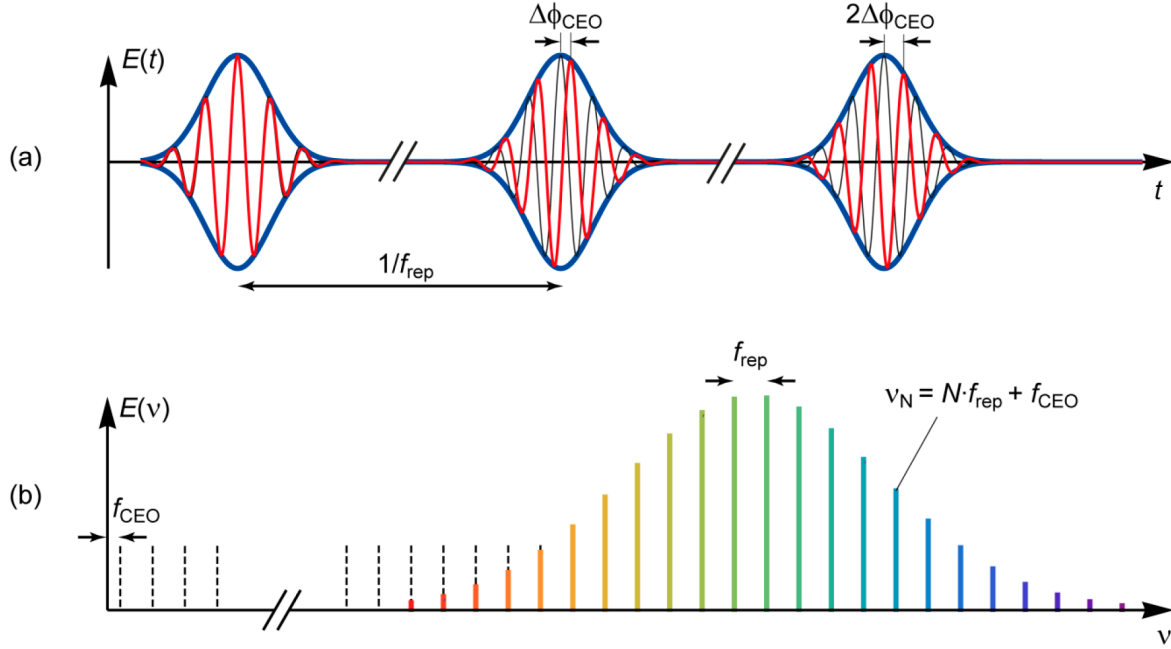


Figure 2.2: **a)** The carrier-envelope phase of a laser pulse train changes by an offset of  $\Delta\Phi_{\text{ceo}}$  from pulse to pulse. **b)** In the frequency domain a train of laser pulses consists of a set of comb lines under a spectral envelope. The comb frequencies are multiples of the pulse repetition frequency  $f_{\text{rep}}$  plus the carrier-envelope offset frequency which is directly related to the CEP slippage in the time domain by  $f_{\text{ceo}} = \Delta\Phi_{\text{ceo}}/2\pi \cdot f_{\text{rep}}$ . Figure taken from Ref. [31] under the terms of the [Creative Commons Attribution 4.0 International License](#).

From the Fourier transform of a train of laser pulses with  $f_{\text{rep}}$  repetition rate, it follows, that the spectrum of the pulse train is not continuous but consists of a comb of closely spaced lines separated by  $f_{\text{rep}}$ . In a more intuitive picture, this can also be explained by the resonance condition of the laser resonator which demands for longitudinal modes that the cavity length must be a multiple of the resonant wavelengths [29, p. 204].

The frequencies of the comb lines are given by the following formula [30]:

$$f_n = n \cdot f_{\text{rep}} + f_{\text{ceo}} \quad (2.8)$$

Here,  $n$  denotes a (large) integer. A frequency comb is illustrated in Fig. 2.2b. The  $f_{\text{ceo}}$  of a laser pulse train can be experimentally determined by generating a beatnote signal between a frequency of the fundamental laser pulse and a frequency-doubled version of the pulse [30, 32]. By precise dispersion control within a laser resonator, this value can be set to a specific value. For  $f_{\text{ceo}} = 0$  the laser pulse train is CEP-stable and the electric field of all pulses is identical.

## 2.2 High harmonic generation

High harmonic generation from gas atoms was first observed in 1987 [2] and has since then become an invaluable tool for the table-top generation of coherent light in the XUV and soft X-ray spectral range. Its applications comprise for example high resolution imaging [33–35], XUV spectroscopy [36,37], high resolution lithography [38] and attosecond physics [3–5,12–15]. In this section, the generation of attosecond pulses by means of HHG will be discussed.

### 2.2.1 The three-step model of HHG

Shortly after the first high harmonics had been generated in gas, Corkum et al. developed an intuitively understandable three-step-model of the process [39]. To generate high harmonics in a gaseous medium its atoms have to be exposed to an oscillating electric field which is of comparable magnitude to the field seen by the bound electrons. These conditions can be created by tightly focusing a beam of ultrashort laser pulses of high peak power in a gas jet. Usually, noble gas atoms are used for HHG because they have the highest ionization potentials which allow for the highest photon energies.

In the first step, the laser electric field deforms the potential of the gas atoms to a point, where the lowest bound electrons can tunnel through the Coulomb barrier (Fig. 2.3a) which typically requires pulse peaks intensities of  $\sim 10^{14}$  W/cm<sup>2</sup>.

After the electron has left the atom, it is fully exposed to the laser field which accelerates it away from the parent ion in the second step of the process. However, the direction of the electric field will inverse after around a quarter of an optical period after the emission and the free electron wave packet is first decelerated and then accelerated back towards the parent ion.

Its exact moment of emission determines the trajectory of the released electron and when and if there is a possibility of a recollision of the electron with its parent ion in the third step of the model (Fig. 2.3b). The final electron kinetic energy, which is acquired during the propagation, and the atom ionization potential determine the energy of the photon, which is emitted upon recombination. While the maximum kinetic energy is realized by a single trajectory associated to a specific time of emission of the electron, for all lower kinetic energies there are two possible trajectories commonly referred to as long and short trajectory (Fig. 2.3c).

### 2.2.2 HHG cutoff energy

The cutoff for the highest generated HHG photon energy can be derived directly from the electron trajectories in the laser electric field (Fig. 2.3c). The maximum possible emitted HHG photon energy is [39,40]:

$$E_{\text{cutoff}} = I_p + 3.17 U_p = I_p + 3.17 \cdot I_{\text{IR}} \lambda^2 \cdot \frac{e^2}{8 \pi^2 c^3 \epsilon_0 m_e} \quad (2.9)$$

Here,  $I_p$  denotes the ionization potential of the gas atoms and  $U_p$  the ponderomotive potential of the laser pulse. The latter is proportional to the maximum laser intensity  $I_{\text{IR}}$  and the

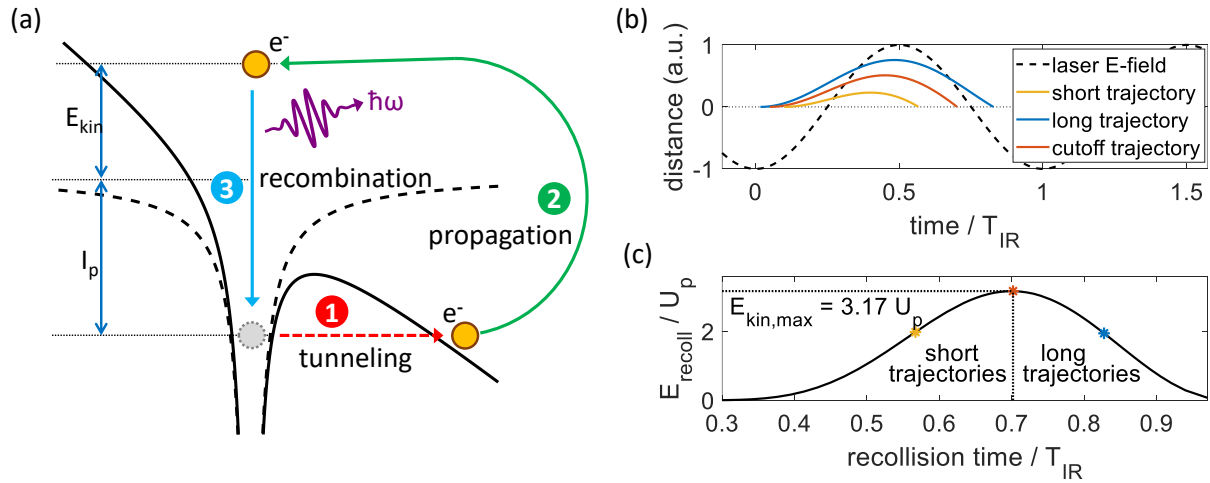


Figure 2.3: **a)** The three-step model of high harmonic generation. In the first step, a strong external electric field deforms the atomic potential such that an electron can tunnel through the potential wall. The electron is accelerated by the electric field, first away from and then back towards the parent ion. In the third step, the electron recombines with the ion and the released kinetic and potential energy is emitted as a XUV photon. **b)** Electrons are emitted around the maximum of the laser field strength. Depending on the exact moment of emission, the electron trajectory can take different routes and the moment of recombination and the energy of the emitted photon vary. **c)** Kinetic energy as function of the time of recollision. The maximum kinetic energy at the moment of recollision is  $3.17 U_p$  (ponderomotive potential). For lower kinetic energies there are two possible trajectories (long and short).

square of the wavelength  $\lambda$  and includes a number of physical constants (electron charge  $e$  and mass  $m_e$ , speed of light  $c$  and vacuum permittivity  $\epsilon_0$ ). Increasing the HHG photon energy can hence be achieved by longer wavelengths or utilizing a gas with a higher ionization potential. Another approach of extending the cutoff is multi-color excitation by few-cycle pulses ranging from the visible to the mid-IR [41, 42].

Argon and neon are widely used as HHG gas and only helium has a higher ionization potential but this comes at significantly lower photon flux, which also applies to longer wavelengths. Studies have shown, that the conversion efficiency of HHG scales with  $\lambda^{-5}$  to  $\lambda^{-6}$  [43–45] due to the reduced recollision probability for electrons with longer trajectories and higher kinetic energy.

The laser intensity  $I_{IR}$  could be increased by tighter focusing at fixed laser power. However, this cannot be pushed beyond a certain limit without losing photon flux due to reduced phase-matching (Section 2.2.4).

### 2.2.3 The generation of attosecond pulses

The tunneling probability of bound electron in the first step of the three step model depends highly on the electrical field strength and strong-field ionization occurs therefore predominantly around the maxima of the strongest field oscillations. Therefore, high-energy photons are emitted only within a fraction of a cycle of the driving field (e.g. 3.4 fs at 1030 nm wavelength). As a result, the HHG photons are generated in pulses with typical durations on the order of a few hundred attoseconds.

In a multi-cycle laser pulse of around 10 fs pulse duration or more (in the near infrared), several field strength maxima of comparable height occur every half optical period, which leads to the emission of several subsequent XUV light bursts in a so-called attosecond pulse train. The temporal structure of the APT translates into a spectrum with a set of well-separated high harmonics at odd multiples of the fundamental laser photon energy. At 1030 nm wavelength the spacing between two neighboring harmonics is thus about 2.4 eV and their width on the order of 300 meV for typical laser pulse lengths of tens of femtoseconds.

In very short few-cycle laser pulses the strongest field strength maximum can be significantly higher than the precedent and subsequent ones. Consequently, the highest XUV photon energies are only generated within a single attosecond burst, which leads to a continuous spectrum on the high-energy side of the spectrum. However, a certain amount of emission from more than only one field maximum cannot be avoided completely. To minimize these weaker side-pulses, the CEP has to be chosen such, that the maximum of the envelope coincides with a maximum of the electrical field strength in a so-called cosine-pulse (Fig. 2.1a).

Hence, in the case of sufficiently short few-cycle driving laser pulses the highest photon energies are only generated once per pulse. By spectral filtering only this high-energy part of the spectrum, an isolated attosecond pulse can then be realized in an amplitude-gating scheme [4]. Other approaches for the generation of IAPs can also allow for longer fundamental laser pulses and include ionization gating [46], polarization gating [47, 48] and the attosecond lighthouse [49].

### 2.2.4 Phase-matched HHG

In coherent frequency conversion processes it is crucial that the newly generated wavelengths acquire the same phase upon propagation through the conversion medium as the fundamental. This phase matching ensures a coherent build-up of the generated photons and is thus essential for reasonable HHG conversion efficiencies.

The three main phase contributions of the acquired phase in the HHG process are dispersion in the HHG gas target  $\Delta k_{\text{gas}}$ , the Gouy-phase  $\Delta k_{\text{Gouy}}$  and the intensity-dependent atomic dipole phase  $\Delta k_{\text{dipole}}$  [50]:

$$\Delta k_{\text{hhg}} = \Delta k_{\text{dipole}} + \Delta k_{\text{Gouy}} + \Delta k_{\text{gas}} \quad (2.10)$$

The phase mismatch induced by the intensity dependence of the dipole phase is well approximated by the following expression [51]:

$$\Delta k_{\text{dipole}} = -\alpha \frac{\partial I_{\text{IR}}}{\partial z} \quad (2.11)$$

Here, the intensity of the fundamental laser beam is  $I$  and  $z$  its propagation axis centered at the focus position. The reciprocal intensity coefficient  $\alpha$  is on the order of  $10^{-14} \text{ cm}^2/\text{W}$  for the short and  $10^{-13} \text{ cm}^2/\text{W}$  for the long trajectory [52, 53].

The Gouy-phase induced term due to the focusing geometry is

$$\Delta k_{\text{Gouy}} = -q \frac{\partial \Phi_{\text{Gouy}}}{\partial z} = -q \frac{z_{\text{R}}}{z^2 + z_{\text{R}}^2} \quad (2.12)$$

where  $q$  denotes the harmonic order and  $z_{\text{R}}$  the Rayleigh length.

The third term is the phase mismatch between the fundamental wavelength  $\lambda$  and its  $q^{\text{th}}$  harmonic due to dispersion in a partially ionized gas [54, 55]

$$\Delta k_{\text{gas}} = qk(\lambda) - k(\lambda/q) \underset{q \gg 1/q}{\approx} \frac{2\pi Nq \Delta\delta}{\lambda} \cdot \left(1 - \frac{\eta}{\eta_{\text{cr}}}\right) \quad (2.13)$$

$$\eta_{\text{cr}} = \left(1 + \frac{r_e \lambda^2}{2\pi \Delta\delta}\right)^{-1} \quad (2.14)$$

Here,  $N$  is the total atom number density,  $\Delta\delta = \delta(\lambda) - \delta(\lambda/q)$  the difference in dispersion per number density between  $\lambda$  and  $\lambda/q$ ,  $\eta$  the ionization fraction and  $r_e$  the classical electron radius. The so-called critical ionization fraction  $\eta_{\text{cr}}$  is the fraction of ionized atoms above which the phase mismatch becomes negative. In the near infrared it is on the order of up to a few percent depending on gas and wavelength [56].

For efficient HHG it is hence necessary, that these three components add up to zero phase mismatch:

$$\Delta k_{\text{hhg}} = \Delta k_{\text{dipole}} + \Delta k_{\text{Gouy}} + \Delta k_{\text{gas}} \stackrel{!}{=} 0 \quad (2.15)$$

In the focus at  $z \approx 0$  we can neglect  $\Delta k_{\text{dipole}}$  and by inserting the expressions from Eqs. 2.12 and 2.13 come to the following expression for the number density for phase-matched HHG:

$$N_{\text{pm}} = \frac{\lambda^2}{2\pi^2 \Delta\delta w_0^2 \cdot (1 - \eta/\eta_{\text{cr}})} \quad (2.16)$$

Here,  $w_0$  is the focus beam waist derived from the Rayleigh length  $z_{\text{R}}$ . The formula shows, that smaller beam waists require significantly higher HHG phase-matching gas density. However, in practice the gas density limited because of the necessary pumping capacity of the vacuum pumps and because of the high XUV reabsorption in the gas target and in the background pressure of the HHG vacuum chamber (Section 3.3.3). Moreover, higher peak intensities also lead to higher ionization fractions and phase-matched high harmonic generation is impossible for  $\eta > \eta_{\text{cr}}$ . Again, this implies that very tight focusing is unfavorable for efficient HHG.

### 2.2.5 HHG at MHz repetition rate

For high harmonic generation at high pulse repetition rates, it is very challenging to simultaneously comply with the requirements for high photon energies in Eq. 2.9 and high conversion efficiencies in Eq. 2.16. At a fixed average laser power, the peak laser power is inversely proportional to the repetition rate, which means that harder focusing would be necessary to reach high peak intensities. However, this collides with the phase-matching conditions. As it will be shown in the next section, this contradiction can be solved by employing enhancement cavities, which allow for both high peak power and high pulse repetition rates at the same time.

## 2.3 Enhancement cavities for HHG

Optical resonators are at the very foundation of laser technology and consist in the simplest case of two mirrors, which "store" the light in between them. In an active laser resonator, the circulating light is constantly amplified by stimulated emission in a gain medium within the cavity which is pumped by an external energy source such as light emitting diodes.

A passive resonator or enhancement cavity does not have an active gain medium but light is constantly coupled in from an external coherent source via interference. By this means, the power of a driving laser can be enhanced by orders of magnitude within the cavity, enabling circulating power levels up to the megawatt range [57].

With enhancement cavities supporting femtosecond pulse durations [58, 59] the resulting high peak powers are thus perfectly suited for high harmonic generation [25, 60, 61]. Because the conversion efficiency of HHG is typically on the order of  $10^{-7}$  to  $10^{-5}$  [44, 62–64] it is in principle possible to recycle almost the entire driving fundamental laser pulse in an HHG cavity.

For the purpose of cavity-enhanced HHG a traveling-wave type cavity is best suited, where the light propagates in one direction through the resonator. It typically consists of at least four mirrors through one of which, the light is coupled into the cavity.

### 2.3.1 Power enhancement

In a simple picture, the enhancement of a passive resonator can be described by three parameters: The field reflectivity of the input coupling mirror  $r(\omega)$ , the round-trip phase  $\delta(\omega)$  and round-trip field transmission  $a(\omega)$ , which accounts for losses within the resonator. This subsection follows closely Ref. [65], where at a fixed angular optical frequency  $\omega$  and an incoming seed power of  $P_0$  the intra-cavity power  $P_{\text{cav}}$  is derived as:

$$P_{\text{cav}} = P_0 \frac{1 - r^2}{(1 - ra)^2 + 4ra \sin^2 \delta/2} \quad (2.17)$$

The power enhancement as function of  $\delta$  is displayed in Fig. 2.4 and exhibits a  $2\pi$  periodicity. The round-trip phase change of the pulse depends on the length of the cavity  $d$  and its refractive

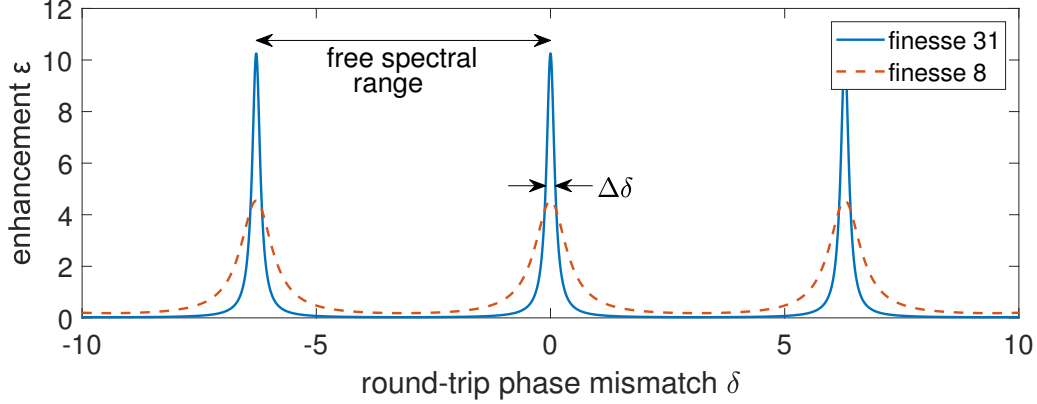


Figure 2.4: Power enhancement resonances of a cavity for two different finesse values. The finesse is the ratio of the distance between the resonances (free spectral width) and the resonance width  $\Delta\delta$ .

index  $n(\omega)$ , the laser wavelength  $\lambda$  and the spectral phase of the cavity roundtrip  $\Phi_{\text{cav}}(\omega)$  which is introduced by the mirrors or the HHG gas target. It can be written as

$$\delta(\omega) = \frac{2\pi d n(\omega)}{\lambda(\omega)} + \Phi_{\text{cav}}(\omega) = \frac{d \omega n(\omega)}{c} + \Phi_{\text{cav}}(\omega) \quad (2.18)$$

Hence, a  $2\pi$ -shift in  $\delta$  corresponds to a cavity length change of  $\lambda$  or a change in frequency of  $2\pi c/d$  (at a refractive index of one).

If the round-trip phase change  $\delta$  is a multiple of  $2\pi$ , it results in a maximum power enhancement of:

$$\mathcal{E}_0 = \left. \frac{P_{\text{cav}}}{P_0} \right|_{\delta=2n\pi} = \frac{1 - r^2}{(1 - ra)^2} \quad (2.19)$$

The full width at half-maximum of the resonances as function of the phase mismatch  $\delta$  can be calculated from Eq. 2.17 as follows:

$$\Delta\delta \approx 2 \frac{1 - ra}{\sqrt{ra}} \quad (2.20)$$

The approximation in the derivation of this formula is valid for  $\Delta\delta \ll 1$  which is ensured for all cavities with reasonably high input coupler reflectivity and low round-trip losses.

The cavity finesse  $\mathcal{F}$  is defined as the ratio of the resonance width  $\Delta\delta$  and the so-called free spectral range, which is the distance between the resonances (Fig 2.4). In the phase representation, the free spectral range is simply  $2\pi$  but it is also common to express it in laser frequency or cavity length (see Eq. 2.18). The finesse can be written as:

$$\mathcal{F} = \frac{2\pi}{\Delta\delta} \approx \frac{\pi\sqrt{ra}}{1 - ra} \quad (2.21)$$

The higher the reflectivity of the input coupler and the lower the round-trip losses, the higher is the finesse.

Fig 2.4 displays the power enhancement for cavities with different finesesses. A high finesse usually translates into high power enhancement and is equivalent to a very sharp resonance peak. However, a high cavity finesse is detrimental for the large spectral bandwidth of ultrashort laser pulses. Because the photon lifetime in the cavity is proportional to the finesse [65] small nonlinear cavity phases accumulate over many roundtrips and impair the broadband enhancement in high-finesse cavities. Moreover, a high finesse is inconvenient from a practical point of view, because the cavity length needs to be stabilized with very high precision and reliability to remain within the sharp resonance for a stable lock and high enhancement. For intra-cavity HHG, low finesse cavities have proven to be more efficient, as it will be elaborated in the next section.

### 2.3.2 Intensity clamping in HHG cavities

The process of high harmonic generation inherently requires the partial ionization of a gas target within the resonator, which inevitably introduces nonlinear phase terms. In single-pass HHG setups, such nonlinear phases do not pose a problem as long as the phase-matching requirements are met (Section 2.2.4).

In intra-cavity HHG however, plasma induced changes of the spatial, spectral and temporal profile of the circulating laser pulse reduce the overlap with the seed pulse and thus impair power enhancement. Consequently, the intracavity power in a cavity with HHG gas target can be significantly lower than in an empty cavity, which has to be considered in the design process of a cavity-based HHG source.

Absorption, dispersion, self-phase modulation and Kerr-lens effects also occur in the un-ionized gas, but the nonlinearities in the plasma fraction of the gas target induce the dominating phase terms at typical HHG conditions. Because the plasma density rises during the transition of the pulse, the refractive index changes on the timescale of the pulses and the resulting nonlinear phase shift leads to spectral broadening. Additionally, the spatial intensity gradient generates a plasma lens.

Because the fraction of ionized atoms increases with the intra-cavity intensity, the nonlinear phase can impair enhancement up to a point, where higher seed power will hardly have any effect on the intracavity power. This saturating behavior has been observed in several experiments [66–69] and is commonly referred to as intensity clamping.

Because of the saturation of the intracavity intensity, increasing the seed power beyond a certain level does not result in an increased high harmonic output. Since the curve flattens significantly from the point, where the intra-cavity peak intensity reaches around 65% of its value without HHG gas target, the intensity at this point is defined as the clamping intensity (Fig. 2.5a).

Experimental and theoretical studies over a wide parameter range have identified the key parameters for the clamping intensity and found the following empirical law [69]:

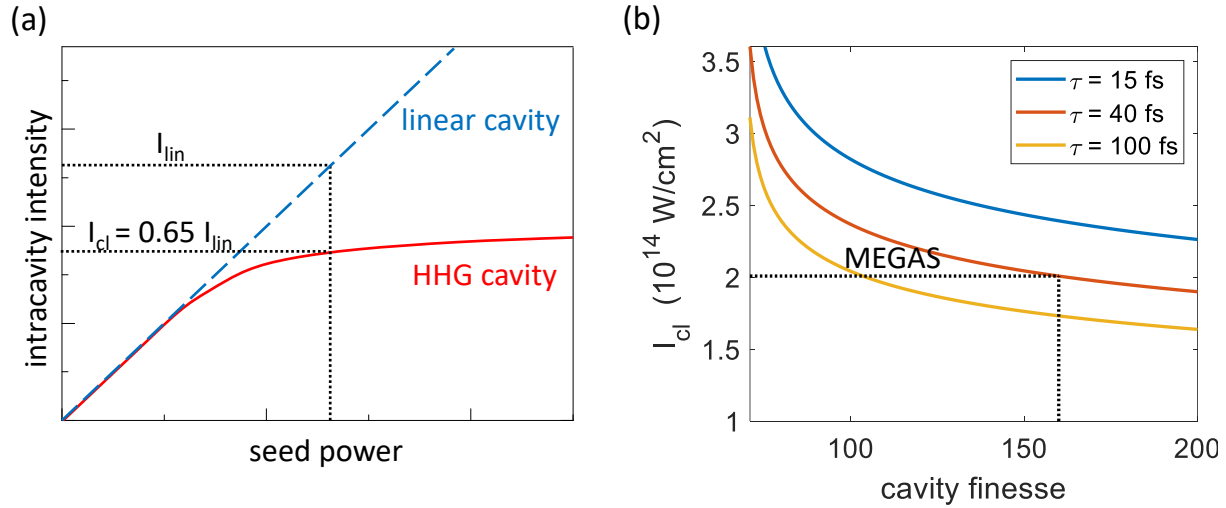


Figure 2.5: Intensity clamping effect in a nonlinear enhancement cavity. **a)** The peak intensity in a HHG enhancement cavity saturates due to distortions of the circulating pulse in the HHG gas and the generated plasma. Holzberger et al. developed a formula for the point where the clamping intensity  $I_{cl}$  is 65% of the intensity in the cavity without gas [69]. **b)** Clamping intensities according to Eq. 2.22 for HHG in argon at a gas density-length of  $4 \cdot 10^{16} \text{ cm}^{-2}$ . The MEGAS cavity finesse of 160 was chosen to enable intracavity peak intensities of  $2 \cdot 10^{14} \text{ W/cm}^2$  at these parameters [70].

$$I_{cl}(\tau, \mathcal{F}, nl) = I_0 \cdot \left( \frac{\tau_0 - \alpha}{\tau - \alpha} \frac{\mathcal{F}_0 - \beta}{\mathcal{F} - \beta} \frac{n_0 l_0 - \gamma}{nl - \gamma} \right)^\delta \quad (2.22)$$

The clamping intensity  $I_{cl}$  thus depends on the pulse duration  $\tau$ , the cavity finesse  $\mathcal{F}$ , the gas target density-length product  $nl$  and a set of variables  $(\alpha, \beta, \gamma, \delta, I_0, \tau_0, \mathcal{F}_0, n_0 l_0)$ , which are tabulated for xenon, neon and argon in Ref. [69].

The most important consequence of this clamping law is that increasing the finesse of a HHG cavity to achieve higher intra-cavity intensities can be counterproductive (Fig. 2.5b). The reason for this behavior is, that the finesse is proportional to the photon lifetime within the cavity [65]. Consequently, pulses in a high-finesse cavity accumulate the nonlinear phase of the gas target over a higher number of round trips. Hence, it makes more sense to increase the seed power and operate a cavity at the lowest possible finesse to achieve the necessary intra-cavity intensity for the desired application [66, 69, 71].

### 2.3.3 Design of a HHG enhancement cavity

Taking the findings of the previous sections into consideration, the key parameters of the design of an enhancement cavity for high harmonic generation can be broken down to three main relations:

For high harmonics with certain photon energies, a specific intra-cavity peak intensity must be reached according to Eq. 2.9.

The phasematching conditions pose requirements on the focus size, the maximum ionization fraction and gas density (Eq. 2.16).

From the resulting necessary peak intensity and focus and gas target geometry, the maximum usable finesse is then derived from the clamping law in Eq. 2.22.

Because the power enhancement scales more favorably with a lower input coupler reflectivity than with other round-trip losses (see Eq. 2.19), the desired finesse is best realized by choosing a comparably low input coupler reflectivity.

The remaining technical limitations in cavity-based HHG are consequently the minimum achievable pulse duration, which is mainly limited by the available cavity optics, and the maximum seed power, which is provided by the laser system.

## 2.4 Attosecond photoelectron spectroscopy

In 2001 ultrafast physics was revolutionized by the first two attosecond photoelectron spectroscopy experiments: One of them relying on reconstruction of attosecond beating by interference of two-photon transitions (RABBITT) [3] utilizing APTs and the other one on the attosecond streak camera [4] with IAPs. Ever since then, these two techniques have been used in parallel to characterize attosecond pulses and to investigate electron dynamics in gases [10, 13, 72, 73], molecules [74–77] and solids [8, 11, 14, 15, 78]. The following sections will be dedicated to introducing the fundamental physics of photoemission and of XUV-pump IR-probe photoelectron spectroscopy, explaining the working principle of attosecond streaking and RABBITT in detail and comparing their individual advantages and drawbacks.

### 2.4.1 The photoemission process

The description of the photoemission process in this section closely follows Ref. [79].

Photoemission from a solid sample requires a minimum photon energy to overcome the material work function. This corresponds to the energy difference between the Fermi level, which marks the highest occupied state at absolute zero temperature, and the vacuum level. It is typically on the order of a few electronvolts [80] such that photons with wavelengths in the ultraviolet spectral region or shorter are required for photoemission. The kinetic energy  $E_{\text{kin}}$  of the released photoelectron can be calculated as:

$$E_{\text{kin}} = \hbar\omega - \Phi - |E_{\text{bind}}| \quad (2.23)$$

Here,  $\hbar\omega$  denotes the photon energy,  $\Phi$  the work function and  $E_{\text{bind}}$  eventual additional binding energy dependent on the initial state of the electron (step 1 in Fig. 2.6). The momentum

of the emitted photoelectron parallel to the emission surface  $\mathbf{p}_{||}$  is directly related to the crystal momentum  $\mathbf{k}_{||}$  within the solid:

$$\mathbf{p}_{||} = \hbar \mathbf{k}_{||} = \sqrt{2m_e E_{\text{kin}}} \sin \vartheta \quad (2.24)$$

Here,  $\vartheta$  denotes the angle between surface normal and emission direction and  $m_e$  the electron mass. The momentum of the absorbed photon can be neglected at typical experimental conditions. Because there is no translational symmetry along the surface normal, the perpendicular component of the crystal momentum  $\mathbf{k}_{\perp}$  is not conserved in the emission process.

According to Eq. 2.24 the emission angle  $\vartheta$  of the photoelectron can be directly related to its quasi momentum in the crystal parallel to the surface  $\mathbf{k}_{||}$ . This direct access to two dimensions of the crystal momentum makes angle-resolved photoemission spectroscopy (ARPES) the most powerful and direct tool to investigate the band structure of solids. For this purpose, either the sample can be tilted to capture electrons from different emission angles or an angle-resolving electron spectrometer can be used to simultaneously collect and image electrons from a large range of emission angles.

The probability  $w_{i,f}$  for the photoemission from an initial  $N$ -electron ground state  $\Psi_i^N$  to a final state  $\Psi_f^N$  can be calculated from the perturbative photon interaction hamiltonian  $H_{\text{int}}$  according to Fermi's golden rule as [79]:

$$w_{i,f} = \frac{2\pi}{\hbar} |\langle \Psi_i^N | H_{\text{int}} | \Psi_f^N \rangle|^2 \delta(\hbar\omega + E_i^N - E_f^N) \quad (2.25)$$

$$H_{\text{int}} = -\frac{e}{2m_e c} \cdot (\mathbf{A} \cdot \mathbf{p} + \mathbf{p} \cdot \mathbf{A}) \quad (2.26)$$

Here,  $\mathbf{A}$  denotes the electromagnetic vector potential,  $\mathbf{p}$  the electron momentum operator and  $E_i^N$  and  $E_f^N$  the initial- and final-state energies of the system.

In a one-step model of photoemission, this equation can coherently describe the entire photoemission process from a solid if bulk, surface and vacuum are included into the hamiltonian [82] and the initial and final wave function are known. Usually, the final state wavefunction is obtained in an inverse LEED formalism, which accounts for the limited electron emission depth by damping of the wave function within the solid [83, p. 375].

For solid state systems the description in the one-step model is often too complex. Hence, the photoemission process is commonly decomposed in a model of three independent steps as displayed in Fig. 2.6 [84, 85]. In the first step, an incoming photon is absorbed and an electron from an occupied state is excited. In the second step, the electron travels to the surface and is subject to scattering. The inelastic scattering in this phase of photoemission can be described by means of an inelastic mean free path which follows a very similar curve in all solids and is on the order of several Å for electron energies of 10 to 100 eV [86]. In the third step, the electron is transmitted through the surface into the vacuum if its energy is sufficient to overcome the material work function. The emitted photoelectron spectrum and photoemission probability results from the combination of these three steps.

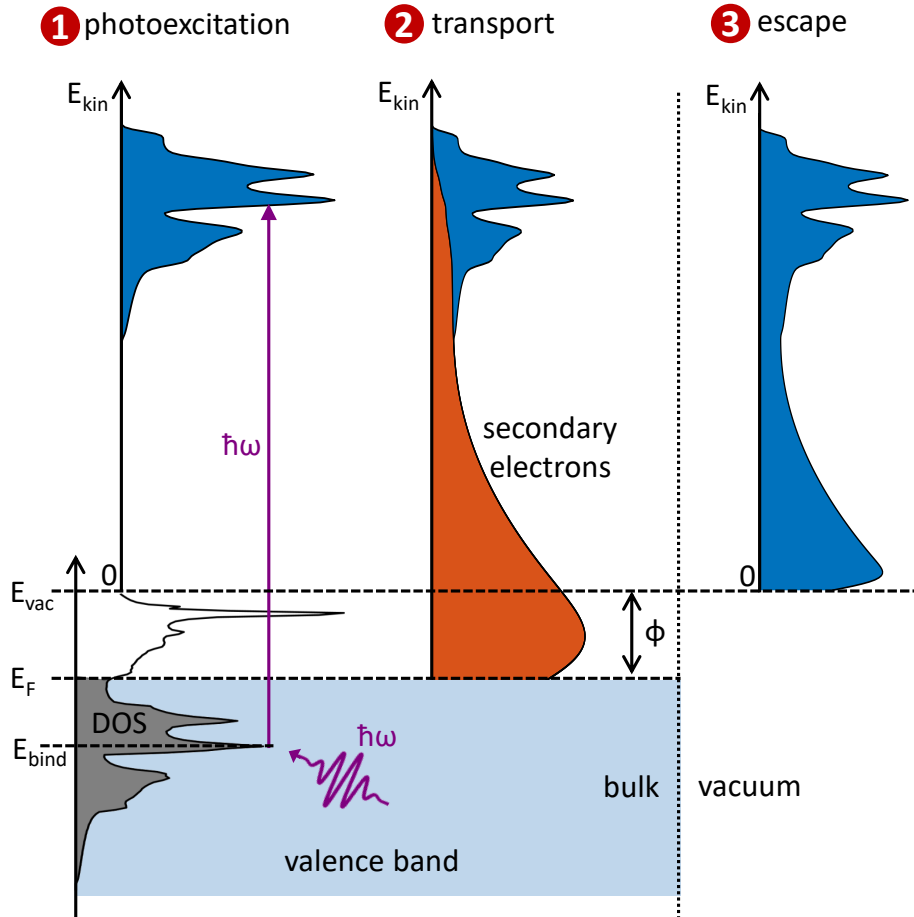


Figure 2.6: Three-step model of photoemission: In the first step, electrons from the occupied density of states (DOS) are excited by a photon with energy  $\hbar\omega$ . During their transport to the surface, some electrons are scattered inelastically and form a secondary electron background. In the final step, electrons with sufficient kinetic energy to overcome the work function  $\Phi$  escape from the sample. Inspired by Ref. [81].

### 2.4.2 Laser dressed photoionization

Attosecond photoelectron spectroscopy techniques rely on pump-probe measurements involving high-photon-energy pump pulses to photoionize a target material and a high-intensity laser pulse to probe the emitted photoelectrons. The pump pulses can either be generated by HHG (Section 2.2) or by free-electron lasers (FEL) [87] and are in the extreme ultraviolet or X-ray spectral region. The probe pulses are typically generated in titanium sapphire (Ti:Sa) solid-state or ytterbium-doped fiber laser systems and are in the infrared (IR) spectral range from 700 to 1100 nm wavelength. Hence, the photoionizing pump pulse will be referred to as XUV-pulse and the dressing probe pulse as IR-pulse for the rest of this work.

To derive an expression for photoionization in the presence of a laser field, we start from the

time dependent Schrödinger equation for a single active electron in the dipole approximation in atomic units:

$$H(t) |\psi(t)\rangle = \left( \frac{1}{2} (\mathbf{p} + \mathbf{A}_{\text{IR}}(t))^2 + V(r) + \mathbf{E}_X(t) \cdot \mathbf{r} \right) |\psi(t)\rangle = i \frac{d}{dt} |\psi(t)\rangle \quad (2.27)$$

Here,  $\mathbf{p}$  denotes the canonical momentum operator,  $V(r)$  the ionic core potential, the XUV field is given by its field  $\mathbf{E}_X(t)$  in the length gauge and the IR laser field is represented by its vector potential  $\mathbf{A}_{\text{IR}}(t)$  in the velocity gauge. The mixed-gauge representation here is chosen to facilitate the next calculation steps. After neglecting the influence of  $V(r)$  and  $\mathbf{E}_X(t)$  on the free electron compared to the IR electric field in the strong field approximation [88] and assuming that the IR field does not contribute to the ionization of the system, the resulting wave function is projected on plane wave final states and the following formula for an XUV-pump IR-probe spectrogram can be derived [89–91]:

$$S(\mathbf{p}, \tau) = |\langle \mathbf{p} | \psi(t) \rangle|^2 = \left| \int_{-\infty}^{\infty} dt \mathbf{d}_{\mathbf{p}+\mathbf{A}_{\text{IR}}(t)} \cdot \mathbf{E}_X(t - \tau) \cdot e^{i(\mathbf{p}^2/2+I_p) \cdot t} \cdot e^{i\Phi_{\text{IR}}(t)} \right|^2 \quad (2.28)$$

$$\Phi_{\text{IR}}(t) = \int_t^{\infty} dt' (\mathbf{p} \cdot \mathbf{A}_{\text{IR}}(t') + \frac{1}{2} \mathbf{A}_{\text{IR}}^2(t')) \quad (2.29)$$

Here  $\mathbf{d}_{\mathbf{p}} = \langle \mathbf{p} | \mathbf{r} | \psi_0 \rangle$  denotes the dipole transition matrix element,  $I_p$  the ionization potential and  $\Phi_{\text{IR}}(t)$  describes the electron phase induced by the electric field of the probe pulse.

The derived spectrogram formula resembles the one that describes frequency-resolved optical gating (FROG) as it is commonly used mainly in the visible and IR spectral range to characterize a laser pulse  $E(t)$  by gating it with a function  $G(t)$  [92]:

$$S_{\text{FROG}}(\omega, \tau) = \left| \int_{-\infty}^{\infty} dt E(t) \cdot G(t) \cdot e^{-i\omega t} \right|^2 \quad (2.30)$$

Comparing this formula and equation 2.28, it becomes obvious that the IR field represents a pure phase gate  $\Phi_{\text{IR}}(t)$  as long as the dipole transition matrix element does not change significantly over the relevant momentum range. As a type of blind-FROG [93], the XUV pulse can hence be retrieved by frequency-resolved optical gating for complete reconstruction of attosecond bursts (FROG-CRAB) [94].

However, there are two special cases of XUV pulse types, for which the interpretation of XUV-pump IR-probe photoelectron spectrograms is relatively intuitive without FROG-CRAB retrieval:

**Isolated attosecond pulses** probed by a laser field result in a spectrogram which is best understood in a wave picture as the dressed photoelectron peak follows the vector potential of the probe pulse as displayed in Fig. 2.7a. This technique is commonly referred to as **attosecond streaking**.

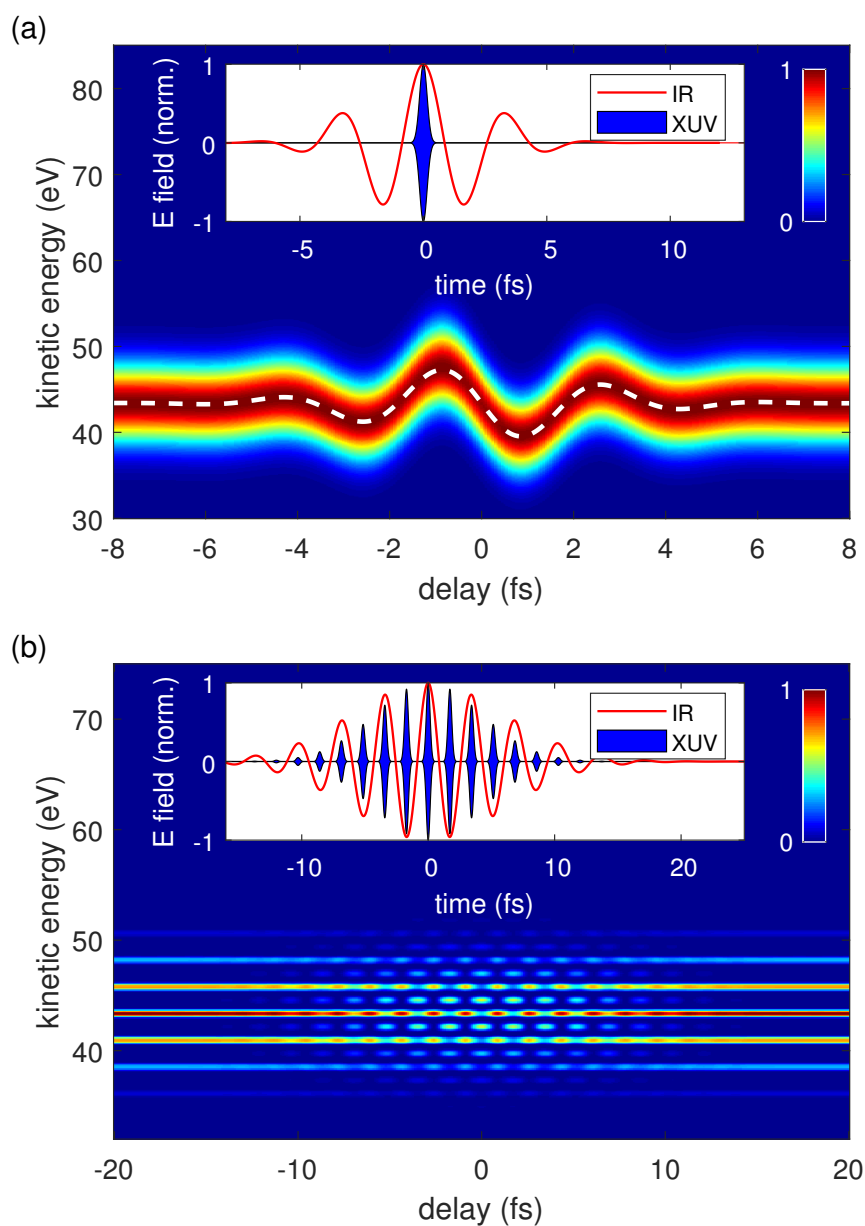


Figure 2.7: XUV-pump IR-probe photoelectron spectrograms calculated from Eq. 2.28 for an IR pulse centered at a wavelength of 1030 nm, an XUV spectrum centered around 65 eV, an ionization potential of 21.6 eV and a constant dipole transition element. **a)** Attosecond streaking as obtained from the IR pulse and the isolated attosecond pulse displayed in the inset. Due to the short XUV wavelength, only the envelope of its electrical field is depicted (equally in b). The IR vector potential is indicated by the white dashed line. **b)** RABBITT spectrogram obtained from the multi-cycle IR pulse and the attosecond pulse train displayed in the inset.

**Attosecond pulse trains** probed by a multi-cycle laser field give rise to delay-dependent sidebands between the high-harmonic peaks, which are best understood in the photon picture as two-photon transitions. These so-called **RABBITT** traces (Fig. 2.7b) also allow to characterize the temporal structure of the XUV and measure photoemission timing.

In the following sections both these techniques will be presented and compared.

### 2.4.3 The attosecond streak camera

The general idea of the streak camera is to map processes which are too fast to be observed directly to another observable. For attosecond streaking this means mapping the timing of photoelectrons liberated by an isolated attosecond pulse to the final electron velocity as illustrated in Fig. 2.8a. Although it is also possible to map the timing to the direction of the electron velocity with a circular polarized IR pulse in the so-called attosecond angular streaking [95], it is more common to map it to the absolute value of the electron velocity as it will be described in this chapter. This is realized by probing the photoelectrons with a linearly polarized ultrashort laser pulse with typical intensities of  $10^{13}$  to  $10^{14}$  W/cm<sup>2</sup>.

This streaking process is fully described by Eq. 2.28 but can also be understood in a more intuitive classical description: From the moment of emission, the photoelectron is fully exposed to the electric field of the laser pulse. Depending on the momentary orientation of the field the electron is initially either decelerated or accelerated. At typical experimental parameters the photoelectron velocity is far from being enough to leave the spatial extension of the laser field (typically several tens of  $\mu\text{m}$ ) within the laser pulse duration (several fs). Consequently, the released electron is not accelerated only once by the momentary electric field at the time of emission but experiences the entire laser pulse after its emission.

The final electron velocity component in the observation direction  $v_f$  of a photoelectron emitted at the time  $\tau_e$  and exposed to an external electric laser field  $E_{\text{IR}}(t)$  can then be calculated classically as follows [90]:

$$v_f = v_i + \cos(\theta) \cdot \frac{e}{m_e} \int_{\tau_e}^{\infty} dt E_{\text{IR}}(t) \quad (2.31)$$

Introducing the vector potential  $A_{\text{IR}}(t)$  of the laser pulse given by the integral over  $E_{\text{IR}}(t)$  in a charge-free environment (Fig. 2.8b) and choosing a suitable gauge we can derive from Eq. 2.31 the change in velocity of an electron emitted at the time  $t$  in an even more simple form:

$$\Delta v(t) = -\frac{e}{m_e} \cos(\theta) \cdot A_{\text{IR}}(t) \quad (2.32)$$

Hence, the amplitude of the laser induced velocity shift is strongest for observation in the direction of the electric field and follows directly the course of the probe vector potential (Fig. 2.7a).

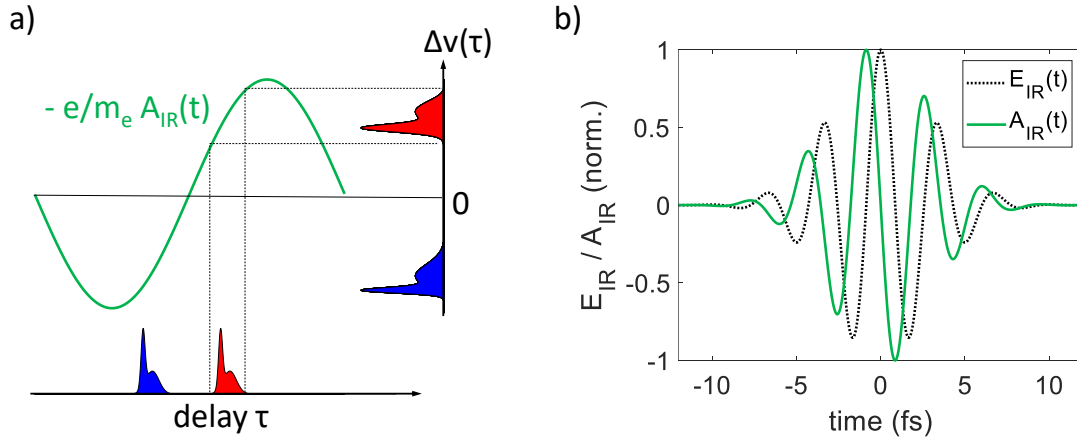


Figure 2.8: **a)** Working principle of the attosecond streak camera: The photoemission timing is mapped to a change in electron velocity depending on the delay  $\tau$  between emission and IR vector potential  $A_{\text{IR}}(t)$ . **b)** Electric field  $E_{\text{IR}}(t)$  and its vector potential  $A_{\text{IR}}(t)$  for an ultrashort laser pulse.

#### 2.4.4 The RABBITT-technique

First demonstrated in 2001 [3] and named afterwards by Muller et al. [96] the RABBITT technique had already been proposed theoretically five years before that [97]. Although the experimental setup is identical to attosecond streaking, a RABBITT spectrogram looks very different due to the photoionization by a train of attosecond pulses (Fig. 2.7a and b). Because the photoelectron wave packets originating from the different attosecond pulses interfere with each other, a RABBITT trace is not as intuitively understood as a streaking trace.

To understand RABBITT qualitatively it is easier to think in a photon-based picture as illustrated in Fig. 2.9a: Sidebands in between the high-harmonic photoelectron peaks arise from two-photon transitions involving the absorption of an XUV-photon and absorption or stimulated emission of an IR photon in a so-called laser assisted photoemission process [98]. Because each of these sidebands can be reached from its two neighboring harmonics, these two quantum pathways interfere coherently. This leads to an oscillatory behavior of the sidebands as a function of the pump-probe delay at twice the fundamental laser frequency as displayed in Fig. 2.9b.

From Eq. 2.28 we can mathematically derive the characteristic sideband oscillations in RABBITT spectrograms by inserting the electrical fields of IR and XUV in the following forms:

$$E_{\text{IR}}(t) = E_0(t) \cdot \sin(\omega_{\text{IR}} t) \quad (2.33)$$

$$E_{\text{X}}(t) = \sum_m A_{2m+1} \cdot \cos((2m+1)\omega_{\text{IR}} \cdot t + \Phi_{2m+1}) \quad (2.34)$$

Here, the XUV is represented by a sum of odd high harmonics with amplitudes  $A_{2m+1}$  and phases  $\Phi_{2m+1}$  and the IR field features an envelope  $E_0(t)$ , which complies with the slowly

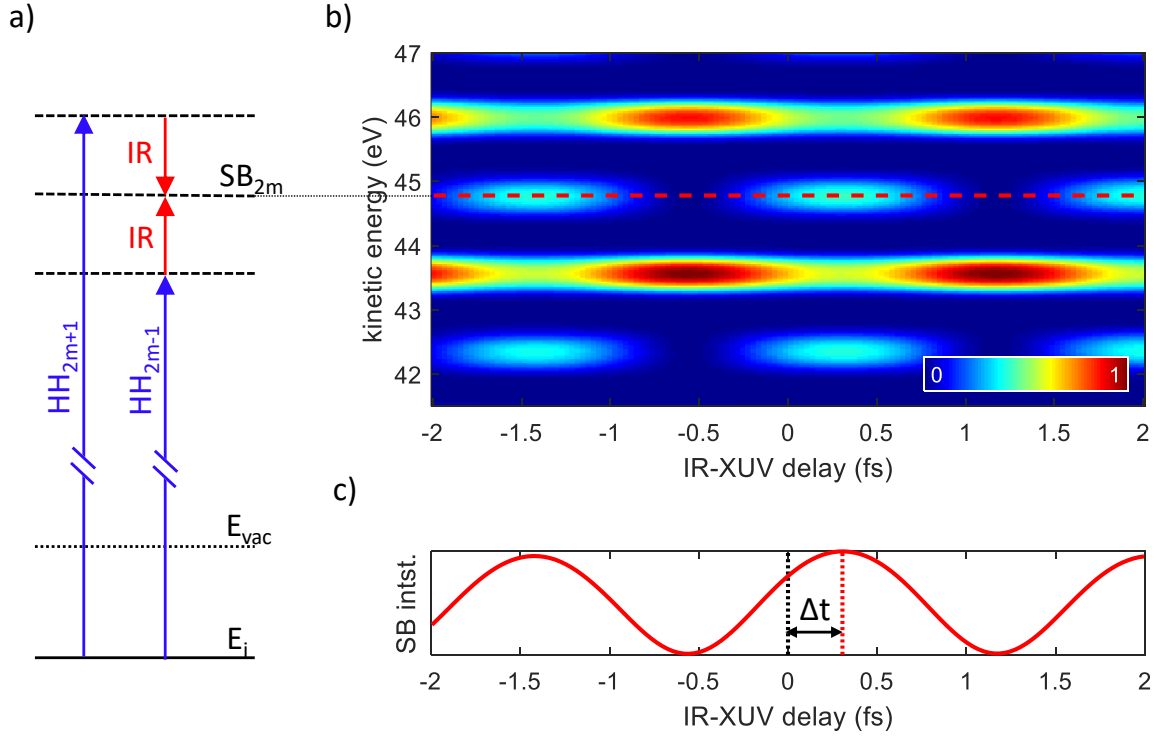


Figure 2.9: **a)** The sideband  $SB_{2m}$  is generated from its neighboring harmonics  $HH_{2m\pm 1}$  and the absorption or stimulated emission of an IR photon. **b)** In a RABBITT spectrogram the sideband intensity (position marked by the red dashed line) depends on the delay between XUV and IR-pulse. Spectrogram simulation based on Eq. 2.28. **c)** Sideband linecut taken at the energy marked in b). The photoemission delay  $\Delta t$  is encoded in the phase of the sine curve.

varying envelope approximation  $dE_0/dt \ll E_0 \omega_{IR}$ . The expression of the XUV field also implies a sufficiently long train of attosecond pulses to justify the representation of each harmonic as a single discrete frequency.

By inserting these fields in Eqs. 2.28 and 2.29 contributions at final kinetic energies corresponding to even multiples of  $\omega_{IR}$  appear and form modulated sidebands<sup>1</sup> [3]:

$$SB_{2m}(\tau) \propto \cos(2\omega_{IR} \cdot (\tau - \tau_{XUV,2m} - \tau_{PE,2m})) + \text{const.} \quad (2.35)$$

The sidebands oscillate as function of the pump-probe delay  $\tau$  at twice the laser frequency  $\omega_{IR}$  and their phase contains the XUV spectral phase difference of the two neighboring harmonics  $\tau_{XUV,2m} = (\Phi_{2m+1} - \Phi_{2m-1})/2\omega_{IR}$  and the photoemission delay  $\tau_{PE,2m}$ . The latter can be broken down into three different contributions [12]:

$$\tau_{PE} = \tau_W + \tau_{CC} + \tau_{transp} \quad (2.36)$$

<sup>1</sup>For a detailed description of the mathematical derivation steps refer to Ref. [99].

Here,  $\tau_W$  denotes a Wigner-type delay induced by the single-photon ionization process [100] and  $\tau_{CC}$  results from the continuum-continuum transition in the probe field [101]. For solid samples the transport time of the electrons from their mean emission depth to the surface  $\tau_{\text{transp}}$  also must be considered. All three contributions depend on the final electron kinetic energy and are thus different for each sideband order.

The pump-probe delay  $\tau$  is equal for all sideband orders and different final or initial states and materials. Among the other contributions the electron transport time is in solids usually the dominating term [14, 102] and the sum of  $\tau_W$  and  $\tau_{CC}$  typically no more than a few tens of attoseconds [10, 101, 103]. The sum of the delay terms which depend on the sideband order  $\Delta t_{2m} = \tau_{XUV,2m} + \tau_{PE,2m}$  is the total sideband delay as it can be extracted from a RABBITT spectrogram (Fig. 2.9c).

The approximations made in the derivation of this equation require the ponderomotive potential  $U_p$  of the laser field to be significantly smaller than  $\hbar\omega_{IR}$  which limits the maximum applicable laser intensity. At typical experimental conditions like  $10^{11}$  W/cm<sup>2</sup> and 1030 nm wavelength (i.e.  $\hbar\omega_{IR} = 1.2$  eV) the resulting ponderomotive potential of 10 meV fully satisfies this condition. For intensities (or photon energies) beyond this prerequisite, additional terms lead to higher order sideband oscillations [104, 105] which has also been observed in the scope of this thesis (Section 4.4).

### 2.4.5 Attosecond streaking and RABBITT compared

Both attosecond streaking and RABBITT are valuable tools for the observation of electron dynamics at the attosecond timescale and have enriched our understanding of it. Because both approaches have been shown to be in good quantitative agreement in gases [106] and solids [107] the choice between them can be made according to their suitability for the desired application as they feature a number of important differences:

**Experimental challenges** are posed by the need of ultrashort few-cycle laser pulses driving the HHG or gating mechanisms as it is necessary for the generation of isolated attosecond pulses. This can be considered a practical drawback of attosecond streaking. Additionally, a carrier-envelope phase stable probe laser is needed for attosecond streaking. Alternatively, the CEP of each individual pulse can be measured in phase-tagged attosecond streaking [108].

**Probe pulse intensities** of around  $10^{12}$  to  $10^{13}$  W/cm<sup>2</sup> are typically used to obtain well-modulated attosecond streaking traces, whereas RABBITT probe intensities are usually on the order of  $10^{11}$  W/cm<sup>2</sup> to prevent multi-IR-photon transitions [106, 109]. High probe intensities can cause irreversible damage to a sensitive sample or lead to perturbations of the system under study. Thermal or intensity induced effects can for example alter the initial population of states, affect the band structure as in the dynamical Franz-Keldysh effect [110, 111] or even turn an insulator into a conductor [112]. Depending on the goal of the study such effects can be wanted or perturbing the sample.

Moreover, high IR intensities cause a strong background of above-threshold-ionization (ATI) electrons at lower kinetic energies in attosecond streaking. Because this is hardly at all observed in RABBITT measurements, they are well suited to investigate photoelectrons with low kinetic energies, which can for example be useful to observe the influence of unpopulated electronic states close to the vacuum level [12, 78, 102]. Furthermore, the ATI electrons contribute to space-charge effects [113], which is a serious drawback in measurements where high energy resolution is needed.

**Complete characterization of attosecond pulses** is not provided by the traditional RABBITT approach, because it attributes only a discrete spectral phase to each harmonic which in reality do have a finite width with a certain dispersion. Consequently, RABBITT only measures the average pulse shape in an APT, but no pulse-to-pulse variation in shape, intensity or phase. Although this is sufficient for the vast majority of applications, it is also possible to retrieve a RABBITT-trace using the FROG-CRAB algorithm to fully characterize an APT [114]. Another approach to gain more information about an APT is the so-called Rainbow RABBITT which also considers the intra-sideband delays [115, 116].

**Attosecond chirp** can pose a serious problem in the correct FROG-CRAB retrieval of exact delays in attosecond streaking traces, particularly when the central momentum approximation is used [106, 117]. Although being described by the same physics and formulae as streaking, RABBITT spectrograms do not need to be retrieved with an algorithm but can be evaluated by sine fits or Fourier analysis, which is simpler and unaffected by attochirp.

**High XUV photon energies** (of more than  $\sim 50$  eV) at decent flux are usually inaccessible to RABBITT experiments because the longer fundamental laser pulses lead to lower peak power at good phase-matching conditions. Low repetition rate laser systems can compensate for this, but suffer from space-charge effects on solid samples. Therefore, RABBITT with high photon energies has so far only been used to study gas atoms [13, 115].

Consequently, until now the dynamics of deeply bound electronic states in solids have only been studied by means of attosecond streaking. This significant drawback for RABBITT has been overcome within the framework of the MEGAS project and this thesis by high-repetition-rate intra-cavity high harmonic generation (Section ??).

**High energy resolution** in RABBITT measurements is enabled by the well-separated high harmonics of typically only several hundreds of meV width in an APT. Consequently, RABBITT intrinsically measures simultaneously photoemission delays at several discrete final electron kinetic energies for the same initial state, which is not the case for attosecond streaking and its broad continuous excitation spectrum.

Although it is possible to obtain even continuously energy-resolved delays from a streaking trace via the FROG-CRAB retrieval algorithm [16], this is less intuitive and less direct than in the RABBITT approach and therefore potentially more susceptible to retrieval-induced errors. Especially when dealing with closely spaced electronic states

and complex band structures in solids, the high energy resolution offered by RABBITT is highly beneficial, particularly when combined with angular resolution [78, 102].

The drawback of measuring only at discrete energies with RABBITT can be countered by a closer high-harmonic spacing at smaller laser wavelength [118] or by shifting the high harmonics to scan over different energies. Due to the possibility of accumulating blueshift, which is introduced by phase modulation in the HHG target, intra-cavity HHG is particularly well suited for the latter approach, as demonstrated in Section 5.3.4.

**Unambiguous attribution of photoelectrons** to a specific pulse in an APT is not possible, which permits the ingenious combination of high energy and time resolution in RABBITT measurements, which seemingly contradicts Heisenberg's time-energy uncertainty principle [119]. Consequently, only photoemission delays of less than the time between two consecutive attosecond pulses (i.e. half a fundamental laser cycle) can be measured unambiguously. In practice, this does typically not pose a problem because the relevant delays to be observed are far below this time of for example 1.7 fs at 1030 nm wavelength.

**The absolute timing of photoemission** is not directly determinable with neither of the two techniques because it is not possible to determine the exact XUV-IR delay of a spectrogram. For this reason, only relative photoemission times can be measured and it is most common to reference photoemission from different initial states of a sample [8, 10, 13]. However, by referencing photoemission from complicated solid samples to photoemission from gas atoms, which are theoretically well understood, it is possible to come very close to measuring the absolute photoemission timing [11, 12, 14].



# Chapter 3

## Experimental setup

The MEGAS project (megahertz attosecond pulses for ultrafast photoelectron microscopy and spectroscopy) was a collaboration of the Fraunhofer Institute for Optics and Precision engineering (IOF), the Fraunhofer Institute for Laser Technology (ILT) and the Max-Planck Institute for Quantum Optics (MPQ). By combining their expertise in their respective fields of research, these groups were able to conceive and implement an experimental setup, which combines high XUV flux and high photon energies with space charge-free photoemission conditions and attosecond angle-resolved photoelectron spectroscopy (ARPES) in a unique and unprecedented manner [24].

The laser system was mainly set up by the IOF, the spectral broadening unit and pierced mirror designed and provided by the ILT and the HHG enhancement cavity was designed and implemented by the MPQ. The application of this novel HHG source in attosecond and angle-resolved PES experiments was the object of this work. This comprises conception and implementation of the attosecond beamline together with improvements of the ARPES setup, which were necessary to deal with the challenges posed by the high repetition rate. The resulting experimental setup will be presented in this chapter.

### 3.1 Laser system

The laser system is based on a commercial titanium-sapphire oscillator<sup>1</sup> (Ti:Sa) pumped by a 532-nm CW laser<sup>2</sup> (Fig. 3.1a). The mode-locked IR laser pulses are centered around 780 nm with a typical spectral FWHM of 230 nm and 500 mW average power at 73.6 MHz pulse repetition rate (Fig. 3.1b). The oscillator beam is split 50:50 at a beam splitter in two branches: one half can be carrier-envelope phase stabilized by an acousto-optical frequency shifter (AOFS) and compressed down to 6 fs pulse duration. This beam branch has not been used in the context of this work but could for example serve as pump pulse in future plasmonic experiments like attosecond photoemission electron microscopy [120, 121].

---

<sup>1</sup>*Femtolasers* Rainbow CEP4

<sup>2</sup>*Coherent* Verdi V10

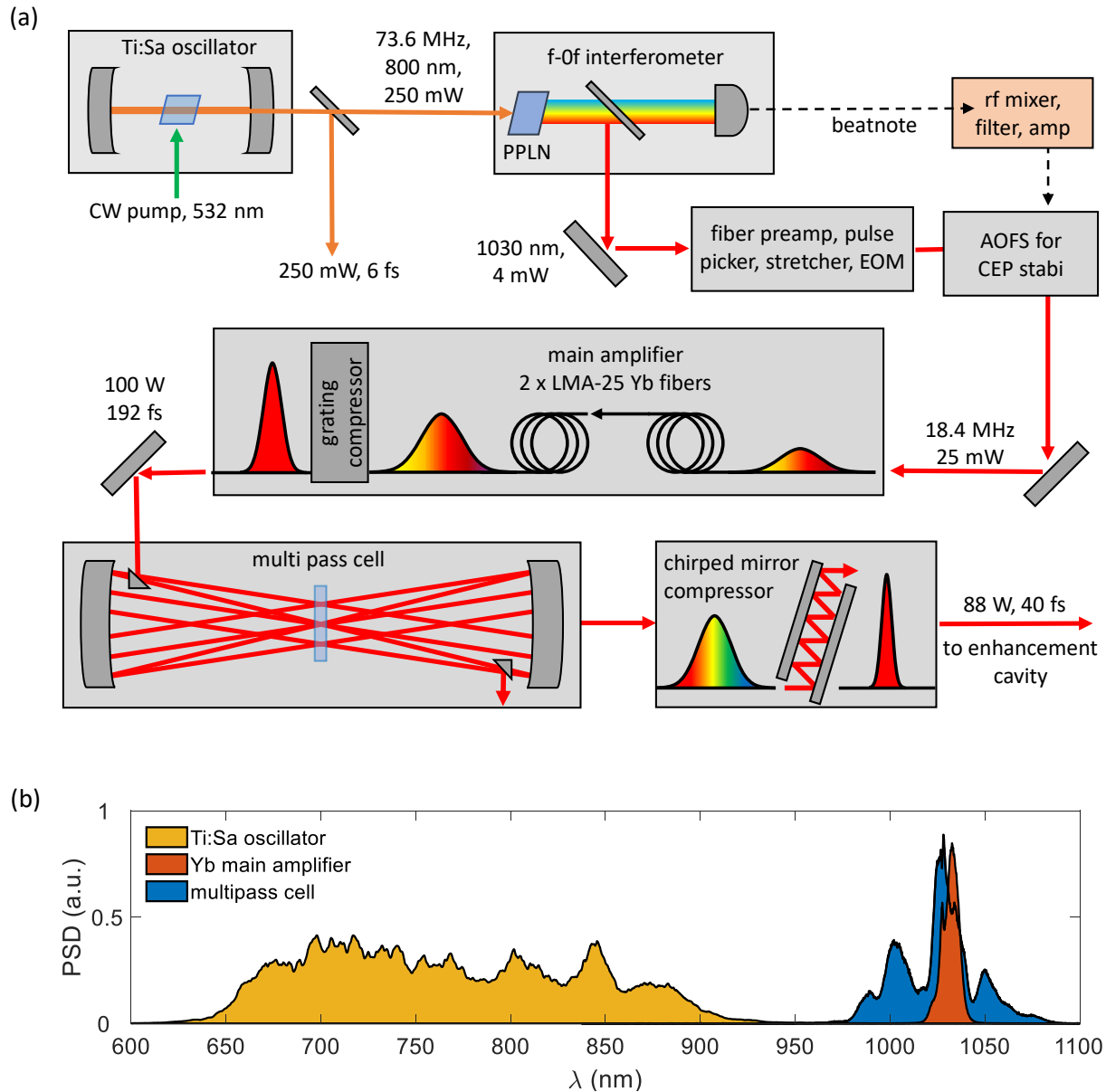


Figure 3.1: **a)** Laser system setup: A Ti:Sa oscillator generates the seed pulses for the MEGAS system. Half of the output power is spectrally broadened in a PPLN-crystal to generate a  $f_{\text{ceo}}$  beatnote signal and the light around 1030 nm seeds the amplifier system. The pulses are fed to an Yb-doped fiber pre-amplifier with a stretcher, a pulse picker and an EOM. The  $f_{\text{ceo}}$  is stabilized in an AOFS in a feed-forward scheme. The pulses are amplified in two LMA fibers and compressed by gratings. A multipass cell broadens the spectrum in 45 passes through a fused silica substrate and the pulses are compressed to 40 fs by chirped mirrors. **b)** Power spectra of the titanium-sapphire oscillator, the main amplifier and after the multipass cell.

The other half of the laser beam is focused in a periodically-poled lithium niobate crystal (PPLN) for difference frequency generation. The newly generated frequency components allow for the determination of the carrier-envelope offset frequency in a so-called f-to-0f interferometer [122]. In our setup, this beatnote signal is used for a feed-forward CEP stabilization in another module later on. The spectral components of 1030 nm wavelength are split off by a reflective filter and serve as seed for the following fiber amplifier system. The setup thus combines the high phase and pulse shape stability of the Ti:Sa oscillator with the high average beam power of state-of-the-art fiber amplifiers [123].

Subsequently, the laser pulse enters the multi-stage amplifier system based on ytterbium-doped fibers<sup>3</sup>. After the first amplification step in the preamplifier, an acousto-optical modulator serves as pulse-picker to reduce the pulse repetition rate to 18.4 MHz [124]. The preamplifier unit also stretches the laser pulse by means of fiber-Bragg gratings for subsequent chirped-pulse amplification [125]. Additionally, a fiber-coupled electro-optical modulator (EOM) in the preamplifier operated at 3 MHz generates radio-frequency (RF) sidebands, which are required for the Pound-Drever-Hall cavity lock (Section 3.2.1).

The pulse picker and the amplifier system support repetition rates from the full 73.6 MHz of the oscillator down to around 1 MHz. However, the subsequent spectral broadening unit and pulse compression must be modified or replaced at a pulse repetition rate other than 18.4 MHz. It is currently investigated, how the higher pulse energies at 1 or 2 MHz pulse repetition rate could allow for spectral broadening in a hollow-core fiber which would support a pulse duration of 10 fs and significantly higher peak power. Although this repetition rate is unpractical for enhancement cavities, it could for example be used for single-pass HHG or other experiments.

After the preamplifier, the laser is CEP stabilized in an AOFS<sup>4</sup> which utilizes the beatnote signal generated in the PPLN-branch of the oscillator in a feed-forward scheme. The chirped laser pulses enter a grating-based mini-compressor before the main amplifier for dispersion fine tuning. The main amplifier itself consists of two ytterbium-doped large-mode-area (LMA) fibers which yield an average laser power of up to 100 W at 192 fs FWHM pulse duration after a grating compressor.

A multipass cell is used to spectrally broaden the laser pulses in 45 passes through an anti-reflex coated 13-mm fused silica substrate [126]. The transmission through the multipass cell and the subsequent chirped mirror compressor is 88% at a final FWHM pulse duration of 40 fs.

## 3.2 Enhancement-cavity based high harmonic generation

Previous experimental and theoretical studies of the MEGAS collaborators at MPQ have identified the optimum parameters for efficient intracavity HHG [67, 69, 127, 128]. According to these findings the MEGAS was set up to generate a high photon flux and high photon energies [24, 70].

---

<sup>3</sup>developed by IOF and Active Fiber Systems GmbH within the scope of the MEGAS project

<sup>4</sup>Femtolasers CEP4 module

### 3.2.1 Enhancement cavity setup

The MEGAS cavity consists of 8 mirrors and is set up in a vacuum chamber which is 3 m long to accommodate the total cavity length of 16.3 m in accordance with the laser pulse repetition rate (Fig. 3.2). It is a standard bow-tie resonator and operated at the inner stability edge. It has been shown that this configuration is best suited for high-power enhancement cavities because it exhibits a large beam size on the cavity mirrors to avoid mirror damage or temperature gradients and is robust against misalignment [129]. Two focusing mirrors with a focal length of 300 mm each separated by slightly more than twice the focal length give rise to a tight focal point for HHG in between them.

The size and divergence of a mode at any point in a empty resonator is determined by the positioning and focal lengths of the cavity mirrors. Optimum input coupling efficiency into the cavity is achieved if the incoming beam overlaps perfectly with the cavity mode at the input coupling mirror in beam size, divergence, spectrum and phase.

To enhance a laser pulse in a cavity it is necessary to achieve stable and continuous constructive interference of the seed pulse with the circulating intracavity pulse, which means that the optical length of the cavity must directly correspond to the pulse repetition rate of the laser system, which requires active stabilization. The feedback signal for the Pound-Drever-Hall type stabilization [130] is the laser light which is reflected from the input coupler and its the phase-modulated sidebands generated in the EOM in the preamplifier.

The power which is reflected by the input coupler is minimal and the intra-cavity power maximal if cavity length and repetition rate are in agreement. In the MEGAS system this is implemented in two ways: Fast deviations are corrected by moving a mirror of the titanium-sapphire seed oscillator and thus changing slightly the repetition rate. Slower drifts which accumulate to significantly larger distances are accounted for by translating one of the enhancement cavity mirrors by up to 10  $\mu\text{m}$ .

The intracavity power can be determined by measuring the power, which leaks through one of the cavity mirrors with previously determined transmission properties (Fig. 3.2). In the current setup, we measured an intracavity power of up to 3.0 kW in the empty cavity and 2.4 kW when generating high harmonics in argon at an intra-cavity pulse duration below 50 fs.

The precision of cavity mirror coatings is particularly crucial because small deviations in phase or reflectivity sum up at each roundtrip. It is not necessary to maintain the spectral phase of the circulating pulse identical after each reflection but after each roundtrip, such that the sum of the spectral phases of all optical components in the cavity is as linear as possible. Because the fabrication process is not sufficiently precise to guarantee the necessary phase requirements, the phase of each cavity mirror is individually measured by spatial spectral interferometry [131]. Based on these measured spectral phases, a set of mirrors from different coatings and coating runs can be combined to achieve a well-controlled roundtrip phase.

For most applications it is sufficient to have a linear spectral phase and minimal losses in each roundtrip, but some experiments additionally require carrier envelope phase control, such as the generation of isolated attosecond pulses [132]. In the case of intra-cavity HHG for RABBITT, CEP stability does not play a notable role because each attosecond pulse train

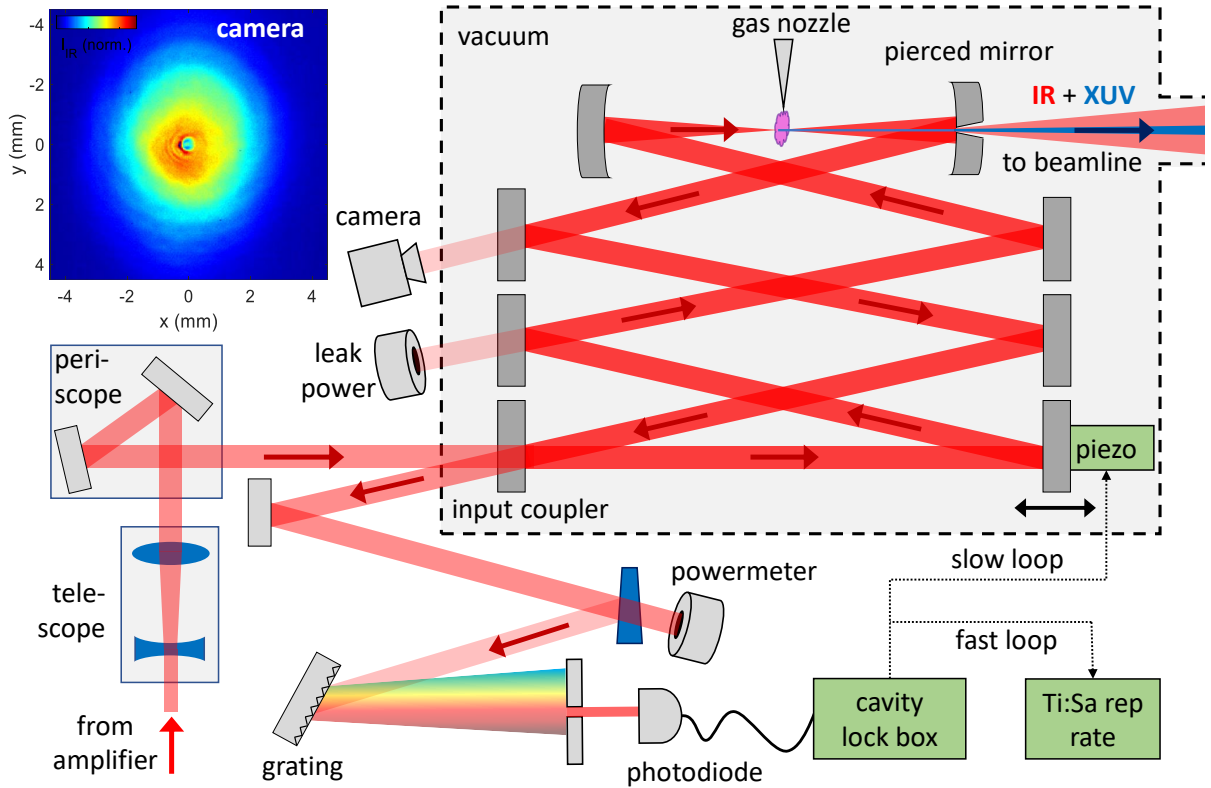


Figure 3.2: Schematic representation of the enhancement cavity setup. A telescope and a periscope are used to match and align the seed beam with the cavity mode. High harmonics are generated in the focus of the cavity and output coupled through a hole in a cavity mirror. Leaks through cavity mirrors are used to determine the intracavity power and to image the pierced mirror (inset on the left). The IR power, which is reflected from the input coupler is monitored by a powermeter and a part of it is monochromatized by a grating and a slit and detected by a photodiode to serve as input signal for the Pound-Drever-Hall cavity lock. Enhancement cavity length and the oscillator pulse repetition rate are controlled in a slow and fast loop respectively to ensure their synchronicity.

consists of many XUV pulses of comparable intensity which are intrinsically synchronous to the IR electric field they were generated from. Hence, it is sufficient to adjust the  $f_{\text{ceo}}$  of the laser to the so-called optimum-offset frequency (OOF) of the cavity, which is determined by the CEP slippage that the intra-cavity laser pulse acquires at each roundtrip (Section 2.1).

The OOF of the cavity can easily be determined experimentally by adjusting the  $f_{\text{ceo}}$  of the laser such that the intra-cavity power is maximal when the cavity is locked. The current cavity OOF is -9.7 MHz. The  $f_{\text{ceo}}$  of the laser is controlled by means of a pair of motorized glass wedges within the oscillator cavity and monitored over a spectrum analyzer showing the beatnote measured in the f-to-0f interferometer in the oscillator box.

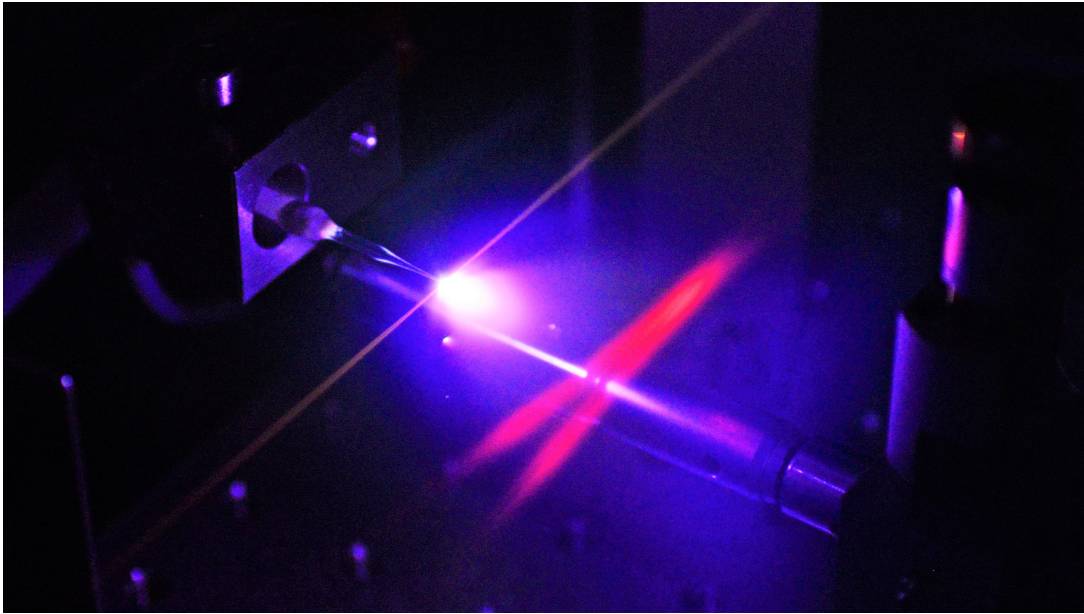


Figure 3.3: Photo of the HHG gas target in operation. Argon atoms streaming out of the end-fire nozzle (on the left of the picture) are ionized in the IR focus, keep propagating and emit light upon recombination (bright cone-shaped purple cloud). The excited HHG gas atoms travel to two crossing IR cavity beams which excite fluorescence (red crossing beams). The generated XUV photons also ionize gas atoms on their way (thin orange beam). Photo taken by Thorsten Naeser.

### 3.2.2 Intra-cavity high harmonic generation

The HHG gas target consists of a thin fused silica end-fire nozzle which is located close to the cavity focus (Fig. 3.3). It can be self-made from a glass tube with a gas burner or obtained from a commercial supplier<sup>5</sup>. Although the material is transparent, it is inevitably heated in the close vicinity of a kW-laser beam, which is why only fused-silica nozzles were used. Other types of glass with lower melting point quickly deform. For high harmonic generation in argon, a nozzle with a 200- $\mu\text{m}$  diameter was used and yields optimum photon flux at around 3.5 bar of backing pressure. Because the phase matching-pressure in neon is significantly higher and the vacuum pumps<sup>6</sup> have only limited pumping capacity, smaller nozzles of 50- $\mu\text{m}$  diameter were used for neon HHG at backing pressures of 10 to 20 bar.

The XUV radiation cracks residual hydrocarbons in the vacuum chamber which can lead to the deposition of carbon and a reduced reflectivity of the cavity mirrors. Therefore, the three cavity mirrors after the focus are constantly purged with ozone<sup>7</sup> during high harmonic generation. The ozone reacts with the hydrocarbons on the mirrors and evaporates them to

<sup>5</sup>Hilgenberg GmbH, Malsfeld, Germany

<sup>6</sup>Edwards iXL120 dry pump and Edwards STP-iXR1606 turbo molecular pump

<sup>7</sup>generated by Anseros COM-AD-01-IP

prevent carbon contamination.

The cavity input coupler has a transmission of 3% which is comparably high for an enhancement cavity. A lower transmission would enable a higher finesse which could allow for higher intra-cavity circulating power. However, previous studies have shown that it is more advantageous for intracavity HHG to rely on lower finesse and higher seed power due to the intensity-clamping effect in nonlinear enhancement cavities (Section 2.3.2).

Because no material is sufficiently transmissive for the generated XUV photons, they cannot be coupled out through a cavity mirror and it is challenging to implement a solution which has a high output coupling efficiency for the XUV without introducing major losses for the circulating IR pulse. XUV output coupling by reflection from a Brewster plate [60, 61] and diffraction from an XUV nano-grating [133, 134] are suitable for lower photon energies but suffer both from very low efficiencies at photon energies above  $\sim 30$  eV. Geometrical output coupling schemes such as higher order cavity modes [67, 132] or non-collinear HHG [135] have also been demonstrated and could be a way to boost output coupling efficiencies in future cavity-based HHG sources, particularly for high photon energies. However, these approaches are intrinsically not intended to output couple IR and XUV light simultaneously, which can be a disadvantage for XUV-pump IR-probe experiments.

The MEGAS cavity employs another geometrical output coupling scheme through a tiny hole in one of the cavity mirrors, which was proposed in 2006 [136] and has been promoted and developed by the MEGAS collaborators since then [24, 67, 127]. Since the divergence of the XUV is much smaller than for the IR, a significant share of the high harmonics can be output coupled through the hole with minor IR losses. Detailed theoretical and experimentally cross-checked studies over a wide range of HHG parameters predict an output coupling efficiency on the order of 10% for our cavity geometry [137].

The IR cavity leak through the hole is intrinsically perfectly synchronous to the XUV and can be utilized for pump-probe experiments. Moreover, this approach is particularly well suited for high photon energies exceeding 100 eV [24, 127]. We currently employ an output coupling mirror with a 340- $\mu\text{m}$ -diameter laser drilled hole which was developed and fabricated by the MEGAS collaborator of the ILT [138].

The resulting HHG spectra measured with an XUV spectrometer are depicted in Fig. 3.4a and b. For HHG in argon, the spectrum spans from 30 eV to more than 60 eV photon energy. High harmonics generated in neon range from 30 eV to more than 100 eV. The higher photon energies in neon HHG come at the cost of significantly lower flux. The measured neon HHG XUV power of 140 nW (above 60 eV) is almost three orders of magnitude lower than a total of 60  $\mu\text{W}$  for argon HHG.

Fig. 3.4c gives an overview over the XUV photon flux of state-of-the-art HHG sources based on titanium-sapphire lasers, ytterbium-fiber lasers and enhancement cavities. The MEGAS XUV source clearly sets new standards for the photon flux at high repetition rates, particularly for high photon energies of 40 eV and above. High repetition rates are crucial for space-charge free photoemission measurements (Section 5.1) and high photon energies are needed to access deeply bound core states in solids as demonstrated in this work (Section 6.2).

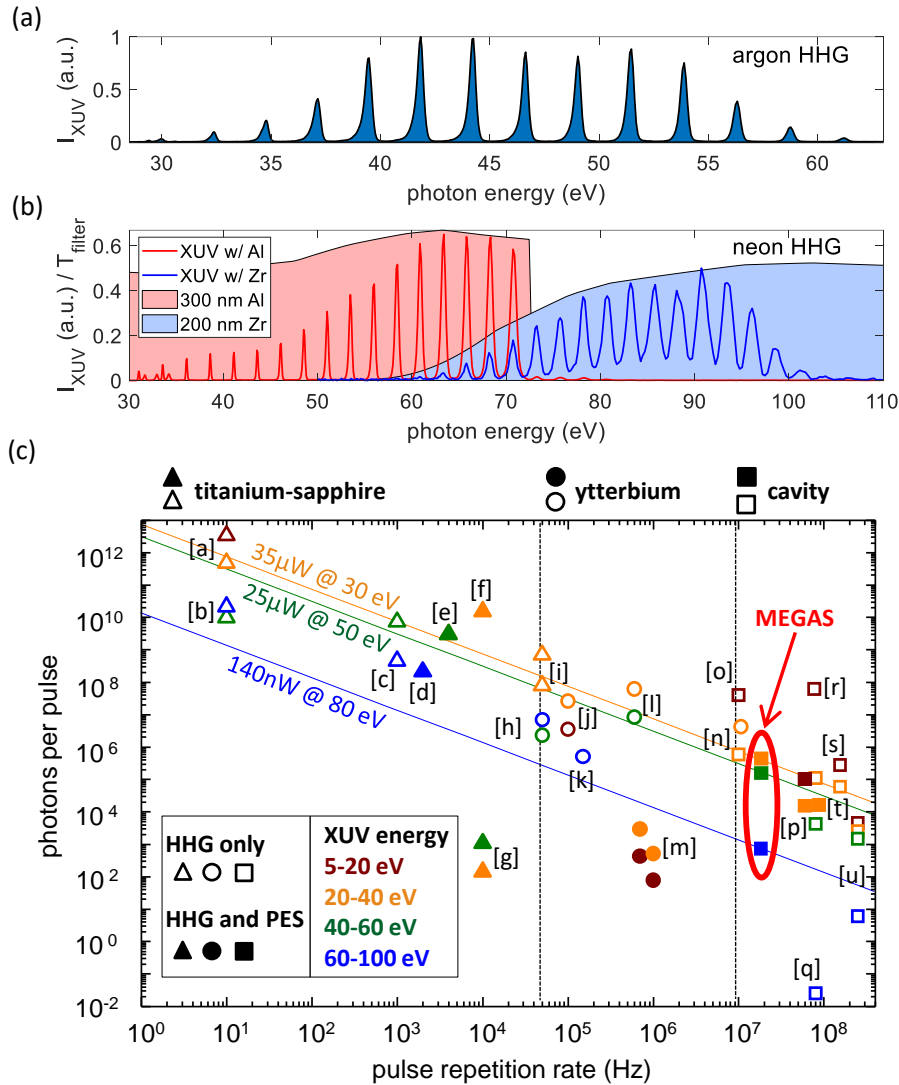


Figure 3.4: **a)** XUV spectrum generated in argon measured with a 300-nm aluminum filter. **b)** XUV spectra generated in neon measured with a 300-nm aluminum and zirconium filter respectively and corresponding filter transmission curves. **c)** Overview of XUV photons per pulse and pulse repetition rates of state-of-the-art HHG sources. The HHG sources can be attributed to three different types of HHG technology: titanium-sapphire and ytterbium fiber-based laser systems and enhancement cavities. They separate the data points in three repetition rate ranges and are recognizable by symbol shape. Diagonal lines indicate equal XUV average power with the MEGAS source used in work (red encircled data points). Our system sets new standards in photon flux for MHz HHG sources, particularly for photon energies of 40 eV and more. XUV sources which have been used for PES experiments are represented by filled symbols.

Figure c) adapted from Ref. [24] under the terms of the [Creative Commons Attribution 4.0 International License](https://creativecommons.org/licenses/by/4.0/). HHG source references: a [139], b [140], c [141], d [121], e [142], f [143], g [144], h [63], i [145], j [62], k [146], l [147], m [148], n [149], o [150], p [151], q [67], r [133], s [37], t [152], u [127].

### 3.3 Attosecond beamline

The design and setup of the attosecond beamline was an important experimental task of this thesis and is thus described here in detail. The beamline fulfills three functions: Diagnosis and filtering of the IR and XUV beam and creating a pressure gradient between HHG chamber and the PES chamber.

#### 3.3.1 Vacuum and differential pumping

The beamline extends over a total length of 213 cm which is necessary due to the high pressure difference which has to be bridged between 0.01 to 0.1 mbar in the HHG chamber (due to the HHG gas load) and ultra-high vacuum conditions of  $10^{-9}$  to  $10^{-8}$  mbar in the experimental chamber to minimize sample contamination. A three-stage differential pumping setup was designed and set up as a part of this thesis to meet this requirement. It features three pipes connecting the HHG chamber, two ConFlat-100 (CF) crosses with a turbo-molecular pump each, and the experimental chamber (Fig. 3.5).

The connecting pipes are designed as thin and long as possible to prevent gas flowing from the high-pressure side to the low-pressure side of the pumping stage. Mathematically this is described by the conductivity of piping  $C$  which is defined as quotient of the gas throughput  $q_{pV}$  and pressure difference  $\Delta p$ . In the molecular flow regime, the conductivity of a pipe is [153, p. 107]:

$$C_{\text{pipe}} = \frac{v_{\text{mol}} \cdot \pi \cdot d^3}{12 \cdot l} \quad (3.1)$$

Here,  $d$  and  $l$  are the diameter and length of the pipe and  $v_{\text{mol}}$  the thermal velocity of the gas atoms and molecules, which is 464 m/s for air at room temperature. Because the conductivity scales with  $d^3$  it is crucial to keep the pipe diameters as small as possible. The final pressure  $p_1$  in the first differential pumping stage is determined by the gas leak rate and the vacuum pump and is well approximated by the following expression:

$$p_1 \approx \frac{p_{\text{hhg}} \cdot C_{\text{pipe}}}{S_{\text{pump}}} \propto \frac{d^3}{l} \quad (3.2)$$

It depends on the pressure in the HHG chamber  $p_{\text{hhg}}$  and the pump throughput  $S_{\text{pump}}$  and is proportional to the conductivity of the pipe connecting it to the HHG chamber. The calculation is identical for the next two differential pumping stages, and the simplifications remain valid as long as the calculated pressure is significantly larger than the base pressure of the chamber without additional gas flow through the beamline.

Hence, it is key for a large pressure gradient that the length  $l$  of the employed pipes is as long as possible and even more importantly their diameter  $d$  as small as possible. The divergence of the 1030 nm IR beam after diffraction at the 340  $\mu\text{m}$  outcoupling hole is 7 mm per meter propagation. Consequently, the diameters of the tubes were chosen to match the diameter of the IR beam at every point along the beamline, such that the beam could pass the beamline

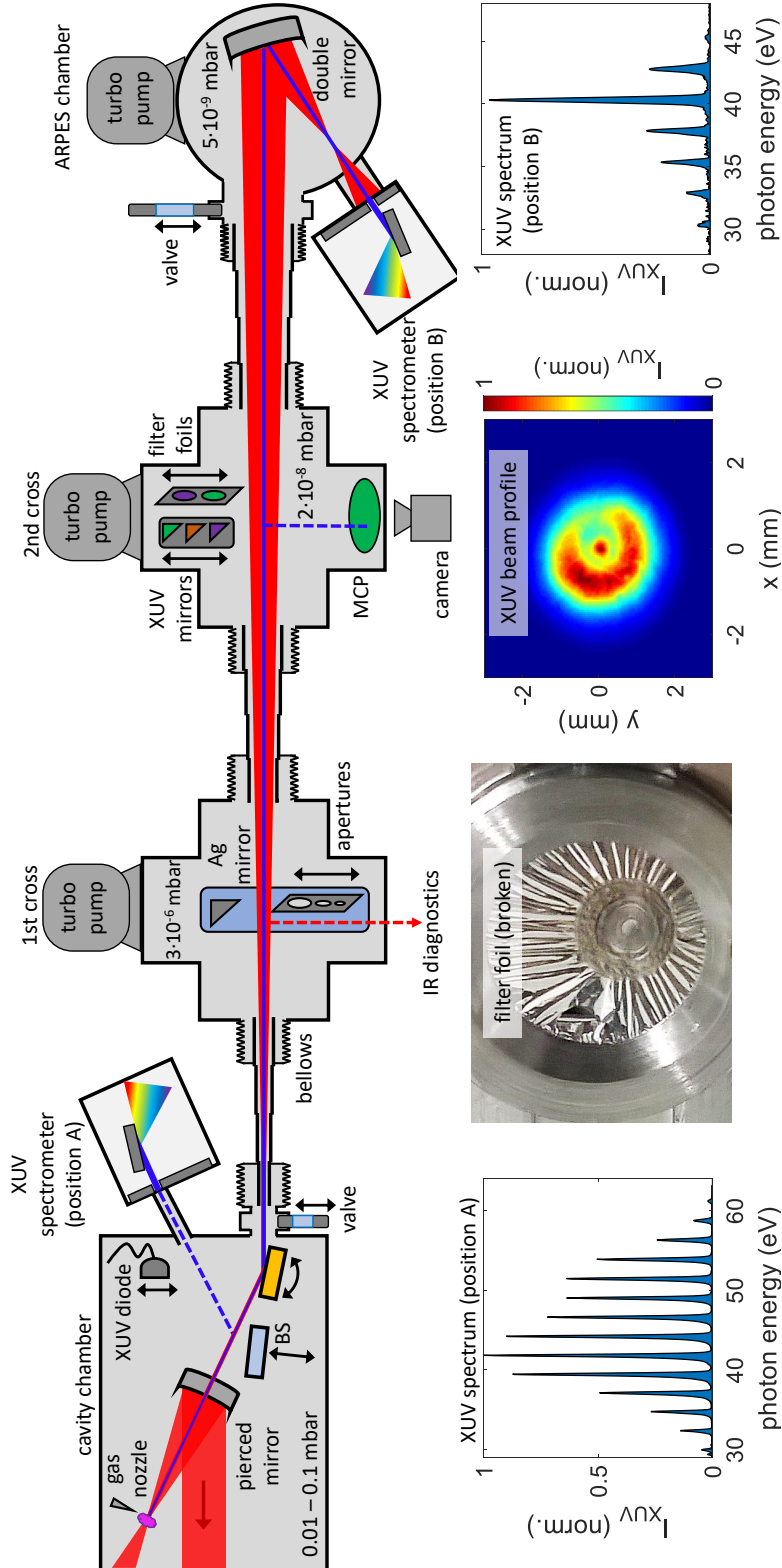


Figure 3.5: Attosecond beamline setup. XUV and IR are coupled out through a hole in a cavity mirror and steered into the beamline. A XUV-IR beam splitter can be used to direct the high harmonics to a XUV spectrometer (position A; XUV spectrum as inset below). An XUV diode can be introduced into the beam to measure the XUV power. Pipes, whose inner diameter increases with the diameter of the divergent IR beam connect the 3 differential pump stages. The IR beam can be coupled out from the beamline in a first CF100-cross by 45° mirror or the IR power can be reduced by clipping the beam with apertures of 2 to 6 mm diameter. The second CF100-cross features metal foil filters and 45° XUV mirrors to direct the XUV on an MCP with phosphor screen and image the XUV beam profile (see inset below). Below is a photo of a damaged aluminum foil filter, where the circular IR beam diffraction pattern was burned into the foil. In the ARPES chamber the XUV is spectrally filtered by the double mirror and the resulting XUV spectrum can be detected by a spectrometer (position B; XUV spectrum as inset below).

without clipping or significant diffraction. Within each tube, the diameter increases in 1-mm steps accordingly.

The differential pumping pipes are connected to the vacuum chambers and CF-100 crosses with flexible steel bellows (Fig. 3.5) and each pipe is mounted at two points on x-y-linear stages which enable full position and orientation control of the pipes to ensure that they can be perfectly aligned with the laser beam without clipping it.

The 255-l/s turbo-molecular pumps<sup>8</sup> in each differential pumping stage bring the pressure down from around 0.01 to 0.1 mbar in the HHG-chamber (for argon and neon HHG respectively) to  $3 \times 10^{-6}$  mbar in the first stage,  $2 \times 10^{-8}$  mbar in the second stage and in the  $10^{-9}$ -mbar range in the experimental chamber, which is pumped by a 685-l/s turbo-molecular pump<sup>9</sup>.

To be able to vent the individual parts of the setup separately, vacuum gate valves separate the XUV spectrometer from the setup and the beamline from the HHG chamber and the experimental chamber. The beamline gate valves feature a window such that the laser beam can be used for alignment if a part of the setup is vented and one or two valves are closed. All connections of the beamline and the ARPES chamber are ConFlat flanges with copper sealings to guarantee ultra-high vacuum conditions with minimal leakage. For the cavity chamber ISO-K flanges are used which are fully sufficient for this high-vacuum part of the setup.

### 3.3.2 Beam diagnostics and filter

Depending on the intended use, an XUV spectrometer<sup>10</sup> can be set up either directly behind the cavity chamber to characterize the generated XUV spectrum or behind the ARPES chamber to measure the XUV reflected from the focusing XUV mirror as it impinges on the sample (Fig. 3.5). In the first case, a motorized stage in the HHG chamber allows for moving an IR-XUV beam splitter [127] into the beam path which directs the high harmonics to the spectrometer. This enables the characterization of the unfiltered generated spectrum and flux optimization at the desired photon energy in real time. If the spectrometer is mounted to the ARPES chamber, the sample has to be moved out of the beam path to characterize the XUV. The beam diameter is very large at this point due to its high divergence after the focus of the double mirror. Therefore, integration times of several minutes are necessary for the acquisition of a meaningful XUV spectrum at this position.

Two metal foil filters mounted each on a vacuum gate valve in front of the XUV spectrometer suppress the residual IR light: A 300-nm thick Al filter for photon energies below 73 eV and a 300 nm Zr filter for higher photon energies (see also Fig. 3.4b). To calibrate the spectrometer energy axis, several approaches have been combined: Sharp absorption edges of filters, e.g. at 73 eV in aluminum or at 100 eV in silicon can be used for absolute calibration of certain points in the spectrum. Moreover, the constant energy spacing between the high harmonics or often visible second order diffraction peaks can be used to adjust the energy axis in between and

---

<sup>8</sup> Pfeiffer HiPace 300

<sup>9</sup> Pfeiffer HiPace 700

<sup>10</sup> McPherson DO240A-BN-995

beyond those points. The resulting XUV spectra are in very good agreement with XUV mirror reflectivity curves, which corroborates the calibration.

Motorized linear stages<sup>11</sup> in the first and second CF-100 cross are used to insert mirrors, filters or apertures into the beam path (Fig. 3.5). All of them are high-vacuum or ultra-high vacuum compatible and feature an optical position encoder with nanometer resolution to ensure reproducible positioning of the mounted optical elements. The stages are mounted on rings fitting into the CF-100 pipes and hold in place by set screws.

The first CF-100 cross contains a silver mirror on a linear stage which can direct the IR beam through a window flange mounted on the side of the cross. This enables the direct characterization of the intracavity laser pulse for example by a spectrometer, a beam profile camera or an autocorrelator. A set of apertures with 2-, 3-, 4- and 6-mm diameter on a stage in the second cross allows to clip the IR beam to reduce the IR beam power and hence control the probe pulse intensity at the target. This can be necessary if RABBITT sidebands exhibit higher order oscillations as shown in Section 4.4.

The XUV beam profile can be measured by a microchannel plate (MCP) detector with phosphor screen mounted on the top flange in the second CF-100 cross. Three different 45°-XUV mirrors with reflectivity curves centered at 40, 60 and 90 eV can be inserted into the beam path and direct the beam to the MCP. The detector phosphor screen is imaged by a CCD camera and allows for XUV profilometry (Fig. 3.5) as well as a first estimation of the XUV flux and spectral envelope.

A set of 50 to 300 nm thick filter foils<sup>12</sup> such as silicon, aluminum, carbon or zirconium can be inserted in the beam in order to block the IR light and spectrally filter the XUV according to their individual characteristic transmission properties. However, the high average power of the IR laser proved to be critical for the filters and repeatedly destroyed them within seconds. The necessity for high laser powers of typically 5 to 10 W in the beamline is a consequence of the high repetition rate: RABBITT experiments ideally require probe intensities of around  $10^{11}$  W/cm<sup>2</sup> for a well-modulated sideband signal. Since our repetition rate is about three orders of magnitude higher than in kHz-repetition rate HHG systems, the average laser power increases by the same factor.

Due to their thinness, the metal foil filters cannot dissipate the absorbed laser energy by thermal conductivity but only by radiation. This explains, why clipping the outer parts of the IR beam by apertures could not overcome the problem of breaking foils. Because the XUV beam is in the center of the IR beam where its intensity is highest the foil filters heat up locally and break. For comparison, the 3 mm thick tungsten crystal in the ARPES chamber is heated by the laser up to 700°C (Section 3.4.5), a temperature which is already above the melting point of aluminum. This also explains, why some aluminum filters turned transparent, because only a thin layer of optically transparent aluminum oxide was left as depicted in the filter photo in Fig. 3.5. Zirconium, carbon and silicon filters proved to be even more fragile under these extreme circumstances.

---

<sup>11</sup>two *SmarAct* SLC-24180 and one *SmarAct* SLC-1760

<sup>12</sup>*Lebow Company*, California, USA

To overcome this problem, the steering mirror in between the pierced cavity mirror and the beamline has to be replaced by an uncoated glass substrate or even an IR-XUV beam splitter [127] to reduce the impinging laser power. Since the IR power is needed for time-resolved measurements to provide a sufficiently strong probe field, this can only be done for static measurements and the exchange of the mirror requires venting the cavity chamber. For future experiments a more flexible solution will be implemented. This can be done, by mounting the IR-XUV beam splitter together with the gold steering mirror in the cavity chamber on a motorized stage or by employing significantly thicker filter foils, which comes at the cost of reduced XUV flux.

To monitor the correct positioning of the beamline pipes, the apertures and the coaxial filter as well as the IR beam profile and power, the IR beam reflected from the tungsten crystal in the ARPES chamber was directed through a viewport, refocused by a lens and captured by a beam profile camera equipped with suitable filters or by a powermeter (Fig. 3.5).

### 3.3.3 XUV transmission and reflectivity losses

A motorized unprotected gold mirror at a grazing angle in the HHG chamber is used to steer the beam from the cavity into the beamline (Fig. 3.5). The initial setup featured two such mirrors at  $10^\circ$  grazing incidence, which introduced XUV losses of more than 60% according to calculations based on Ref. [154]. In the context of this work, the focusing mirror axis of the cavity was positioned at an angle with the beamline and only one mirror at  $3^\circ$  grazing angle was used for beam steering. By this, the losses could be reduced to about 15%, which corresponds to more than twice the photon flux of the initial design. One steering mirror proved to be sufficient for the occasionally necessary realignment of the beam with respect to the beamline and the ARPES chamber. Moreover, the distance between pierced mirror and beamline is now minimized to about 60 cm in order to avoid reabsorption of the high harmonics by the background HHG gas atoms.

Figs. 3.6a and b show the losses introduced by the XUV optics from the generation of the high harmonics to the experimental chamber for HHG in argon and neon. It includes a 300-nm aluminum foil filter, as it was used for all photoelectron experiments presented in this thesis (Section 3.4.3). The foil filter suppresses XUV above the Al absorption edge of 73 eV. If higher photon energies were required, other foil materials like zirconium or silicon could be used.

Since the high phase-matching pressure for neon HHG leads to a background pressure of 0.1 mbar in the cavity chamber, 70 to 90% of the generated XUV is absorbed by neon atoms during the propagation of the beam to the beamline entrance. For HHG in argon at lower backing pressures, the absorption in 0.01 mbar is only notable at photon energies between 15 and 40 eV. The actual absorption in the HHG gas is probably even higher because of the higher pressure around the HHG gas nozzle. Moreover, it can be assumed that oxygen atoms from the ozone in the cavity chamber and thin oxide layers on the filter foils additionally suppress lower photon energies, whose outcoupling efficiencies through the pierced mirror are also generally lower [137].

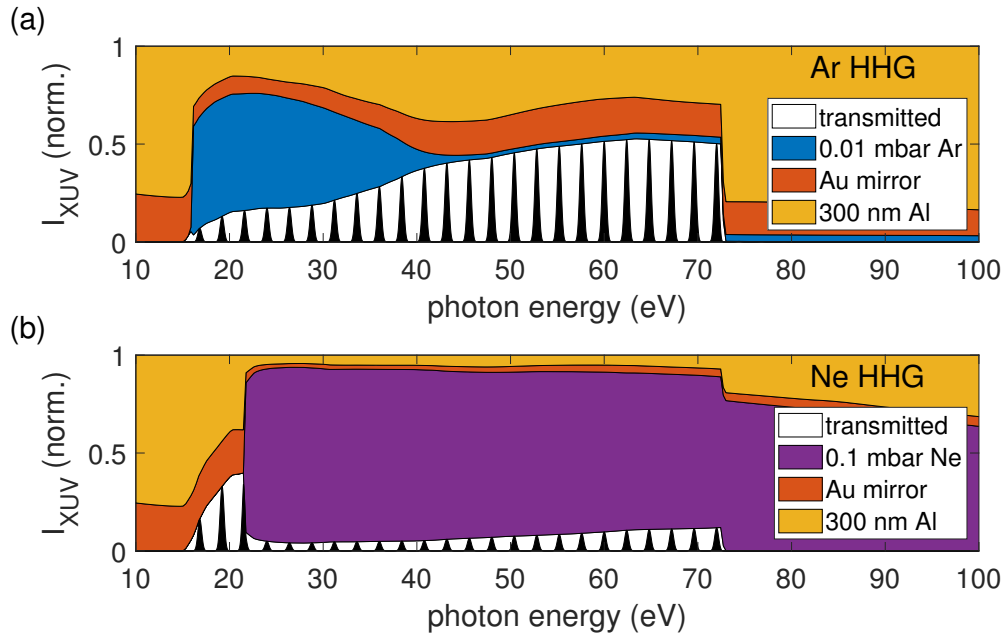


Figure 3.6: Portions of the generated XUV, which are lost due to absorption in gas, filter and mirrors along the beam path for HHG in argon and neon displayed in **a)** and **b)** respectively. The losses arise from absorption in the HHG gas background pressure, a 3°-grazing angle gold mirror and a 300-nm aluminum foil filter applied in this order. The total transmitted XUV power is shown by black high harmonics on white background. Reflectivities and absorption coefficients taken from [154].

### 3.4 ARPES chamber

The presented ARPES setup was conceived and built for kHz-PES experiments [108,155] and has experienced a few improvements and modifications for experiments at MHz pulse repetition rates in the course of this thesis. The next section gives an overview of the experimental chamber setup and the subsequent sections a more detailed description of the individual components.

#### 3.4.1 Chamber setup overview

The experimental vacuum chamber is of cylindrical shape with 50 cm inner diameter and numerous CF-flanges oriented towards the sample position, which is located in its center (Fig. 3.7). The collinear IR and XUV beams enter the experimental chamber from the beamline and are spatially separated by a coaxial foil filter into a central XUV beam and a donut shaped IR beam around it. The delay between these two beams is introduced by a two-segment mirror which also spectrally filters the XUV and focusses the beam on the sample.

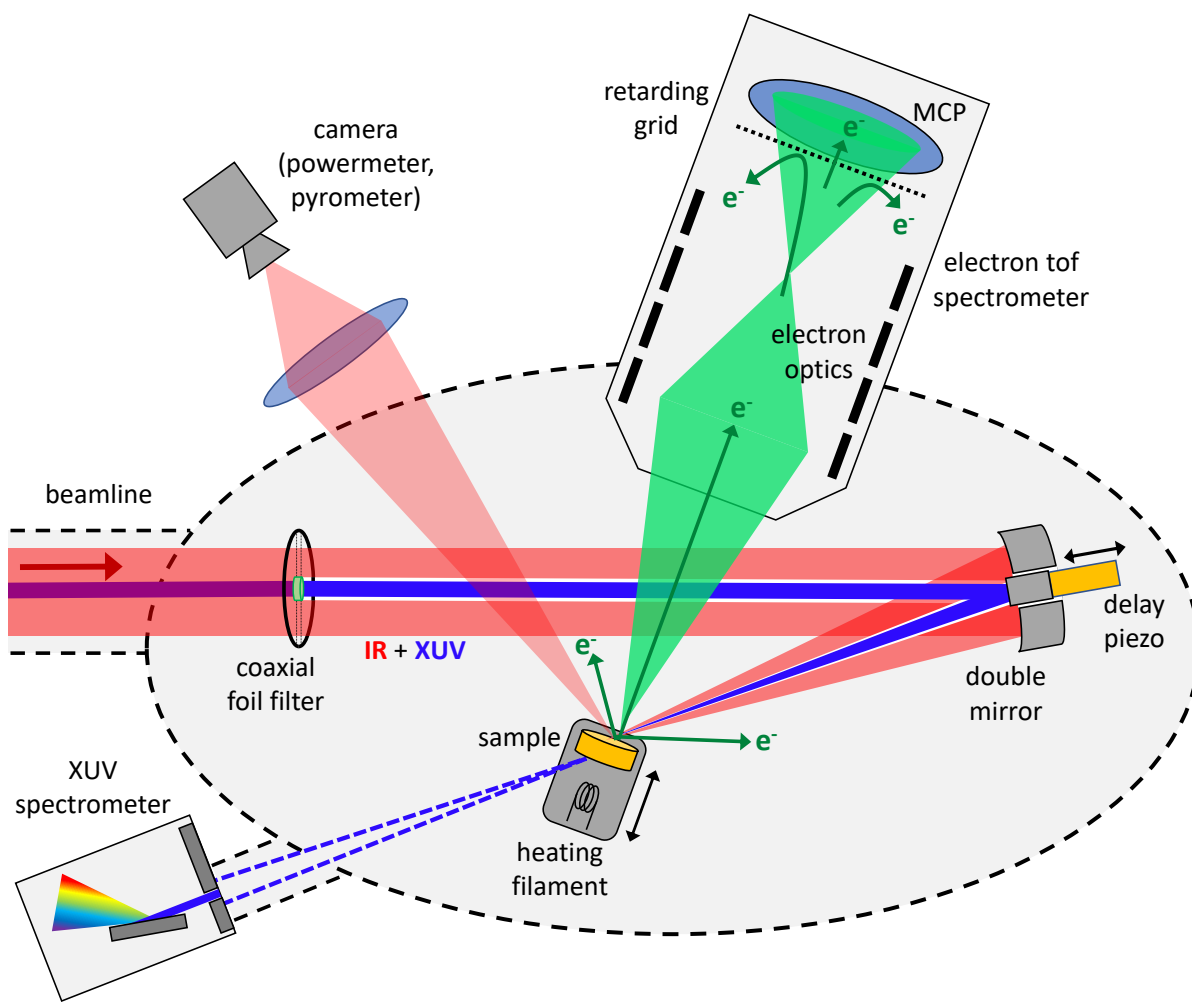


Figure 3.7: XUV and IR beam enter the experimental chamber from the beamline with different beam diameters. A 300-nm aluminum thick foil in the center of the beam blocks the IR light and separates XUV and IR spatially. The double mirror introduces a delay between the two beams and focuses them on the target. Photoelectrons emitted from the W(110) sample crystal are captured by the ToF spectrometer and their emission angles are imaged on the MCP detector by electrostatic lenses. A retarding grid cuts off slower electrons in front of the detector. The IR light, which is reflected from the tungsten crystal surface, can be used to image the IR focus or measure the average laser power. The viewport is also used for monitoring the sample temperature with a pyrometer. A filament behind the crystal serves as electron source, which is used to clean the sample surface by means of electron impact heating. The high-harmonic spectrum can be measured with an XUV spectrometer when the sample is retracted from the beam path.

The sample holder is mounted on an x-y stage<sup>13</sup>. An extra degree of freedom was realized in the course of this thesis by adding a rotation stage<sup>14</sup> to the setup which allows for the detection of photoelectrons from a wide range of emission angles. The positioners are optically encoded and motorized to guarantee the reproduceable exact positioning of the sample. The correct sample position is determined by the electron spectrometer<sup>15</sup> which demands a fixed working distance of 53.3 mm from its entrance opening to the sample. It is an angle-resolving time-of-flight spectrometer and captures and detects electrons within an acceptance angle of up to  $\pm 15^\circ$ .

Photoelectrons can be deflected by magnetic and electric fields on their way from the sample into the electron spectrometer, which is magnetically shielded by mu-metal. This is particularly detrimental for angle-resolved measurements as these fields would change the initial electron momentum. To minimize their influence, magnetic materials and insulators are avoided in the vicinity of the sample. Moreover, the static magnetic field at the sample position, which is mainly attributed to the Earth's magnetic field, is corrected in three dimensions by three sets of coils around the vacuum chamber. To this purpose, a home-built 3-axis teslameter is used, whose calibration process indicates a precision of less than  $1 \mu\text{T}$ . A sample preparation chamber equipped with an electron impact heating setup and an ion sputtering gun can be connected to the experimental chamber and the sample transferred to it with a wobble stick and a transfer rod.

### 3.4.2 Coaxial foil filter

For pump-probe experiments, the XUV and IR must be delayed with respect to each other which requires spatial separation between them. Just as for the cavity outcoupling, this is achieved by making use of the different divergence of the two beams. Compared to the IR, the wavelength of the XUV is by around two orders of magnitude smaller and consequently also its divergence. A thin metal foil filter placed in the center of the IR beam is mostly transparent for XUV but blocks the IR completely. Hence, the two coaxial beams can be separated into an XUV beam in the center and a donut-shaped IR beam around it. This approach is a well-established technique in attosecond physics.

Because of the high average laser power the design and positioning of the coaxial filter had to be adapted to the challenges that come along with MHz-attosecond PES. In many kHz-beamlines, the filter foil in the center of the beam is held in place by a pellicle membrane of a few  $\mu\text{m}$  thickness and the entire coaxial filter is often referred to as pellicle. However, such a membrane cannot withstand the high average IR power in the MEGAS setup. Therefore, the central foil filter is suspended by two wires running across a frame ring of one-inch inner diameter (Fig. 3.8a). The central filter consists of a 300-nm aluminum foil glued between two aluminum rings of 3 and 5 mm inner and outer diameter respectively. To position the coaxial

---

<sup>13</sup> *SmarAct* SLC-2460 and SLC-24120

<sup>14</sup> *SmarAct* SR-5714C

<sup>15</sup> *SPECS* Themis 1000

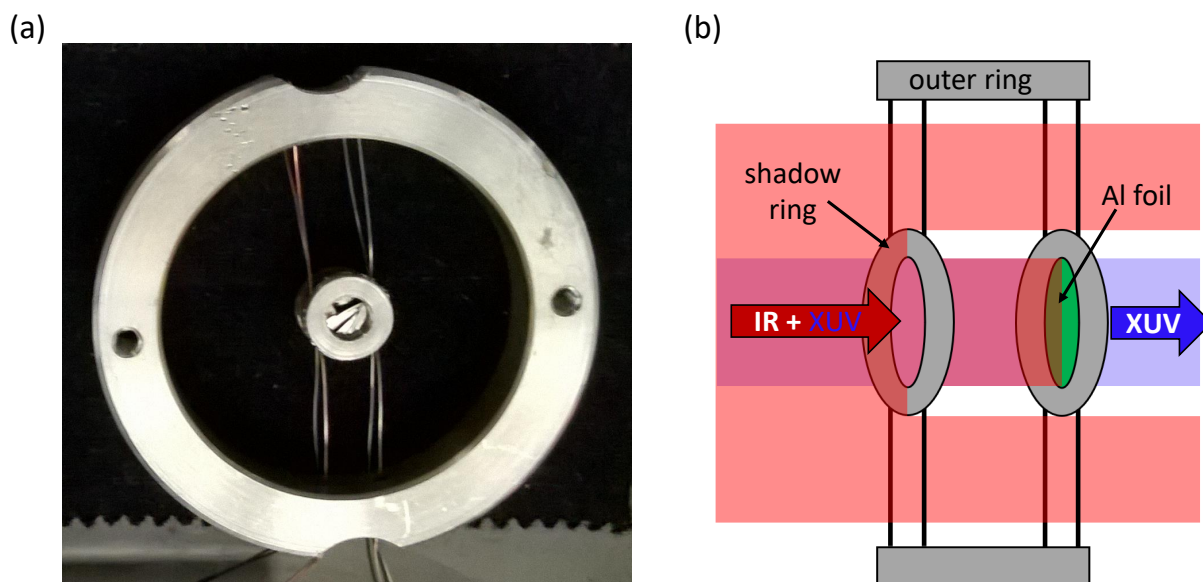


Figure 3.8: **a)** Front view of the coaxial filter (with broken aluminum foil). **b)** Coaxial foil filter/pellicle setup. A 300-nm thick aluminum foil filter is glued onto a ring and suspended by two wires in a larger outer diameter ring. Another small identical ring is mounted in front of the foil ring and casts a shadow on it to reduce the heat load. The filter separates the IR and XUV in an outer and inner beam.

filter precisely in the center of the beam or to entirely remove it from the beam path, it is mounted on an encoded x-y translation stage<sup>16</sup>.

However, this coaxial filter also suffers from the issue of frequently breaking filter foils due to the high IR laser power (Section 3.3.2). A thicker filter would come at the cost of reduced the photon flux and a nickel support mesh on the filters was not able to solve the problem. To reduce the IR intensity impinging on the metal foil, the coaxial filter was moved from the beamline to the ARPES chamber where the beam has its maximum size and therefore the least power within its central 3-mm diameter, which is covered by the foil filter. Furthermore, a duplicate of the ring, to which the filter foil is glued, was placed right in front of the coaxial filter to block the IR from the mounting ring of the filter foil and thus reduce the heat load on it (Fig. 3.8b). Together, these measures proved to be sufficient to prevent the filter foil from breaking.

### 3.4.3 Double mirror interferometer

After passing the coaxial filter, the two spatially separated beams impinge each on a segment of the so-called double mirror which consists of a round core segment of 5 mm diameter and

<sup>16</sup>*SmarAct* SLC-24120 and SLC-1760

an outer ring around it. The two segments are cut<sup>17</sup> from the same super-polished 1-inch mirror substrate<sup>18</sup>. The inner segment is an XUV multilayer mirror<sup>19</sup> mounted on a piezo crystal<sup>20</sup> to provide a variable pump-probe delay. The outer segment is gold coated to offer a high reflectivity for the IR beam. The mirror segments have a 250 mm radius of curvature, are oriented at a 5° incidence angle of the beam and the reflected beams are focused on the sample surface.

The entire double mirror setup features a total of 8 motorized actuators<sup>21</sup> to provide all necessary degrees of freedom. Particularly, the ability to tilt the outer mirror segment independently from the inner one is necessary, to overlap the two reflected beams on the target. The light which is reflected from the sample crystal exits the chamber through a viewport and is used to image position and shape of the two foci with a lens on a camera with a magnification of around five. Due to the donut-shape of the IR beam and the astigmatism introduced by the 5° incidence angle on the double mirror, the spatial profile of the IR focus is significantly distorted as shown in Fig. 3.9a. Simulations based on the apertures and optical elements along the beam path confirmed that this is inherent to the current setup (Fig. 3.9b).

Because the focus of the outer mirror features only low on-axis intensity, higher sideband modulation in RABBITT-traces is observed, when the XUV focus overlaps with one of the off-axis maxima of the IR focus from outer mirror segment. Since the rest of the IR light does not contribute to the probe field strength but represents a significant heat load to the sample and the optical components along the beam path, it would be desirable to aim for a better focus quality for future experiments, especially with samples which do not withstand high temperatures as well as tungsten. One possibility to implement this, could be an off-axis aperture which cuts a rounder beam out of the IR donut profile.

Temporal overlap between the two beams is established without the coaxial filter and by illuminating both mirror segments with IR light. After overlapping the beams spatially, the delay between the beams is varied until a delay dependent interference pattern can be observed on the CCD camera (Fig. 3.9c). The maximal modulation depth of the pattern indicates the zero-delay position.

When illuminating the inner mirror segment with the IR beam special care must be taken to not expose it to too much laser light. Because of the high laser power and the comparably low IR reflectivity of the inner mirror its nanometer-thin layers could be corrupted and the reflectivity behavior significantly affected. The spatial overlap can be established without cavity lock but finding temporal overlap requires short pulses which are only provided by a locked cavity.

The evaluation of measured RABBITT sideband delays (Section 4) showed that there was a significant drift in the pump-probe delay during the measurement (Fig. 3.10a). The direction of the drift indicated, that the inner mirror segment moved towards the incoming beam over

---

<sup>17</sup>substrates cut by *Korth Kristalle GmbH*, Altenholz, Germany

<sup>18</sup>*Gooch and Housego Moorpark*, California, USA

<sup>19</sup>designed and fabricated by Alexander Guggenmos and Yang Cui

<sup>20</sup>*Physikinstrumente P-620 UHV*

<sup>21</sup>seven *Newport Spectra-Physics GmbH 8301-UHV Picomotors* and one *Physikinstrumente L-509*

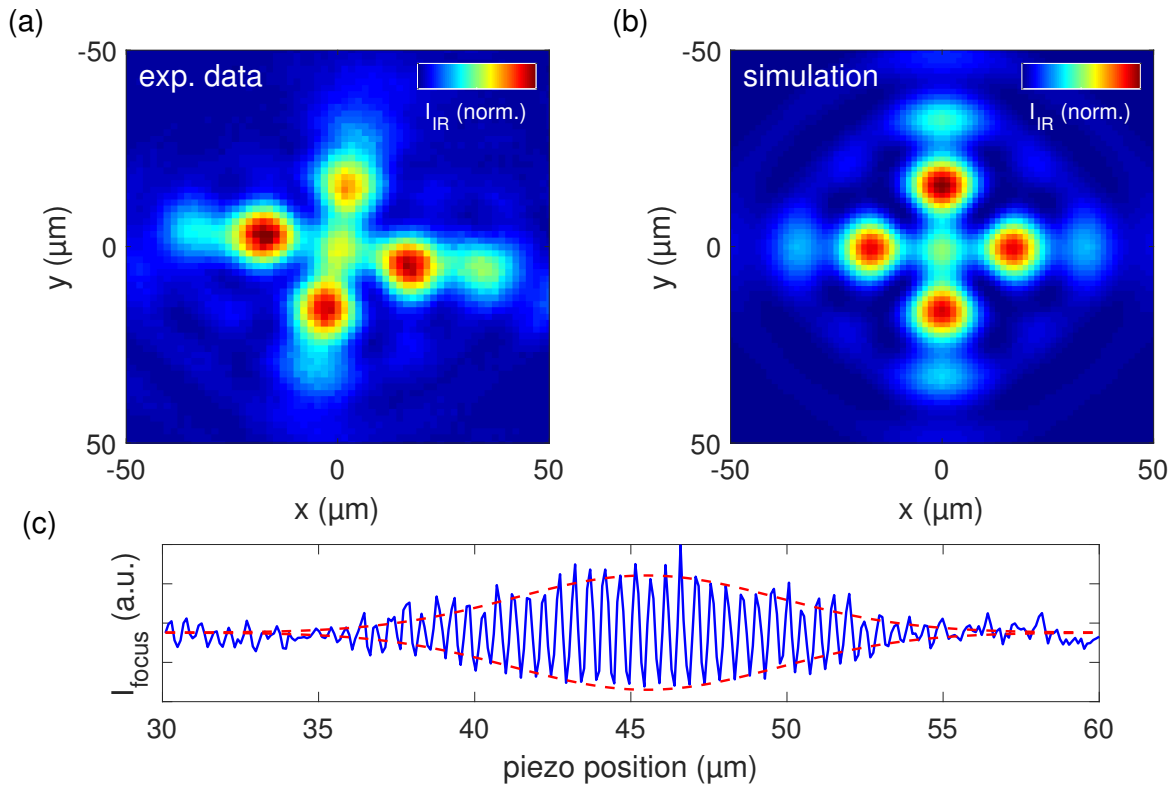


Figure 3.9: **a)** Spatial profile of the IR double-mirror focus (outer mirror segment). Astigmatism of the focusing mirror and the donut-shaped IR beam lead to this cross-shaped focus. Because the sample was presumably not on the exact same height as the incoming beam, the symmetry axis is slightly tilted. **b)** Numerical calculation of IR double-mirror focus after coaxial filter and focusing mirror. The simulation is based on code provided by Maximilian Högner. **c)** Intensity at the overlap of the foci from inner and outer mirror segment as function of the double-mirror delay piezo position. The maximum of the interference modulation depth is located around  $46\ \mu\text{m}$ , which corresponds to zero delay position between the two mirror segments.

the first 2 or 3 minutes of a measurement. This was attributed to thermal expansion of the aluminum bolt to which the inner mirror segment is glued, which is heated by IR stray light. It has only little mass and thermal contact to the rest of the setup and the inner mirror segment is not designed to be reflective for stray IR light. The bolt material was replaced with Invar36, a nickel-iron alloy whose thermal expansion coefficient of around  $10^{-6}\ 1/\text{K}$  is more than an order of magnitude smaller than for aluminum [156]. As a result, this drift effect did not impair the measurements any more.

Another much slower delay drift of inverse direction was observed during the continuous measurement of dozens of RABBITT traces over several hours (Fig. 3.10b). It could be attributed to thermal expansion of the outer mirror segment, which occurs on a much longer timescale because the reflectivity of the outer mirror segment is much higher and the mass and thermal

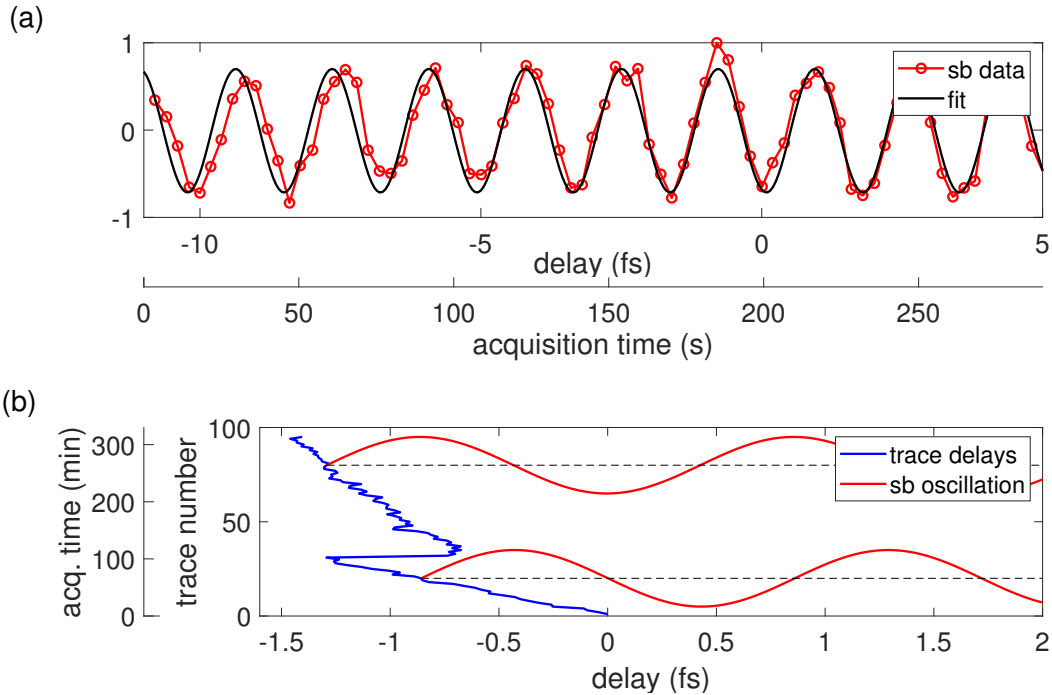


Figure 3.10: **a)** Delay drift within a RABBITT sideband during the acquisition of a spectrogram. A fit to the second half of the sideband data points (black solid line) reveals a drift of the interferometer of around 30 nm within the first 150 s of the measurement. Afterwards, the sideband period remains constant and is in good agreement with the fit. The drift is attributed to thermal expansion of the inner mirror segment and its mount. **b)** Long-term drift of the interferometric double-mirror delay during the acquisition of 95 spectrograms. The drift was extracted from the sideband delays in the RABBITT traces and spans 1.4 fs over a total measurement time of 320 minutes. After 31 traces, a 70-minute measurement break leads to a jump in the delay. The drift could be attributed to thermal expansion of the outer mirror segment and its mount. Note, that the acquisition-time ordinate is only correct for the first and last trace and is linearly interpolated in between.

contact of its mount is significantly larger. A 22-mm diameter aperture was placed in front of the double mirror to mitigate stray light but this could not fully suppress this effect.

Due to its slowness this drift is not particularly harmful to the measurement result of a single RABBITT spectrogram, which is typically taken within two to three minutes. However, when combining different trace, it has to be accounted for this kind of delay drift as it is described in Section 4.2. An approach to extract delays between RABBITT sidebands from measurements with free running XUV-IR delay has been proposed recently [157] and could be employed to mitigate the influence of any kind of delay drifts in future experiments.

In the course of time-resolved PES measurements within the scope of this thesis it proved to be absolutely crucial to find the right distance between sample and focusing mirror. Deviations

of only around 100  $\mu\text{m}$  from the correct position impair significantly the intensity of the RABBITT sidebands, which quickly disappear completely at larger offsets. The first step to find the right sample distance is by illuminating the sample with IR light only and detect the emitted above-threshold-ionization electrons. By translating the mirror on a motorized stage, the sample-mirror distance is varied until number and energy of the ATI electrons is highest which marks the point of the maximum IR intensity. However, the distance for optimum RABBITT sideband modulation was often found to differ by more than 1 mm from this point which could be attributed to the distorted spatial profile of the focus.

#### 3.4.4 Angle-resolved time-of-flight photoelectron detection

The time-of-flight electron spectrometer<sup>22</sup> used for all photoelectron measurements in this thesis features an electron lens system which images the electron emission angles onto its imaging grade microchannel plate electron multiplier. The electron signal from the MCP is then detected by a delay line detector (DLD) which allows for simultaneous measurement of the impact point on the detector and the arrival time of each electron [158]. This is realized by a pair of meandering wire electrodes behind the MCP which are orientated perpendicular to each other. In each of these two electrodes the passing electron cloud generates electronic signals whose arrival time is measured at both ends of both wires. The time of the electron impact can then be calculated from the mean arrival times of the detected signals and its x- and y- position from the arrival timing difference between the two ends of each electrode.

Subsequently, the 2D electron emission angle and kinetic energy of a detected electron is calculated from its point of impact on the detector, its time of flight and the applied electron lens voltages. To determine the time of flight of an electron, it is necessary to know its emission and its arrival time. The latter is measured by the DLD and the first can be determined from XUV photons which are scattered from the sample crystal onto the DLD detector. These photons are detected and form a peak which marks the moment when the photoelectrons are emitted, the so-called ‘time zero’.

The spectrometer offers several different operation modes, three of which have been used in the course of this thesis: Drift mode (DM), low-angular-dispersion mode (LAD) and wide-angle mode (WAM). Drift mode is particularly useful for intuitively understandable measurements because it does not apply any voltages to the electronic lens system. The electrons drift from the sample to the detector without any deviations or acceleration. Consequently, the acceptance angle of  $\pm 1.3^\circ$  is geometrically determined by the size of the detector and its distance from the sample and the velocity of the detected electrons is simply calculated as quotient of sample-detector distance and time of flight. This mode is particularly useful for making measurements with high energy resolution, where the detection of a larger emission angle range is not necessary or desired.

LAD and WAM are used for angle-resolved measurements over a wider acceptance angle range from which electrons are collected and imaged onto the detector by the electrostatic

---

<sup>22</sup>SPECS Themis 1000

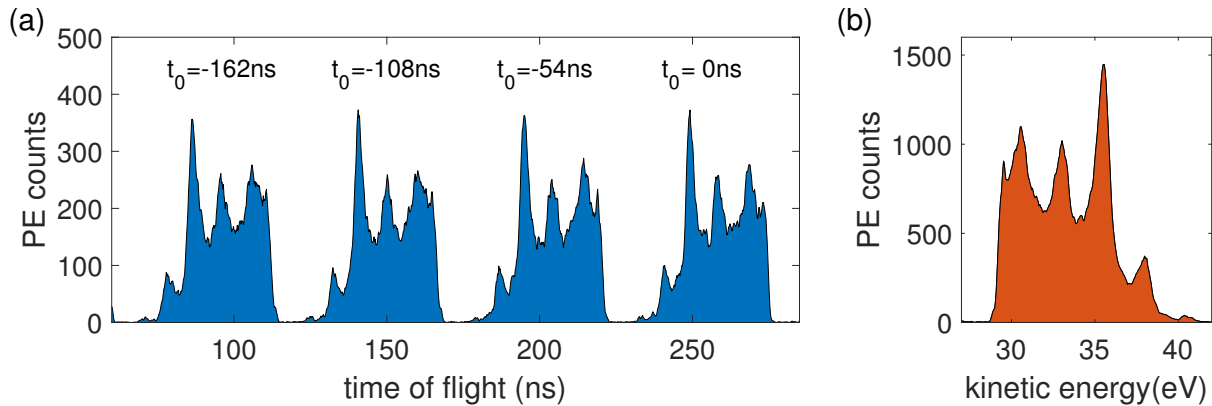


Figure 3.11: **a)** Raw photoelectron time-of-flight spectrum detected by the spectrometer with a frequency-divided trigger signal. The rightmost spectrum around 250 ns was emitted at 0 ns time of flight, the other three spectra each 54 ns before the one on their right. Slower electrons beyond the sharp edge in each spectrum (e.g. at 275 ns) are cut off by a retarding grid to limit the maximum ToF-dispersion to less than 54 ns. **b)** Photoelectron spectra from a) summed up and converted to electron kinetic energy. The retarding grid voltage of -29 V can be directly read from the sharp edge in this photoelectron spectrum.

lenses. Their acceptance angle is  $\pm 7^\circ$  (LAD) and  $\pm 15^\circ$  (WAM), respectively. Because the electron optics are subject to chromatic aberration, the energy resolution of these modes is lower than for DM and depends mainly on the width of the kinetic energy range, which is to be detected.

At 18.4 MHz pulse repetition rate, the time between two subsequent laser pulses is only 54 ns. However, the electron time of flight from the sample to the detector is at our kinetic energies and typical lens settings on the order of at least 200 ns. This means that between the emission of a photoelectron and its arrival at the detector, photoelectrons from several previous laser pulses are detected, which can make the attribution of the electrons to a corresponding emission moment 'time zero' ambiguous. To avoid that slow photoelectrons are overtaken by faster ones emitted from subsequent laser pulses, a counter voltage is applied to a grid in front of the MCP (Fig. 3.7). It repels all electrons whose kinetic energy is too low to overcome the grid voltage which is chosen such that the time-of-flight dispersion between the fastest and slowest photoelectrons remains below the 54 ns (Fig. 3.11a). The resulting sharp cutoff in the photoelectron spectrum and its known energy can then be used to relate the photoelectrons unambiguously to one of the previous time-zero peaks.

The trigger signal for the time-of-flight measurements is provided by a photodiode which detects the light transmitted through a mirror in the laser amplifier system. Because the spectrometer electronics do not support trigger signals of more than 5 MHz, a frequency divider was used to reduce the trigger frequency by a factor of 4 to 16. This results in a set of photoelectron spectra within the trigger period, which is then summed up to a single spectrum with a common time zero (Fig. 3.11b).

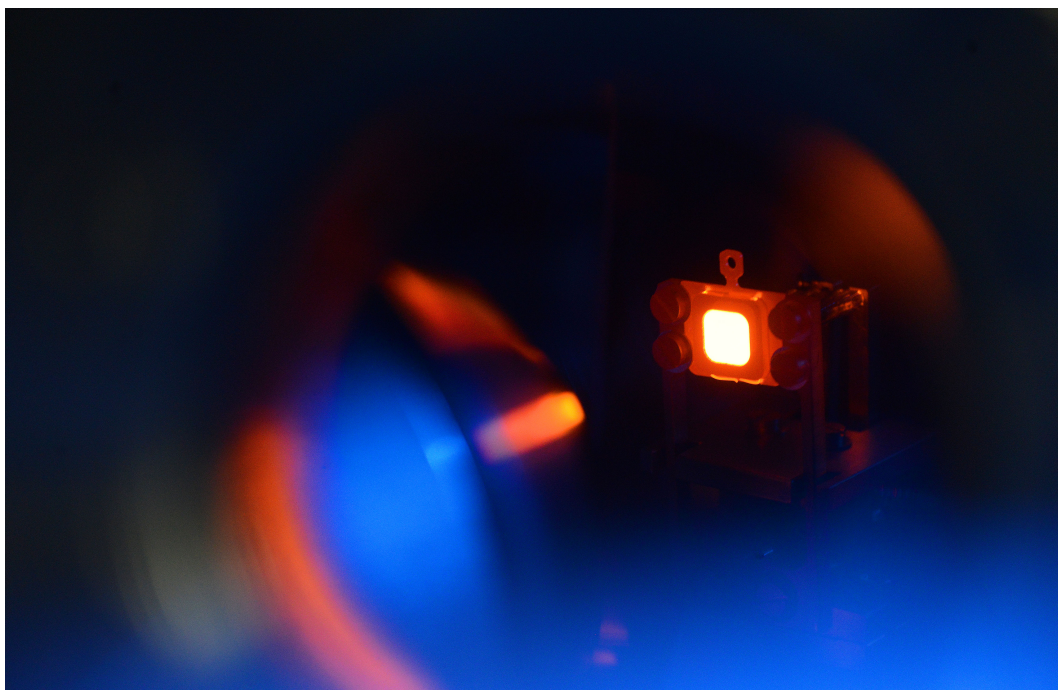


Figure 3.12: Glowing tungsten crystal in its flag-style sample holder seen through a view port in the ARPES chamber. Here, it is cooling down after a 2000°C-flash to vaporize contamination from the surface. Photo taken by Thorsten Naeser.

### 3.4.5 Tungsten crystal preparation

The sample crystal is held in a flag-style sample holder which allows electron impact heating from its backside. A filament behind the sample provides an emission current of 200 mA which is heating the sample up to 2000°C within a few seconds at an acceleration voltage of 1.1 kV<sup>23</sup> (photo in Fig. 3.12). This is made possible by the design of the mount with little mass and thermal contact to the breadboard in the chamber. The parts of the assembly which are close to the sample crystal are made of molybdenum, because it is non-magnetic and withstands high temperatures.

Because predominantly photoelectrons from less than a nanometer below its surface leave a solid without being inelastically scattered [86], it is crucial to ensure the cleanliness of the crystal surface and to remove oxides or other compounds and adsorption layers regularly. The tungsten crystal cleaning procedure consists of several flashes at 1000°C in an oxygen atmosphere to remove carbides from the sample surface followed by a single flash at 2000°C in ultra-high vacuum or argon atmosphere to remove oxides as described in Ref. [159]. The sample temperature is monitored by a pyrometer<sup>24</sup> through one of the viewing ports and the cleaning procedure was typically repeated roughly every 60 minutes.

<sup>23</sup>voltage and filament current supplied by *Tetra Combi Power Supply*

<sup>24</sup>*Maurer KTRD 1075-1*

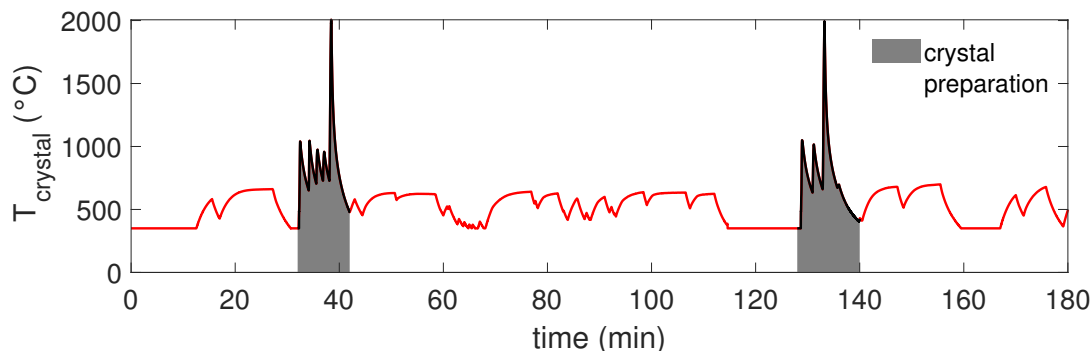


Figure 3.13: Tungsten crystal temperature during the measurement process measured by a pyrometer (with a minimum measurable temperature of 350°C). Over the depicted period, the sample was cleaned twice by electron impact heating with several high-power flashes at 1000°C and a single one at 2000°C (gray filled area). Outside these crystal preparation cycles, the temperature increases, when the cavity is locked and the sample crystal is exposed to high laser power. Laser induced heating is saturating at 630°C in this measurement. Between the PES measurements, the cavity is not locked and the temperature decreases.

To delay the inevitable recontamination of the cleaned crystal surface over time by adsorption and reaction with impinging atoms and molecules it is desirable to keep the experimental chamber at ultra-high vacuum pressure below  $10^{-8}$  mbar. However, we found empirically that the sample contamination is significantly slowed down by a constant argon gas flux into the experimental chamber. Consequently, the chamber background pressure was held at  $10^{-6}$  mbar argon atmosphere. Supplying argon during the sample cleaning procedure also seemed to lead to better results.

A possible explanation for this phenomenon could be, that the argon gas mitigates the migration of molecules and atoms from the cavity chamber and the beamline into the experimental chamber. Because several components in the cavity chamber are not ultra-high vacuum compatible and additional oxygen is supplied by the ozone purging of the mirrors, it represents a potential source of contamination for the experimental chamber.

Because the sample crystal is during the pump-probe experiments permanently exposed to an IR laser power of up to 10 W and absorbs around 64% of it at a 60°-angle of incidence [160] it is heated to temperatures of up to 700°C within only a few minutes of measurement time with a locked cavity (Fig. 3.13). Although this can favor the generation of compounds as tungsten carbide (Section 6.4) it seems also to prevent contamination from adsorption and particularly oxidation as the characteristic chemical shifts of the 4*f* electron binding energy for tungsten oxides could not be observed in our experiments. The high heat load could become a problem for less resistant samples in future experiments. Possible approaches to overcome this issue it will be discussed in Chapter 7.

## 3.5 Measurement routine

Particularly the time-resolved photoelectron spectroscopy measurements require many repetitions to obtain a meaningful dataset for the extraction of photoemission delays with high precision as described in Section 4.2. Therefore, stable operation over several hours or even days is desirable. The measurement routine with an enhancement-cavity based HHG source differs in some points from regular single-pass HHG systems and several things must constantly be observed and corrected if necessary.

One of these tasks is the maintenance of the cavity-lock. Because of the high laser powers thermal effects inevitably impair the alignment of the cavity mirrors over time. Although this phenomenon decreases over time in long-term measurements it is still notable even after many hours of constant operation and manifests in different ways:

One significant drift concerns the cavity length, which is constantly increasing during the measurement. During a lock this is compensated for by a piezoelectric linear stage which adjusts the cavity length. However, the drift exceeds the maximum piezo range of  $10\ \mu\text{m}$  typically roughly after 20 minutes of operation, which limits the maximum lock time. After each lock, the acquired length drift is compensated by another linear stage, which has a longer travel range than the piezo but is not precise enough to be used for the lock. Hence, the piezo can be set to zero position again, to be able to compensate the change in length which occurs during the next cavity lock.

Another thermal-drift effect concerns the overlap between the incoming laser beam and the cavity mode. This can be caused by drifts of the seed beam as well as misalignment of the cavity mirrors. To compensate for it the last two mirrors of the seed laser outside of the cavity chamber are used to manually walk the beam into perfect overlap with the cavity mode. This should usually be done after every cavity lock to ensure a stable and long-lasting lock with high intra-cavity power.

In the course of the continuous slow misalignment of the cavity mirrors, also the position of the cavity mode on the pierced mirror changes over time. It is monitored by a camera imaging the laser light from the pierced mirror, which leaks through the following cavity mirror (Fig. 3.2) and is typically adjusted when the XUV or photoelectron flux decreases notably. It is corrected by tilting one of the cavity mirrors and subsequently reestablishing the overlap between seed and mode by beam-walking the seed beam.

The positioning of the HHG nozzle is also very sensitive and is subject to drifts of the nozzle or the cavity mode. For HHG in argon, the nozzle position is usually only optimized once per day, in the case of neon HHG several times per day. This is due to the higher necessary phase-matching pressure in neon, which means that the nozzle should be placed closer to the beam, where it is exposed to more laser light.

The measurement of time-resolved photoelectron spectrograms is done by a Labview program, which controls the piezo responsible for the pump-probe delay and saves all detected photoelectrons of each delay step in a separate file. The delay scans are automatically performed alternately in increasing and decreasing delays over the same delay range.

For each detected electron, the raw time and x-y coordinates of impact on the DLD are

recorded. Therefore, each event takes up 4 bytes of memory space in the raw data. At a photoelectron count rate of more than  $10^6$  electrons per second a large amount of data is collected and has to be processed. Because of memory limitations, the Labview measurement script only supports up to two million counts per delay step, which limits the integration time for each step but proved to be sufficient for the measurement of meaningful RABBITT traces. The processing of the acquired data leads to a dead time of approximately 1 s after each delay step.

For further data analysis, the x-y-t coordinates of each photoelectron are converted to the photoelectron emission angles and kinetic energy  $\alpha$ - $\beta$ - $E_{\text{kin}}$  according to a conversion matrix calculated from the spectrometer lens settings and time zero. Because of the large amount of collected data, it is necessary to process and convert it to well-manageable histograms. Including the pump-probe delay of each measured photoelectron spectrum, this results in 4-dimensional datasets. The data was converted and binned with Labview script and further processed and visualized with Matlab in specifically designed scripts.

# Chapter 4

## Methodology - RABBITT analysis and illustration

This chapter is dedicated to the methods which were applied in this thesis to display RABBITT spectrograms in an illustrative and meaningful way, extract photoemission delays from a RABBITT datasets and account for spectral phases introduced by the XUV optics.

### 4.1 Spectrogram illustration

The visibility of the modulated sideband pattern in a RABBITT spectrogram from a solid target depends strongly on the IR intensity but also on other experimental parameters like sample material, contamination, acceptance angle, XUV spectrum and electron kinetic energy.

Particularly at lower kinetic energies the photoelectron spectra are dominated by a background of secondary electrons, which have been scattered inelastically before leaving the sample material. This background is irrelevant for the evaluation of the sideband delays which is done either by fitting of sine curves or by Fourier analysis except for additional noise. The spectrogram in Fig. 4.1a illustrates how secondary electrons can cover a RABBITT trace to an extent where almost no sideband modulations can be seen by eye.

For this reason, it is helpful to subtract a delay independent background from a RABBITT spectrogram, to highlight the relevant features of its characteristic pattern and spot possible anomalies. Removing the constant component of the spectrogram in the Fourier space highlights the sideband modulation, but makes it impossible to distinguish sidebands from high harmonic peaks, which are also oscillating due to depletion. A linear combination of Fourier filtering and the subtraction a smoothed average spectrum overcomes this issue (Fig. 4.1b).

In order to make the graphic representation pleasing to the eye, it is common to interpolate points for a smoother appearance of the data (see Fig. 4.1c). All measured RABBITT spectrograms in this thesis are background subtracted and contain interpolated points as described in this section and their color scale will represent the normalized photoelectron counts and be identical to the one in Fig. 4.1a unless explicitly stated differently.

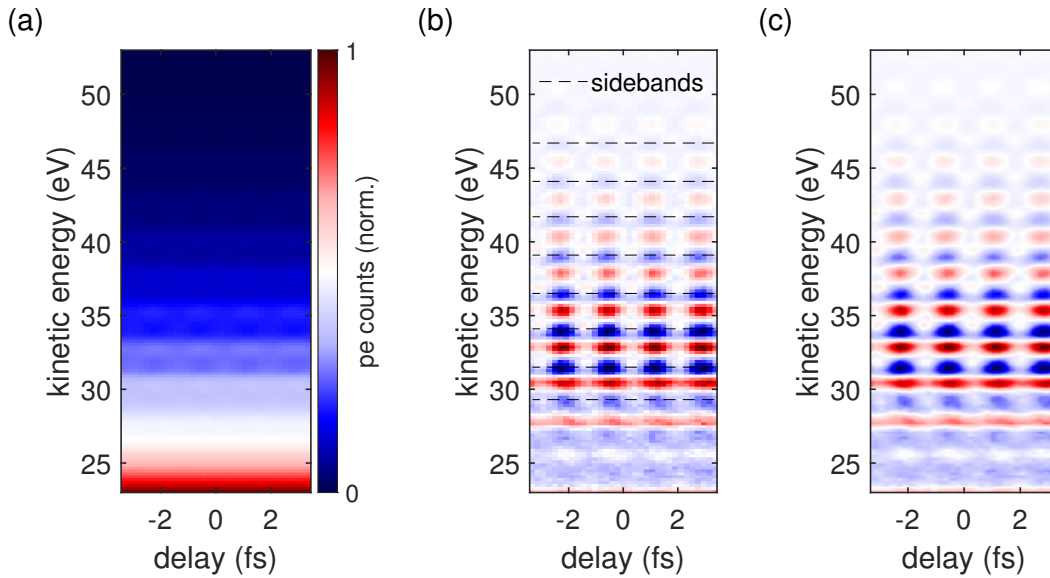


Figure 4.1: **a)** Measured raw RABBITT spectrogram. **b)** Spectrogram from a) after subtraction of a delay-independent background. The background is chosen such that it emphasizes the sideband oscillations and makes sidebands (predominantly blue and additionally indicated by dashed lines) and high harmonics (predominantly red) clearly distinguishable from each other. **c)** Spectrogram from b) after interpolation from 33 delay steps and 150 energy bins to  $500 \times 750$  points. The dataset consists of 33 delay steps of 208 as and was measured within a total net acquisition time of 195 minutes.

## 4.2 Sideband delay evaluation and error bars

The RABBITT data presented in this thesis consists of sets of traces measured under identical experimental conditions and acquired within one or two consecutive days. Because the sample can be contaminated over time and to prevent detrimental influences from drifts in delay or in the XUV spectrum, the individual spectrograms are measured within 2 to 4 minutes and alternating in increasing and decreasing delay. Hence, the datasets consist typically of several tens of individual spectrograms which are all combined to extract photoemission delays with high accuracy. The spectrogram displayed in Fig. 4.1 is for example composed of 68 individual traces, one of which is shown in Fig. 4.2a.

To extract the sideband delay from a spectrogram, all photoelectrons in an interval of  $\pm 0.25$  eV around the central sideband energy are summed up to a linecut. The position and the width of the sideband linecuts are indicated by colored bars on the right side of Fig. 4.2a and the corresponding datapoints (and fits) in identical colors in Fig. 4.2b. According to Eq. 2.35 a sine function is fitted to these sidebands:

$$SB = a_1 \cdot \cos(2\omega_{\text{IR}} \cdot a_\tau) + a_2 \quad (4.1)$$

Here, the free fit parameters are  $a_1$ ,  $a_2$  and the total sideband delay  $a_\tau$  which comprises the pump-probe delay, the photoemission delay and the spectral phase of the neighboring sidebands (see Eq. 2.35). The IR laser frequency  $\omega_{\text{IR}}$  was experimentally confirmed to be  $2\pi/3.44$  fs in numerous spectrograms, which is in perfect agreement with the measured laser central wavelength of 1030 nm. Whereas the pump-probe delay is unknown, but equal for all sidebands in a spectrogram, the photoemission delay and spectral phase delay depend on sideband order and initial or final state (Section 2.4.4). For this reason, only relative delays between the sidebands with an unknown overall delay offset are extracted from a spectrogram. Fig. 4.2c illustrates how a delay between two exemplarily selected sidebands from Fig. 4.2a is determined. Here, the red sideband is shifted to the left by 172 as with respect to the blue one which indicates a larger sideband delay.

After the evaluation of the delays of all sidebands in all 68 traces of the dataset, their mean values are the sideband delays extracted from the entire dataset, their standard deviation their error bars. The values thus obtained are displayed in Fig. 4.1d together with histograms indicating the distribution of the delays in the dataset for each sideband.

As the XUV-IR delay turned out to be notably drifting between the measurement of the individual traces, it is necessary to account for this effect, when determining the delay mean values and standard deviations. This is done by summation over all sidebands in each trace and fitting a sine curve to this sideband sum. The result of this procedure is displayed in Fig. 4.1e and shows a clear drift in delay over the acquisition of the 68 traces of the dataset. A significant jump interrupting the uniformity of the curve is observed after trace number 36 and can be attributed to a 50-minute interruption in the measurement procedure. Because the delay drift is negative, it is attributed to thermal expansion of the of the outer mirror segment and its mount due to laser stray light on the mirror mount and light absorbed by the outer mirror segment itself (Section 3.4.3).

Because the individual spectrograms are noisy and sometimes hardly meaningful to the human eye, it makes sense to sum over all individual traces of an entire dataset to obtain a clear RABBITT trace as presented in Fig. 4.1c. Therefore, the individual traces have to be shifted by their total sideband delay (determined as described above). This is done by stitching a part of one side of the spectrogram to the other. Because the delay intervals of the spectrograms in this thesis were chosen to be integer multiples of the sideband periods, this is possible without disturbing the regularity of the RABBITT pattern.

However, this was only done for illustration and first visual examination of the dataset. The evaluation of the actual sideband delays and their error bars is exclusively based on the values extracted from the individual (unshifted) traces. The spectrograms in Fig. 4.1 and all other measured spectrograms in this thesis, which consist of a set of traces, were obtained by the above described procedure of summation over shifted spectrograms.

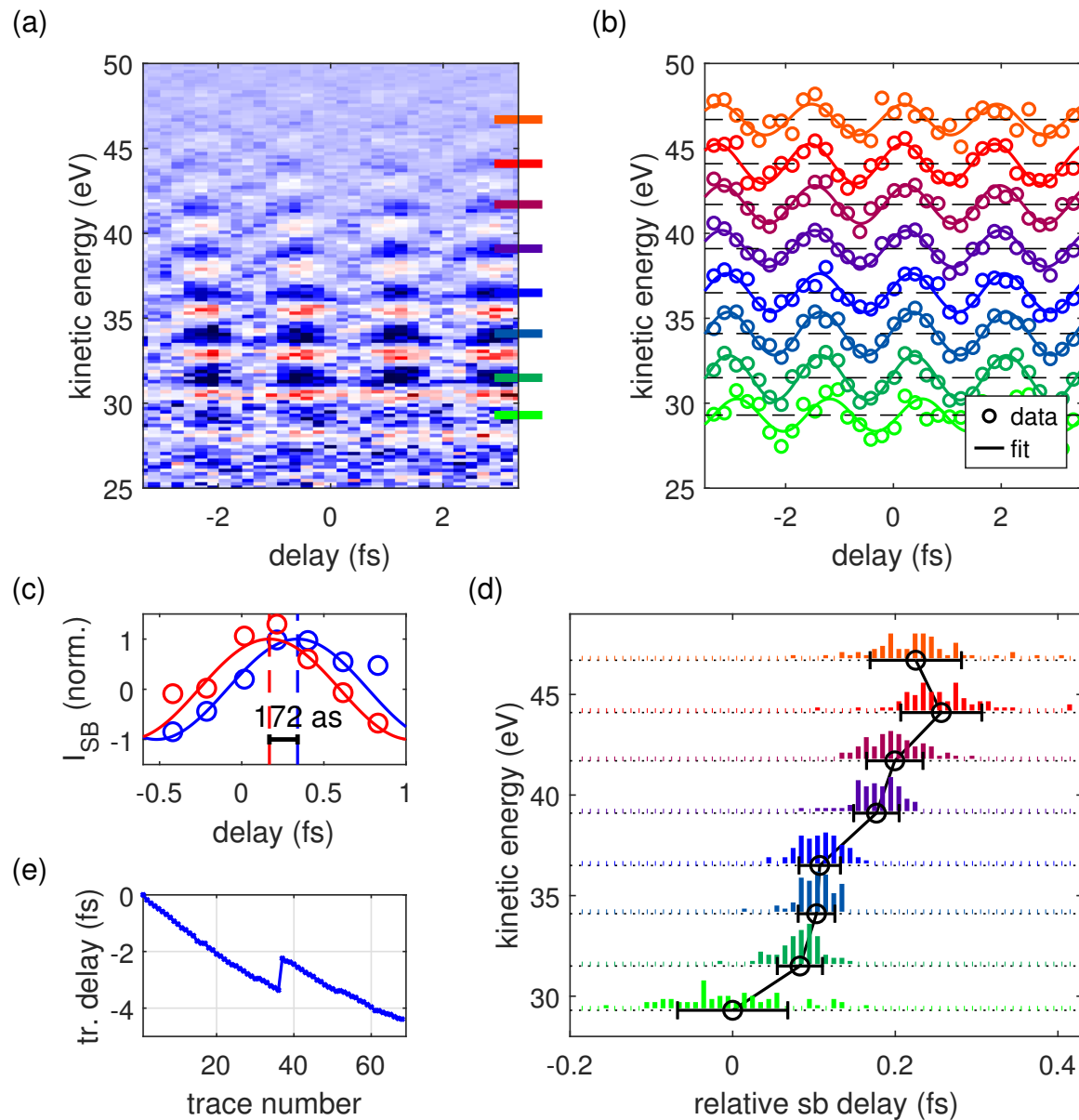


Figure 4.2: **a)** RABBITT trace measured within an acquisition time of 140 s. The spectrograms in Fig. 4.1 are obtained by summation over 68 such traces. Sideband positions are marked by colored lines on the right. **b)** Normalized sideband intensities extracted from a) with sine fits. **c)** Relative delay between two selected sidebands. **d)** Average relative sideband delays and standard deviations in the entire dataset (black circles and error bars). The histograms represent the distribution of the values extracted from the 68 individual traces. **e)** Drift in XUV-IR delay during the acquisition of the dataset extracted from the individual traces. After trace number 36 a measurement break of 50 minutes led to a sudden surge in the curve.

### 4.3 Sideband delays introduced by XUV optics

As shown in Section 2.4.4 the phase of each sideband (of the order  $m$ ) contains the difference of the spectral phases  $\Phi_{m\pm 1}$  of its two neighboring harmonics (see Eq. 2.35). By dividing it by the sideband oscillation frequency (i.e. twice the IR laser frequency  $\omega_{\text{IR}}$ ) this phase difference can be directly translated into an XUV induced sideband delay:

$$\tau_{\text{xuv},m} = \frac{\Phi_{m-1} - \Phi_{m+1}}{2\omega_{\text{IR}}} \quad (4.2)$$

Consequently, a linear attochirp will result in a linear shift of the sideband delays with respect to each other.

Four different components contribute to the total spectral phase of the XUV: i) The phase acquired in the HHG process itself, ii) dispersion in the gas in the HHG vacuum chamber, iii) dispersion in the aluminum filter and iv) the spectral phase of the XUV multilayer mirror.

The first two components can be neglected at our experimental parameters: An experimentally validated model was used to simulate HHG in argon in our cavity [161]. It yields a maximal HHG-induced sideband delay of less than 2 as over a wide range of parameters around our experimental conditions. This is neglectable compared to the size of the other contributions to the XUV spectral phase and the error bars of the experimentally determined sideband delays.

For the calculation of the dispersion in argon and in the aluminum filter, tabulated values for their refractive index were taken from Ref. [154]. Due to the low background pressure in the HHG chamber gas of 0.1 mbar or less, this delay contribution turned out to be below 1 as for both neon and argon and was neglected. The aluminum filter however, does introduce notable sideband delays on the order of tens of attoseconds over the relevant energy range.

By far the most important contribution is the influence of the XUV mirrors: Although their spectral phase is typically mostly linear within the FWHM of the reflectivity curve there can be a significant amount of chirp outside of this energy range (Fig. 4.3a). This can come down to a mirror induced sideband delay of more than hundred attoseconds between neighboring sidebands. The mirror-related delay is calculated from the phase design curves of the mirrors which have been shown to be highly reliable [162] and are fabricated inhouse.

The experiments in this thesis do not focus on the delays which are introduced by the XUV spectral phase, but on the delays from the actual photoemission process. Therefore, the sideband delays can be corrected for the spectral phase contributions as displayed in Fig. 4.3b. Especially for broadband measurements containing a large number of high harmonics, these corrections are important. However, if sideband delays from different initial states are compared the XUV spectral phase cancels out for sidebands of the same order because they are excited by the same high harmonics.

### 4.4 RABBITT Fourier analysis

Because the relevant information of a RABBIT trace is encoded in the sideband oscillations at twice the IR laser frequency  $\omega_{\text{IR}}$  it can be helpful to Fourier-transform a spectrogram and

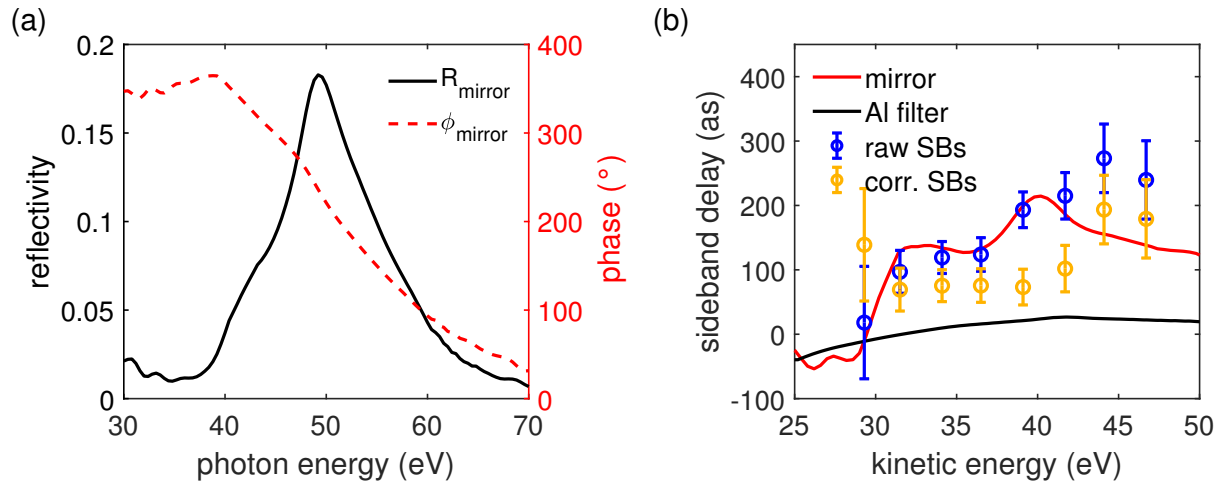


Figure 4.3: **a)** Design reflectivity and phase of the molybdenum-silicon XUV multilayer mirror used for measuring the spectrograms in Fig. 4.1. **b)** Sideband delays introduced by the 300-nm Al filter and the XUV mirror. To translate photon energy to kinetic energy, the energy axis was shifted by 6.5 eV to account for work function and binding energy of the most dominant part of the DOS. Mirror and filter delays are subtracted from the raw measured sideband delays (Fig. 4.2) to obtain the attochirp-corrected relative photoemission delays between the sidebands. Figure adapted from Ref. [163] under the terms of the [Creative Commons Attribution 4.0 International License](#).

convert the delay axis to frequencies (Fig. 4.4a and b). One useful application is to investigate if the probe intensity is such, that only two-photon transitions involving one XUV and one IR photon contribute notably to the spectrogram. This condition was assumed in the derivation of the RABBITT sideband formula (Section 2.4.4).

If the IR intensity exceeds  $\sim 10^{12}$  W/cm<sup>2</sup> four-photon transitions involving three IR photons occur, overlap with the two-photon sidebands and lead to sideband oscillations at  $4\omega_{\text{IR}}$  oscillations [104, 105]. Because this is not accounted for in the regular RABBITT sideband formula it can impair the measurement. Although such multi-IR photon transitions have been used in certain applications [104, 164, 165] they are therefore generally not desirable for RABBITT measurements.

An example of a trace with too high IR intensity is shown in Fig. 4.4a. The irregularities of the sideband oscillations can already be vaguely discerned in the raw spectrogram, as the width of the maxima and minima of the oscillations seem to be unequal and to deviate from a sinusoidal behavior.

By Fourier-transforming the trace along the delay axis the presence of the  $4\omega_{\text{IR}}$  components becomes very obvious (Fig. 4.4b). Summation over the energy axis of the absolute value of the Fourier-transform gives a clear overview over the dominating frequency components of the measurement as displayed in Fig. 4.4c. It shows the spectral components of the displayed RABBITT trace with too much IR intensity and another measurement which has been taken at

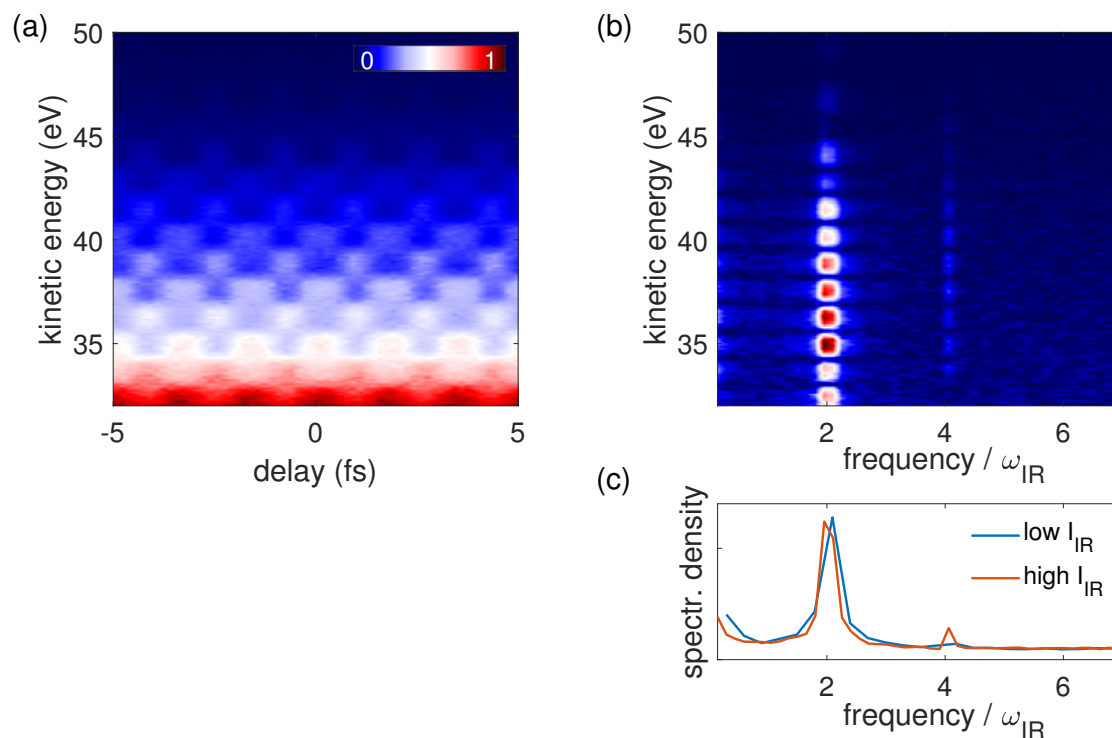


Figure 4.4: **a)** Raw RABBITT spectrogram data taken at high IR intensity. A non-sinusoidal behavior of the high harmonics and sidebands can be vaguely discerned as maxima and minima do not seem to be of equal length (in delay). **b)** Absolute value of the Fourier transform of the spectrogram in a). Sidebands and high harmonics show clear maxima in spectral density at twice the IR laser frequency, as expected from two-photon transitions. Another weaker set of peaks can be observed at  $4\omega_{\text{IR}}$  and indicates the presence of higher-order transitions. **c)** Summation over the energy axis of the data displayed in b) (high  $I_{\text{IR}}$ ). The curve peaks at  $2\omega_{\text{IR}}$  and  $4\omega_{\text{IR}}$ , whereas another measurement with less IR intensity (low  $I_{\text{IR}}$ ) does not exhibit a  $4\omega_{\text{IR}}$  peak.

lower IR intensity and does not exhibit a  $4\omega_{\text{IR}}$  peak.

The analysis of the Fourier transform of a RABBITT spectrogram can also be used to determine the delays of the individual sidebands from the  $2\omega_{\text{IR}}$  phase instead of fitting a sine to the sidebands. A more sophisticated example to apply this to spectrally overlapping RABBITT interferograms will be shown in Section 6.3.2.



# Chapter 5

## Initial-state induced photoemission delays in tungsten

It has been shown in experiments on gas atoms [10, 13, 166] and solids [103], that the angular momentum of an electronic state can have an influence on its photoemission delay. The MEGAS setup is perfectly suited for investigating this phenomenon with high flux and high temporal accuracy. Narrow and well-separated high harmonics offer the necessary energy resolution. It is fully preserved in space-charge free photoelectron detection enabled by MEGAS's high pulse repetition rate which will be shown in this chapter. Moreover, angle-resolved photoemission detection allowed to resolve and identify different initial bands in the photoemission spectra. By these means, final state effects on photoemission delays from W(110) were observed and will be reported in this chapter.

### 5.1 Space-charge free photoemission spectroscopy

In attosecond photoelectron spectroscopy experiments, the emission of all photoelectrons excited by an XUV pulse occurs quasi simultaneously within the pulse duration. Moreover, the laser beams are focused to spot sizes of several  $\mu\text{m}$ , to reach the necessary probe intensities for RABBITT or attosecond streaking.

Consequently, all photoelectrons generated by an XUV pulse (train) are confined to a micron-sized volume shortly after their emission, and interact with each other via the Coulomb force which is proportional to  $1/r^2$  with  $r$  being the distance between two charges. Hence, these space-charge effects due to Coulomb interaction can severely alter the kinetic energy and propagation direction of the photoelectrons. This manifests itself in spectral broadening and a shift towards higher kinetic energies on the high edge of the photoelectron spectrum as it is has been observed in many experiments [21–23].

To be able to resolve band-structure dependent features and closely neighbored states in photoelectron spectroscopy an energy resolution well below 1 eV is often necessary [78, 102] which is significantly impaired by space-charge broadening at kHz repetition rates and high

photoelectron flux. Theoretical and experimental studies have shown, that space-charge effects in time-resolved photoelectron experiments on solids can be calculated in a modified Long-Itchkawitz-Kabler model [23, 167]:

$$\Delta E_{\text{sc}}[\text{eV}] \approx 2 \cdot 10^{-6} \frac{N_e}{d_0[\text{mm}]} \quad (5.1)$$

This simple formula allows to calculate the space-charge induced spectral broadening  $\Delta E_{\text{sc}}$  (in electronvolt) from the number of emitted photoelectrons per pulse  $N_e$  and the diameter of the XUV beam on target  $d_0$  (in mm). Moreover, the space-charge induced kinetic energy shift is almost identical to the broadening and hence also described by this formula [23].

From the number of captured photoelectrons, the spectrometer acceptance angle and the pulse repetition rate, it can be deduced that in the MEGAS setup up to  $\sim 500$  photoelectrons are emitted per laser shot. For our XUV focus size of  $\sim 10 \mu\text{m}$  at  $60^\circ$  incidence angle on the sample and repetition rate of 18.4 MHz, this translates into a space-charge broadening of 50 meV according to Eq. 5.1. This value is well below the spectral width of the high harmonics of around 300 meV and hence hardly impairing our energy resolution.

Because the number of electrons per pulse  $N_e$  is the quotient of average photoelectron flux  $dN/dt$  and pulse repetition rate  $f_{\text{rep}}$ , the space-charge induced shift/broadening at equal focus size depends on these parameters:

$$\Delta E_{\text{sc}} \propto \frac{dN/dt}{f_{\text{rep}}} \quad (5.2)$$

According to this relation a kilohertz high harmonic source at otherwise equal experimental parameters would face significant space-charge broadening of far more than 1 eV. Alternatively, the photoelectron flux could be reduced to preserve the energy resolution but this would strongly impair the signal-to-noise ratio or result in much longer acquisition times. This is illustrated in Fig. 5.1a, which shows how space-charge effects would change the measured photoelectron spectrum at lower pulse repetition rate but equal average electron flux and focus size.

To investigate the space-charge effects in our setup, we performed measurements with different photoelectron flux and compared the resulting photoelectron spectra. The electron flux was reduced by clipping the XUV beam with an aperture which was introduced into the beam. Even though no space-charge effects can be discerned by bare eye in Fig. 5.1b a close look reveals the onset of a space-charge induced energy shift. After a Shirley-type background subtraction [168] a set of Lorentzians was fitted to the photoelectron peak data to determine their exact position (Fig. 5.1c). A relative shift in photoelectron kinetic energy as function of the number of emitted photoelectrons could be extracted. The observed shift agrees well with the space-charge induced shift predicted by Eq. 5.1 (Fig. 5.1d).

Because the photoelectron peak width is already on the order of 1 eV, the expected additional space-charge induced spectral broadening of 50 meV could not be observed. Since a slight shift in kinetic energy does not impair our experiments the PES measurements can hence be considered free from any harmful space-charge induced distortions.

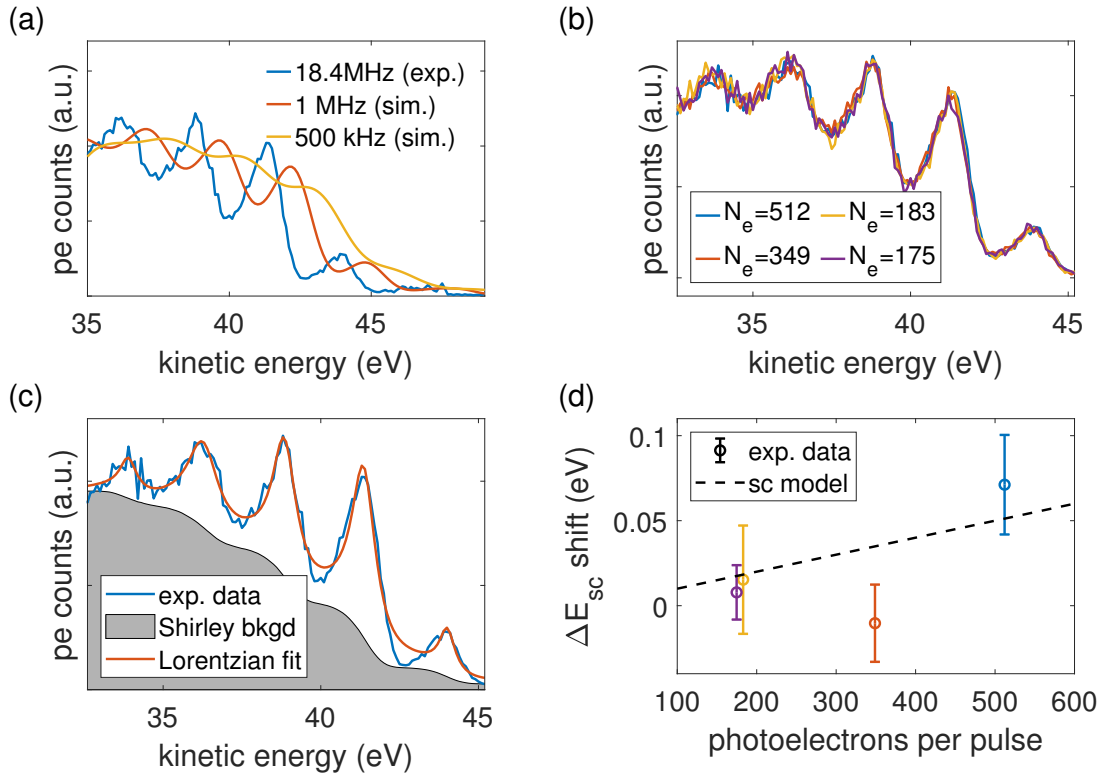


Figure 5.1: **a)** Measured photoelectron spectrum (at 18.4 MHz) together with simulations of the same spectrum at the same average photoelectron flux with space-charge induced spectral broadening and shift at 1 MHz and 500 kHz. **b)** Photoelectron spectra measured with different number of photoelectrons per shot. **c)** Photoelectron spectrum with calculated Shirley background and fit of 5 Lorentzian curves. **d)** Shift in photoelectron kinetic energy as function of the number of photoelectrons per pulse (identical colors as in b)). The given value is the mean over the relative shift of all 5 fitted peaks in each photoelectron spectrum, the error bars their standard deviation. Since the absolute value of the kinetic energy shift is unknown, a constant offset was chosen to match the theoretical space-charge shift calculation according to the modified Long-Itchkawitz-Kabler model.

Considering the problems arising from higher repetition rates such as detrimental cumulative effects in the HHG gas target [169] and time-of-flight dispersion management for the detection of the photoelectrons (Section 3.4.4), 18.4 MHz seems to be in the optimum repetition-rate range for space-charge-free photoelectron spectroscopy.

## 5.2 Tungsten electronic band structure

A single atom features electron orbitals with discrete binding energies. In solids, these orbitals overlap with those from the neighboring atoms and give rise to continuous energy bands

instead of sharp and discrete energy levels. This phenomenon affects particularly weakly bound electronic states slightly below the Fermi energy which form the so-called valence band as well as the mostly unpopulated states above.<sup>1</sup> The resulting bands and their dispersion relation  $E(k)$  between energy and crystal momentum  $k$  determine the optical, thermal and electronic properties of a solid.

Because the momentum parallel to the surface is preserved in the photoemission process (Section 2.4.1), the electronic band structure directly determines the final energy and emission angles of photoelectrons. Moreover, the band structure is directly related to the density of states (DOS) in a solid and the group velocity  $v_{\text{gr}}$  at which an electron wave packet travels within the solid. This section is dedicated to the band-structure related calculations which were done in the context of this thesis to understand and interpret the results of the conducted valence-band photoemission experiments.

All band structure calculations in this work were performed with the open-source software Quantum ESPRESSO, which relies on density function theory, plane waves and pseudopotentials [170]. The calculations were done for a body-centered cubic (bcc) crystal of tungsten atoms with a lattice constant of  $a_w = 3.165 \text{ \AA}$  [171] and a Perdew-Burke-Ernzerhof functional type ultrasoft pseudo potential. For consistency it was confirmed that the calculated band structure and density of states were in good agreement with literature [172].

### 5.2.1 Brillouin zone and photoelectron detection geometry

The first Brillouin zone (BZ) of a bcc crystal is a rhombic dodecahedron and the critical points  $\Gamma$ , N, P and H form the corners of the irreducible BZ (see Fig 5.2a). The bands in the remaining entire BZ can be deduced from the irreducible BZ by the crystal symmetries. As the component of the crystal momentum of an electron parallel to the surface  $k_{\parallel}$  is conserved in the photoemission process, only electrons from a certain part of the BZ are captured by a detector at a fixed angle acceptance  $\alpha$ :

$$k_{\parallel, \text{max}} = \hbar \sin(\alpha) \cdot \sqrt{2m_e E_{\text{kin}}} \quad (5.3)$$

The observation direction for all photoelectron spectra measured in this work was perpendicular to the tungsten (110) surface, which corresponds to the  $\Gamma$ -N direction in the reciprocal space. Hence, at a fixed kinetic energy  $E_{\text{kin}}$  the observable part of the BZ forms a cylinder around the  $\Gamma$ -N-axis as displayed in Fig. 5.2a. In the simplest case, the angle acceptance of an electron spectrometer can be directly deduced from the distance of sample and detector and the detector diameter (Fig. 5.2b). However, this angle can be significantly enlarged by using additional electron optics. All time-resolved measurements displayed in this work were done in the spectrometer's LAD mode with  $7^\circ$  acceptance angle (Section 3.4.4).

---

<sup>1</sup>For deeply bound electronic states in solids, this effect is significantly less pronounced due to less overlap of these more confined electronic orbitals.

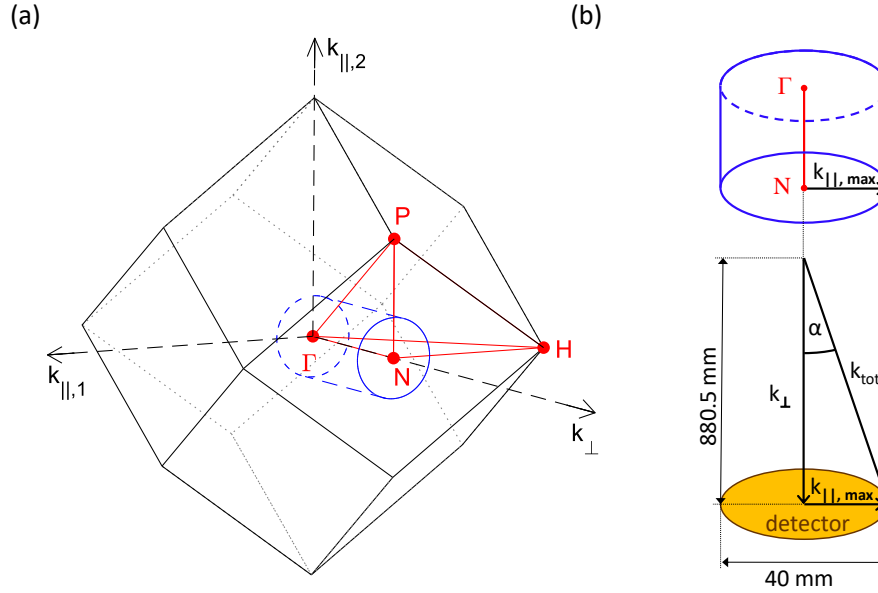


Figure 5.2: **a)** Tungsten bcc Brillouin zone. For a (110) orientation the crystal momentum component normal to the surface  $k_{\perp}$  is the  $\Gamma$ - $N$  direction. For detection within a fixed acceptance angle around the surface normal the detectable part of the BZ is a cylinder around  $\Gamma$ - $N$  in the reciprocal space (blue lines). Here, the radius of the depicted cylinder is  $0.18 \frac{2\pi}{a_{\text{W}}}$  which corresponds to typical parameters in this work (i.e. detector acceptance angle of  $\pm 7^\circ$  at 32 eV kinetic energy). **b)** Detection geometry: If no electron optics are applied, the size and distance of the detector from the sample determines the angle acceptance  $\alpha$  of an electron ToF spectrometer (40 and 880.5 mm respectively in our case). At a given electron momentum  $k_{\text{tot}}$  this directly translates into a maximum detectable momentum parallel to the surface  $k_{\parallel, \text{max}}$ .

### 5.2.2 Density of states

The density of states  $D(E)$  is a measure for the number of electronic states within an energy interval  $dE$  of an electronic band structure and can be calculated from the dispersion relation of the individual bands  $E_n(k)$  as follows [173, p. 486]:

$$D(E) = \frac{1}{4\pi^3} \sum_n \int \frac{dS_n}{|\nabla_{\mathbf{k}} E_n(k)|} \quad (5.4)$$

Here,  $dS_n$  denotes a surface element of the equal-energy surface of  $E_n(k)$ . Because the band structure used in this thesis was calculated and thus already discretized in  $k$ , the density of states was obtained by counting the number of data points in a certain energy interval  $E_n(k_i) \in [E; E + dE[$ .

The calculated tungsten valence band structure and the resulting density of states are displayed in Fig 5.3a and b respectively. Whereas the lower energy part of the band structure

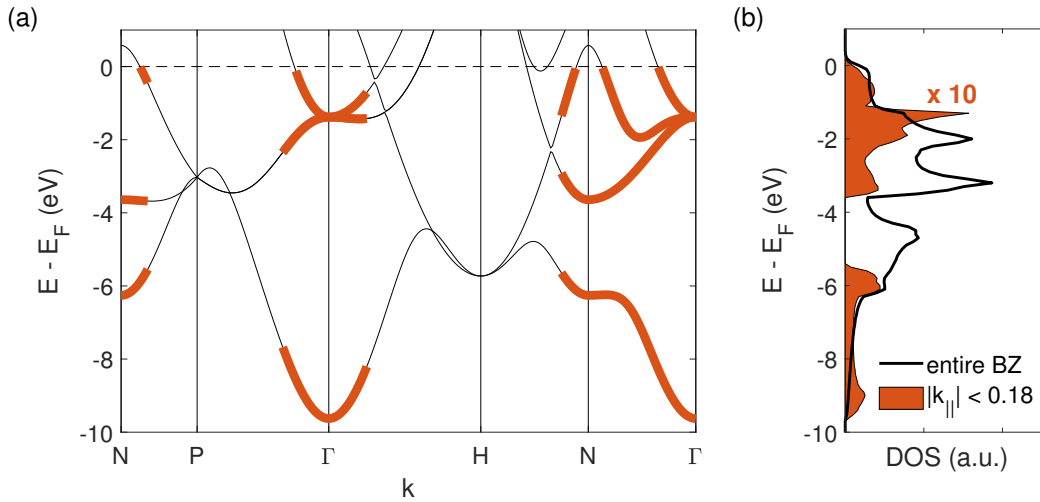


Figure 5.3: **a)** Band structure of a bcc tungsten crystal. Occupied bands with  $k_{\parallel} < 0.18 \frac{2\pi}{a_w}$  around  $\Gamma$ -N are highlighted in red. This corresponds to an acceptance angle of  $7^\circ$  at 32 eV kinetic energy. The low energy bands exhibit a parabola-shaped dispersion which is characteristic for  $sp$  bands. The bands right below the Fermi-energy are dominated by shallower  $d$  bands. **b)** Occupied tungsten density of states for the entire Brillouin zone (black line) and for the part of the BZ with  $k_{\parallel} < 0.18 \frac{2\pi}{a_w}$  around  $\Gamma$ -N (red filled area) as highlighted in a).

consists of  $sp$  bands recognizable by their characteristic upwards parabola shape, the bands right below the Fermi edge can mainly be attributed to shallower  $d$  bands. Accounting for a limited acceptance angle only photoelectrons from the band parts around the observation direction  $\Gamma$ -N are captured. For our setup with an acceptance angle of  $\pm 7^\circ$  (as in the spectrometer's LAD mode) at a typical kinetic energy of 32 eV the visible band parts are marked in Fig 5.3a. This translates into a partial density of (occupied) states over the detectable reciprocal space as displayed in Fig. 5.3b. For these parameters, the DOS of the valence band is split into two parts separated by a gap of 2 eV, where the lower energy part consists of  $sp$ -band electrons and the higher energy part is dominated by  $d$ -band electrons.

As seen in Section 2.4.1 the kinetic energy of a photoelectron is the XUV photon energy less the work function and binding energy. In the case of a continuous distribution of states in a solid spanning over several eV, the static photoelectron spectrum is consequently the convolution of the excitation spectrum and the occupied DOS. In this simple picture a constant transition probability over the relevant energy range is assumed and scattered secondary electrons are not considered.

Hence, the knowledge of the DOS is crucial for the correct interpretation of photoelectron spectra. This is particularly true for a non-trivial excitation spectrum formed by a set of high harmonics as illustrated by Fig. 5.4. Because only occupied states contribute to the photoelectron spectrum, the DOS has to be multiplied by the Fermi-Dirac-distribution at the correct temperature (in our experiment typically around 900 K). By coincidence, the separation

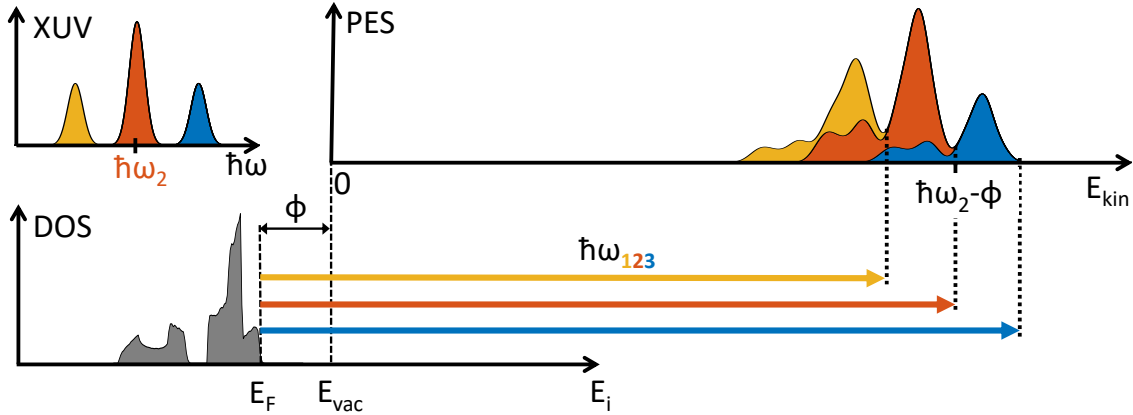


Figure 5.4: Electrons from the occupied part of the density of states below the Fermi energy  $E_F$  are emitted after absorption of a photon with energy  $\hbar\omega$ . The resulting photoelectron spectrum emitted from a solid is a convolution of the density of states and the XUV spectrum shifted by the work function  $\Phi$ .

of the main peaks of the resulting partial DOS corresponds almost precisely to multiples of the spacing between the high harmonics, which additionally complicates disentangling the influences of excitation spectrum and initial state distribution.

## 5.3 Intra-valence band referenced RABBITT

This section is dedicated to photoelectron spectroscopy experiments on the tungsten valence band whose deepest bound states have binding energies of about 15 eV below the vacuum level. Therefore, the high harmonics for the experiments presented in this section were generated in argon, which provides sufficient photon energies and allows for high photon flux. The number of the detected photoelectrons with kinetic energies of more than 23 eV and in an angle range of  $\pm 7^\circ$  was in practice limited by our delay-line detector which allows for the detection of a maximum of about  $1.1 \times 10^6$  photoelectrons per second.

### 5.3.1 XUV spectra for valence band photoemission spectroscopy

To investigate contributions from different band types within the tungsten valence bands it is most insightful to use as monochromatic excitation as possible to be able to unambiguously attribute a photoelectron to a specific initial state. For static photoelectron spectroscopy measurements with an HHG source, it would therefore be ideal to have only one high harmonic. Due to the high absorption of the XUV in the multilayer mirror materials only a few layers contribute to its reflectivity characteristics and do not allow for designs with full suppression of all but one high harmonic for photon energies of 30 to 50 eV.

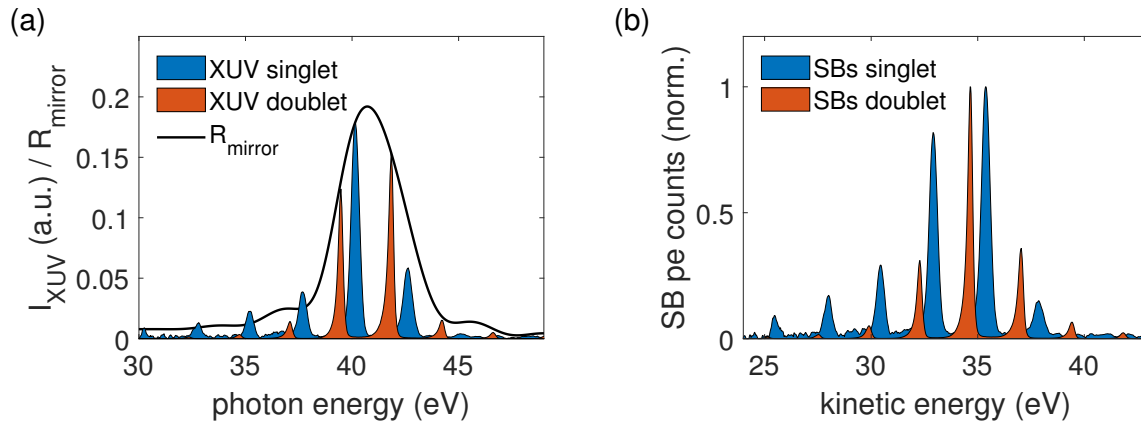


Figure 5.5: **a)** XUV spectra for two different amounts of intra-cavity blueshift. Depending on the energies of the harmonics the resulting spectrum after the XUV mirror features either one or two dominating harmonics (singlet or doublet). **b)** Intensities of the modulated RABBITT sideband signal calculated from the XUV spectra in a) (in the same colors) for an initial state with zero linewidth and 6 eV binding energy. The XUV spectrum with one strong harmonic results in several sidebands of similar intensity, the doublet XUV spectrum in a set of sidebands, which is strongly dominated by a single intense central sideband.

However, with a mirror of relatively small bandwidth it is possible to come at least close to this ideal situation. It is best achieved if the maximum of the reflectivity curve coincides with the energy of a high harmonic. In this configuration, the neighboring high harmonics are strongly suppressed, because they are separated by around 2.4 eV from the reflectivity maximum (at 1030 nm). By choosing the central energy of the mirror such that it coincides with one of the most intense harmonics, the monochromaticity of the resulting excitation spectrum is further improved.

On the other hand, in order to determine the photoemission delays by means of RABBITT, it is necessary to have at least two strong harmonics to generate an oscillating sideband by interference of two-photon transition photoelectrons. Consequently, the mirror bandwidth must be large enough to cover two high harmonics at reasonable reflectivity.

To be able to combine both these possibilities of filtering either one or two high harmonics with a single mirror we opted for a silicon and boron carbide XUV multilayer system. The mirror reflectivity curve is centered at 41 eV photon energy with a FWHM of 4 eV and a peak reflectivity of 19% (Fig. 5.5a). With this mirror both these types of excitation spectra can be obtained by shifting the position of the high harmonics under the mirror reflectivity curve. This can be achieved by tuning the driving laser wavelength. As the photon energies of the high harmonics are multiples of the fundamental laser photon energy, small shifts in IR photon energy can add up to significant shifts in the position of higher harmonics.

Such a change in laser wavelength can be realized in single-pass HHG systems, for example by trimming the laser spectrum. Nonlinear enhancement cavities offer another approach: If

supported by the cavity mirror bandwidth, newly generated frequency components can build up in the cavity and even lead to significant spectral broadening and self-compression in temporal dissipative solitons as recently demonstrated [174].

In the case of intracavity HHG the nonlinear element is the HHG gas target, which is increasingly ionized during the passage of the IR laser pulse thus introducing a blueshift by means of self-phase modulation at each roundtrip. Therefore, the intracavity spectrum typically is blue-shifted with respect to the input spectrum. The amount of blueshift can be controlled by the position and pressure of the HHG target [69].

As displayed in Fig. 5.5a the position of the high harmonics could be shifted by this means by 0.7 eV, corresponding to a difference of 17 nm of the central IR wavelength. As a result, XUV spectra with either one or two dominating high harmonics can be created. They will be referred to as singlet and doublet spectrum in the following.

The displayed singlet spectrum was measured directly after the XUV double mirror. The doublet spectrum was calculated from the mirror reflectivity curve and the XUV spectrum measured before the XUV mirror because the XUV spectrometer was set up at a different position in the setup during that measurement (Section 3.3).

Apart from the IR probe intensity, the intensity of the characteristic RABBITT sideband modulation depends on the product of the field amplitudes of the neighboring harmonics [99]. Consequently and quite intuitively, a single intense harmonic cannot generate a strongly modulated sideband as long as the neighboring harmonic is weak. Therefore, the single-harmonic spectrum features several sidebands of comparable intensities whereas the doublet spectrum is vastly dominated by a central sideband (Fig. 5.5b).

Hence, the possibility to change between these two different XUV spectra allows to choose the excitation spectrum according to the desired application with a single multilayer mirror: For static photoelectron spectroscopy it is most insightful to opt for the singlet spectrum to mitigate superposition of photoemission from different high harmonics and initial states. For time-resolved attosecond PES measurements on of closely neighbored initial states it is best to have a doublet of two equally intense harmonics resulting in a single strong RABBITT sideband.

Consequently, these two types of excitation spectra have been employed throughout this chapter according to the specific application. It will also be demonstrated how crucial the suitable excitation spectrum for time-resolved measurements on closely neighbored states is (Section 5.3.4).

### 5.3.2 Distinguishing photoemission from tungsten *sp* and *d* bands

The valence band of tungsten spans an energy range of about 10 eV below the Fermi energy and consequently it is difficult to attribute photoelectrons unambiguously to a specific initial state and a specific high harmonic. However, due to the limited detection angle, the density of the detectable states features a certain band gap, which separates the DOS in a *d*-band dominated part just below the Fermi energy and a *sp*-band part at lower energies (Fig. 5.6a). Utilizing the singlet XUV spectrum (Fig. 5.5a) it is thus possible to roughly separate the *d*-band and *sp*-band

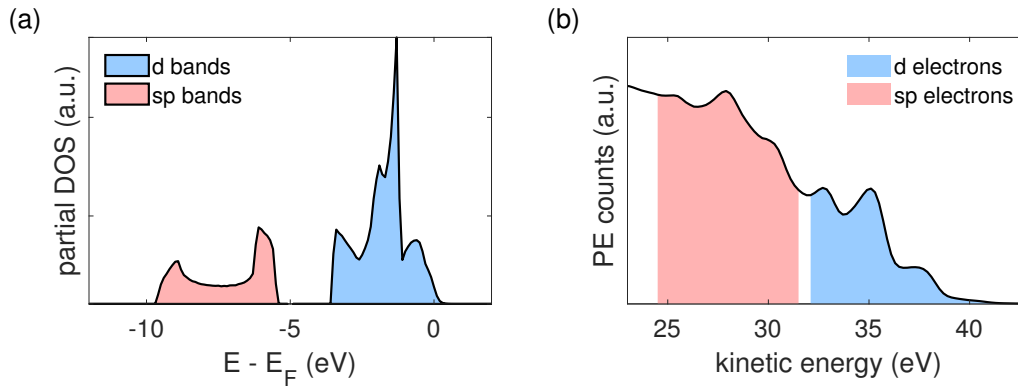


Figure 5.6: **a)** Partial density of states in tungsten as defined by the visible parts of the Brillouin zone at our spectrometer acceptance angle of  $\pm 7^\circ$  around 32 eV kinetic energy. The lower-energy part consists of *sp* bands, the higher-energy part is *d*-band dominated. **b)** Static photoelectron spectrum excited by a singlet XUV spectrum. Energy ranges with predominantly *sp*- and *d*-band photoelectrons are indicated in the same colors as in a).

electrons energetically in the photoemission spectrum as displayed in Fig. 5.6b.

The *sp*- and *d*-band contributions can also be distinguished in angle-resolved PES measurements due to their characteristic dispersion relation: *sp* bands form upwards open parabolae contrary to the more shallow or downward open *d*-bands. Fig. 5.7a displays an ARPES dataset along the crystal N-P direction. By selecting this azimuthal orientation of the crystal, the visible part of the Brillouin zone is a part of the plane formed by  $\Gamma$ -N-P (Fig. 5.2a). Consequently, the bands along the N-P and  $\Gamma$ -P direction contribute to the photoemission and can also be recognized in the photoelectron data. The data was measured in the wide-angle mode of the spectrometer, which captures electrons in an emission angle range of  $\pm 15^\circ$ .

To reduce the secondary electron background and increase the visibility of the bands in the measured data, a smoothed version of the photoelectron spectrum in each angle bin was subtracted from the data. From the conducted density of state calculations (Section 5.2.2) and the measured singlet XUV spectrum it is possible to simulate this measurement. Because the simulation does not include any secondary electrons, it looks qualitatively a little different, but the result displayed in Fig. 5.7b still reproduces well the key features observed in the experimental data. This clearly shows that the initial bands can be separated and identified in the photoelectron spectra.

### 5.3.3 Initial state photoemission delays

To investigate the photoemission timing of *sp* and *d* bands within the tungsten valence band, the XUV doublet spectrum with two strong harmonics and one dominating sideband (Fig. 5.5a) is chosen to prevent overlap from sidebands from different initial bands and different high harmonics. The contribution from the *sp* and *d* bands can already be distinguished in the static photoelectron spectrum in Fig. 5.8a.

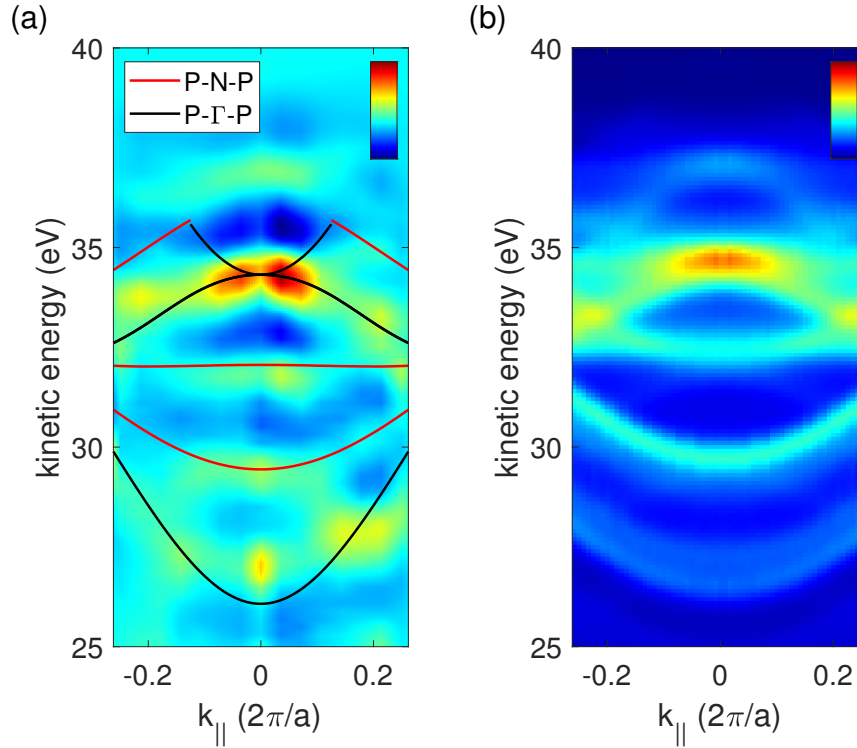


Figure 5.7: **a)** Angle-resolved photoemission spectroscopy data along the N-P direction measured in the wide-angle mode of our spectrometer with an angle acceptance of  $\pm 15^\circ$ . Contributing occupied bands in the  $\Gamma$ -P and N-P orientation are indicated by black and red lines respectively (see also Fig. 5.2a). This measurement was taken with an XUV spectrum which was dominated by one strong central harmonic. **b)** Simulated angle-resolved photoemission spectrogram for the same detection geometry and measured XUV spectrum as in a). Figure adapted from Ref. [163].

The positions of the sidebands are marked by dashed lines as they were extracted from the RABBITT spectrogram in Fig. 5.8b. Their spacing of 6.4 eV already indicates that they originate from different initial states and not from different high harmonics. The latter would result in an energy difference of even multiples of the IR photon energy of  $\hbar\omega = 1.2$  eV, such as 4.8 or 7.2 eV. The *sp*-photoelectron peaks are relatively weak due to the lower density of states and they are located in an energy range which is dominated by a strong background of secondary electrons.

The RABBITT trace in Fig. 5.8b clearly exhibits two strong oscillating sidebands which are well separated from each other and whose neighboring harmonic peaks are also modulated due to depletion. Sideband delay evaluation in the dataset yields a delay of  $39 \pm 18$  as of the *d*-band photoemission compared to the *sp*-photoelectron sidebands as it is illustrated in a representative sideband fit in Fig. 5.8c and shown in more detail in the corresponding inset. Again, the given error is the standard deviation over the delays extracted from all individual RABBITT traces within the dataset.

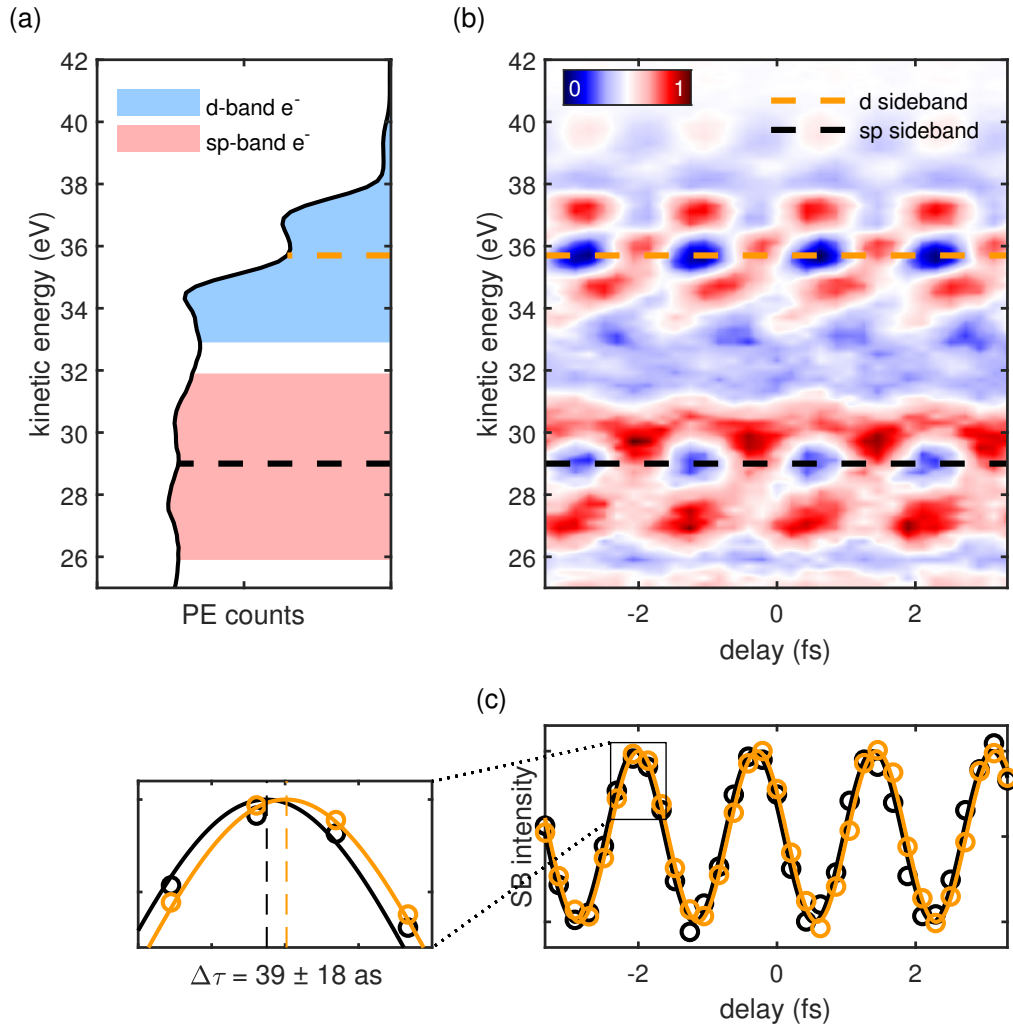


Figure 5.8: **a)** Static photoelectron spectrum measured with an XUV spectrum with two dominating high harmonics. Sideband positions are marked by dashed lines and energy ranges with predominantly *sp*- and *d*-band photoelectrons are indicated. **b)** RABBITT spectrogram featuring two strong sidebands. They can be attributed to *sp*- and *d*-band photoelectrons respectively and are separated by 6.4 eV. The entire dataset consists of 33 delay steps of 208 as and was measured within a total net acquisition time of 28 minutes. **c)** Sideband data and sine fits. The *d*-electron sideband is delayed by  $39 \pm 18$  as with respect to the *s*-electron sideband. Figure adapted from Ref. [163].

Previous attosecond experiments on gas samples have reported an increase in photoemission delay for electronic states with higher angular momentum on the order of a few tens of attoseconds [10, 13, 166].

Although it seems more intuitive that the repulsive centrifugal force of a higher angular momentum would lead to a higher photoemission delay the mathematical treatment of the

scattering of the electron wave packet in the resulting potential during the photoemission process predicts longer emission times for higher orbital momentum [175] as it was confirmed by the experiments.

The fact, that this phenomenon also applies to solids is not trivial because of the influence of the surrounding electrons and the crystal lattice. Recently, it has also been observed for the first time in photoemission from a solid between the valence band and deeper bound states of a tungsten diselenide crystal [103]. This work constitutes the first such measurement with RABBITT on a solid material which finds photoemission delays between different band types within the valence band. It paves the way to further investigations of how an emitted photoelectron interacts with its environment and possibly how the system dynamically reacts to the photoemission process. The combination of high resolution in energy and time which is offered by the RABBITT-technique is highly beneficial for this kind of measurements and will enable more valuable insights in valence band electron dynamics, especially when combined with the high flux generated by our XUV source and the angular resolution of our electron spectrometer.

### 5.3.4 Excitation-dependent RABBITT spectrograms

The choice of the excitation spectrum for the measurement of intra-valence band photoemission delays has already been discussed in Section 5.3.1. To underscore the importance and influence of the suitable XUV spectrum for the desired application, RABBITT measurements with the single-harmonic spectrum are displayed in Fig. 5.9a. For comparison the doublet XUV spectrogram is shown in Fig. 5.9b and the respective excitation spectra as insets.

Although both have been measured with the same XUV mirror and the same sample the differences between the two RABBITT traces are striking. Only the fundamental laser wavelength was changed by about 17 nm by intra-cavity blueshift. The singlet XUV spectrum leads to several sidebands of comparable intensity as calculated and displayed in Fig 5.5b and experimentally confirmed in the RABBITT measurement.

The sideband delays extracted from the two spectrograms are shown in Fig 5.5c and are as different as the corresponding spectrograms themselves. Whereas the doublet-harmonic spectrogram exhibits a relatively small relative delay of 39 as between its two sidebands, the delays from the singlet-spectrum spectrogram feature significantly larger delays of up to more than 300 as. This value is far beyond any initial-state orbital momentum induced photoemission delay reported so far [10, 13, 103, 166]. Instead, these delays can be attributed to the spectral phase of the XUV mirror and are in almost perfect agreement with the calculated mirror sideband delay.

Consequently, the sidebands originate predominantly from the same initial state ( $d$ -band) but different high harmonics. This is corroborated by the spacing between the observed sidebands which is constantly about 2.4 eV over the entire energy range and does not add up to the energy difference of 6.4 eV which separates the  $sp$ - and  $d$ -band sideband in the doublet-harmonic spectrogram.

Although photoelectrons originating from  $sb$  bands are also present in the singlet-XUV

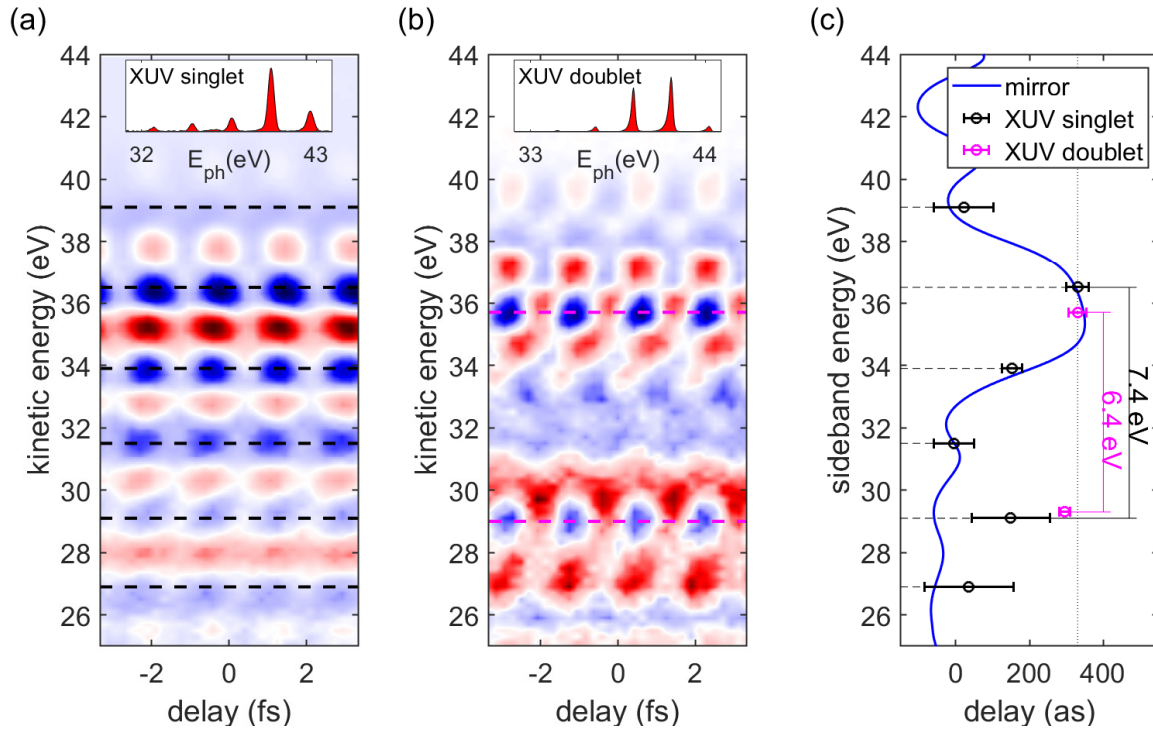


Figure 5.9: **a)** RABBITT spectrogram measured with the XUV 'singlet spectrum' shown in the inset. Six sidebands can be well discerned and are indicated by the black dashed lines. The dataset was measured within a total net acquisition time of 136 minutes. **b)** RABBITT spectrogram measured with the XUV 'doublet spectrum' shown in the inset. Only two sidebands can be well discerned and stem from different initial bands. Their position is indicated by the black dashed lines. Dataset measured within 28 min. **c)** Sideband delays extracted from the spectrograms in a) and b) marked in the same colors. The delays from the XUV-singlet spectrogram agree well with the mirror induced sideband delay curve. Figure adapted from Ref. [163].

spectrogram, they are covered by the more intense *d* band electron sidebands from lower harmonics. However, the sideband at 29 eV does show a deviation of around 200 as from the mirror delay curve. This could also be observed to a smaller extent for the next lower sideband at 27 eV. This behavior can be explained by the contribution of photoemission from higher order harmonics and the deeper bound *sp* electrons.

In conclusion, the suitable excitation spectrum is crucial for the measurement of intravalence band photoemission delays in tungsten. Otherwise, the relatively weak *sp*-band contribution is covered by the dominant *d*-band photoelectrons from weaker high harmonics. It also shows clearly, that the width and structure of the valence band does play an important role in the evaluation of photoemission delays in attosecond experiments, which is often neglected in attosecond PES experiments. This applies particularly to experiments utilizing XUV multilayer mirrors, which can introduce significant attochirp that can easily be confused with actual photoemission delay.

# Chapter 6

## Final-state induced photoemission delays in tungsten

Albeit an XUV photon excites a photoelectron from a solid above the vacuum energy, the electron can still be subject to the periodic crystal potential and its band structure. If an electron wave packet propagates in a highly excited final state of a solid material to its surface, this can be governed by its band-structure dependent group velocity in the three-step model of photoemission. This can lead to a significant increase in photoemission delay [9, 78, 102]. In the one-step photoemission picture, this can also be explained by a resonant transition to a bulk final state which experiences less damping within the solid compared to a free-electron final state [176]. This results in higher emission depth and delay.

The high energy resolution as well as the high photon energies and high flux make the MEGAS source perfectly suited for the investigation of such final-state induced photoemission delays as it will be shown in this chapter.

### 6.1 Final band group velocities in tungsten

Photons in the extreme ultraviolet penetrate around 100 Å into tungsten [154], but the mean emission depth of a photoelectron in the corresponding kinetic energy range is only several Å due to the comparably small electron mean inelastic free path in a solid [177]. The group velocity of the final band in the photoemission process can determine the time that a photoelectron generated in a bulk material needs to cover this distance [102]. At kinetic energies of 20 to 100 eV the corresponding typical group velocities are in the  $10^6$  m/s range which can lead to transport times of several hundred attoseconds. Therefore, this transport time is for solids usually the dominant contribution to the total photoemission delay measured in a PES-experiment [12, 14, 102].

The group velocity at which electron wave packets travel in a specific band  $n$  within the periodic potential of a crystal is determined by its dispersion [173, p. 495]:

$$\mathbf{v}_{\text{gr},n} = \frac{1}{\hbar} \nabla_{\mathbf{k}} E_n(\mathbf{k}) \quad (6.1)$$

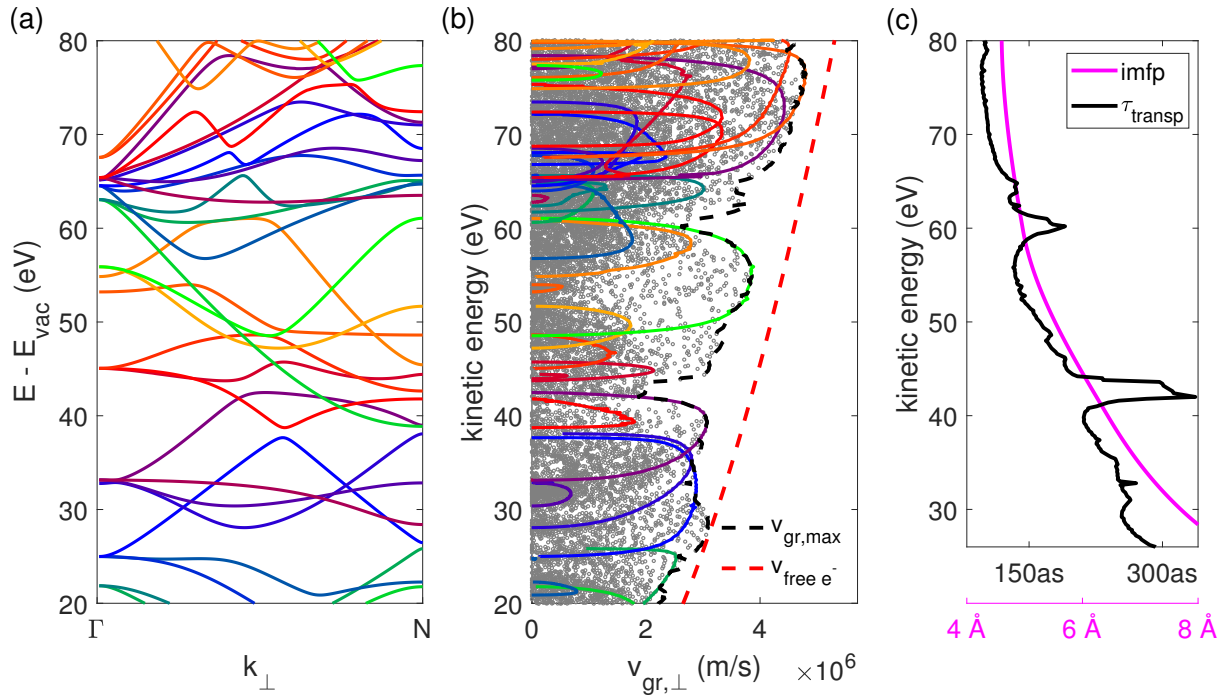


Figure 6.1: **a)** Calculated band structure of the unoccupied conduction band in the  $\Gamma$ -N direction. **b)** Group velocity component perpendicular to the W(110) surface derived from the band structure in a) (solid lines) and at 10,695 points in a  $k_{\parallel}$  radius of  $0.25 \frac{2\pi}{a_w}$  around the  $\Gamma$ -N direction (gray dots) (corresponding to  $7^\circ$  emission angle at 62 eV kinetic energy). The maximal group velocity  $v_{\text{gr,max}}$  over the entire considered part of the reciprocal space is marked by a black dashed line, the free-electron dispersion by a red dashed line. The entire dataset consists of 10,695  $k$ -space points in lines of 155  $k_{\perp}$  values at 69 different  $k_{\parallel}$ -points distributed equally over the covered part of the BZ. For better illustration, a representative sample of around 10% of the datapoints are displayed in this plot. **c)** Electron inelastic mean free path (IMFP) in tungsten (magenta line) taken from Ref. [177]. From  $v_{\text{gr,max}}$  in b) and the IMFP a maximum electron transport time  $\tau_{\text{transp}}$  was calculated (black line).

For the photoemission timing only the component perpendicular to the crystal surface  $v_{\text{gr},\perp}$  is relevant. In the case of a W(110) crystal this is the  $\Gamma$ -N direction. Figure 6.1a displays the calculated band structure along this direction. According to Eq. 6.1 the perpendicular group velocity is simply the derivative of these bands, as shown in Fig. 6.1b in identical colors. Only photoelectrons which travel towards the surface will be emitted and detected. Therefore, negative velocities do not play a role and are not displayed.

As already discussed for the density of states (Section 5.2.1) the contributions from the entire detected part of the Brillouin zone in the given measurement geometry must be considered. This was implemented by calculating  $v_{\text{gr},\perp}$  at a total of 10,695 points in this cylindrical part of the reciprocal space (see Fig. 6.1b).

All points in the dataset contribute to the overall observed group velocity of all photoelectrons within the spectrometer acceptance angle. Because electrons at these crystal momentum values can have different transition probabilities and be scattered differently on their way, it is challenging to make quantitative predications of the overall group velocity.

However, it is possible to determine the maximum perpendicular group velocity  $v_{\perp, \max}$  of the contributing bands at each final energy. This upper limit is also shown in Fig. 6.1b together with the energy-velocity dispersion of a free electron. The general behavior of the maximum group velocity curve is following the parabola of the free electron dispersion, although slightly shifted to lower velocities. However, two very prominent dips in  $v_{\perp, \max}$  arise at 43 and 60 eV final kinetic energy. They are caused by very shallow bands at these energies (Fig. 6.1a).

From the electron inelastic mean free path (IMFP) in tungsten and  $v_{\perp, \max}$  a maximum photoelectron transport time  $\tau_{\text{transp}} = \text{IMFP}/v_{\perp, \max}$  can be derived (Fig. 6.1c). The transport time follows roughly the energy dependence of the inelastic mean free path, except for the peaks at 43 and 60 eV final kinetic energy, which stem from the minima in  $v_{\perp, \max}$ . This characteristic behavior could also be observed in the RABBITT experiments conducted within the scope of this thesis and will be presented in Section 6.3.1.

## 6.2 Tungsten core state RABBITT

As described in Section 2.4 only relative photoemission delays between different initial states or samples can be measured directly by means of RABBITT or attosecond streaking.

In attosecond streaking measurements it is therefore a standard approach to reference the timing of valence band photoemission from solids to deeply bound core states [8, 14, 103, 178]. This requires high photon energies to overcome the core-state binding energies of typically at least several tens of electronvolts [179].

In RABBITT experiments on solids this has so far not been demonstrated. With conventional single-pass HHG systems it is highly challenging to generate attosecond pulse trains with sufficiently high photon flux and the necessary photon energies at decent space-charge conditions. Therefore, the work presented in this chapter represents the first core-state referenced RABBITT measurement on a solid.

The core states in tungsten with the lowest binding energy are the  $4f$  states. They are split into a doublet of 31.2 and 33.4 eV binding energy due to spin-orbit coupling [179, 180]. Hence, including the work function of 5.3 eV for a W(110) surface [181] a total photon energy of at least 36.5 eV is necessary to excite  $4f$  electrons in tungsten above the vacuum level. Although the photon energies generated by the MEGAS HHG source in argon are well above this value, experimentally this proved to be insufficient to measure  $4f$ -RABBITT traces. The background of scattered secondary electrons is increasing drastically for low kinetic energies, which makes it difficult to discern photoemission from the  $4f$  levels even in static photoemission spectroscopy as displayed in Fig. 6.2a.

Without major changes in the enhancement cavity setup it is possible to generate high harmonics in neon at significantly higher photon energies. Although this comes at the cost of

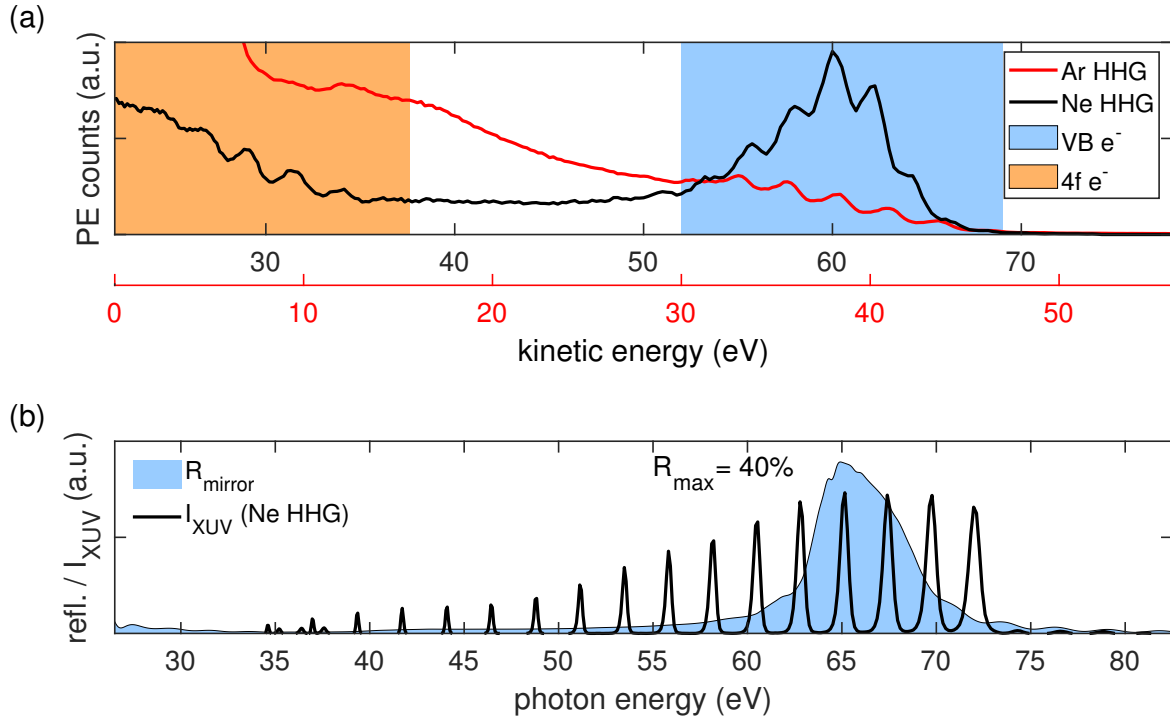


Figure 6.2: **a)** Photoelectron spectra from high harmonics generated in argon (red) and neon (black). Note the different abscissae. Peaks from  $4f$  and valence-band photoelectrons are separated by the  $4f_{7/2}$  binding energy of 31.2 eV. They are well visible with the high photon energies offered by neon HHG but hardly distinguishable with argon harmonics in a dominant background of secondary electrons. **b)** Measured XUV spectrum for HHG in neon with a 300 nm aluminum foil filter (black line) and design reflectivity curve of the utilized XUV mirror (blue filled area).

reduced photon flux, it still enables the measurement of meaningful RABBITT spectrograms within a few minutes. The higher photon energies of neon high harmonics allowed to clearly discern  $4f$ -electron peaks in the photoemission spectra (Fig. 6.2a).

A 300 nm thick aluminum foil was chosen as material for the coaxial filter, because it features a high transmission and proved to be resistant against the high average powers of the IR laser beam. Because of the aluminum absorption edge at 73 eV the reflectivity curve of the utilized XUV mirror was designed to be centered below this value at 65 eV with a FWHM bandwidth of 5 eV (Fig. 6.2b).

Pump-probe measurements with the XUV spectrum in Fig. 6.2b yield the spectrogram shown in Fig. 6.3a. In analogy to the static photoelectron spectra, the RABBITT trace is separated in a high-energy part of valence-band photoelectrons and a low-energy part of  $4f$  photoelectrons and the sideband positions and orders for both parts are marked on the right ordinate.

An anomaly in the otherwise regular pattern can be discerned by bare eye for sideband number 56 at a kinetic energy of around 62 eV and its neighboring harmonic. A more thorough

sideband delay analysis (as described in Section 4.2) yields the delays displayed in Fig. 6.3b (black circles), where two things are particularly striking: i) There is an overall delay offset in photoemission of around 200 as between valence band and  $4f$  electrons. ii) The sideband at 62 eV is delayed by  $148 \pm 40$  as with respect to the other valence band sidebands.

Comparable delays between valence band and  $4f$  photoemission have been observed before in attosecond streaking measurements and have commonly been attributed to the transport time of the photoelectron from within the solid to its surface [8, 9, 14]. It can be modeled by assuming a free-electron-like behavior of the photoelectrons in the solid and accounting for the mean electron emission depth, which corresponds to the electron inelastic mean free path (Section 6.1). Because the  $4f$  electrons are slower but their IMFP is larger they take more time to reach the crystal surface. The result of the free-electron transport delay calculation in Fig. 6.3b (red line) is in reasonable agreement with all  $4f$  and valence-band sidebands except the outlier at 62 eV energy.

Hence, all but one sideband are consistent with the previously conducted tungsten  $4f$ -state referenced attosecond streaking measurements in this core-state referenced RABBITT experiment. As it will be elaborated in the next section this surge in delay can be attributed to final state effects.

### 6.3 Resonant RABBITT sideband delays

The outlier sideband in Fig. 6.3b at 62 eV is delayed by  $148 \pm 40$  as with respect to the other valence band sidebands which cannot be explained by the free-electron transport delay model. There are three possible explanations for this deviation:

**The XUV spectral phase** (more precisely the phase difference between the adjacent harmonics) is part of the sideband phase term (see Eq. 2.35) and attochirp could lead to this phenomenon. However, because the  $4f$  sideband of the same order does not exhibit any comparable surge in delay compared to its neighboring sidebands, the outlier cannot be explained by the spectral phase of the XUV, as this would equally affect  $4f$  and valence-band photoemission. In principle, it could be that the  $4f$  doublet structure partially covers such an effect due to overlap of a mixture of different harmonics and initial states. In Section 6.3.2 it is shown that this is not the case.

**Initial-state effects** have been demonstrated to play a role for photoemission delays from both solids [103] and gases [10, 13]. In general, electrons stemming from states with higher orbital momentum will experience a larger intra-atomic delay in photoemission. As the tungsten valence band is composed of  $sp$  and  $d$  bands (Section 5.2.2), this indeed has a certain influence on the photoemission timing. However, all initial-state related delays, which have been reported so far, were significantly smaller than the here observed 148 as. This could be confirmed by an experiment in the context of this work, which finds a 39 as delay between  $sp$ - and  $d$ -band photoemission (Section 5.3.3).

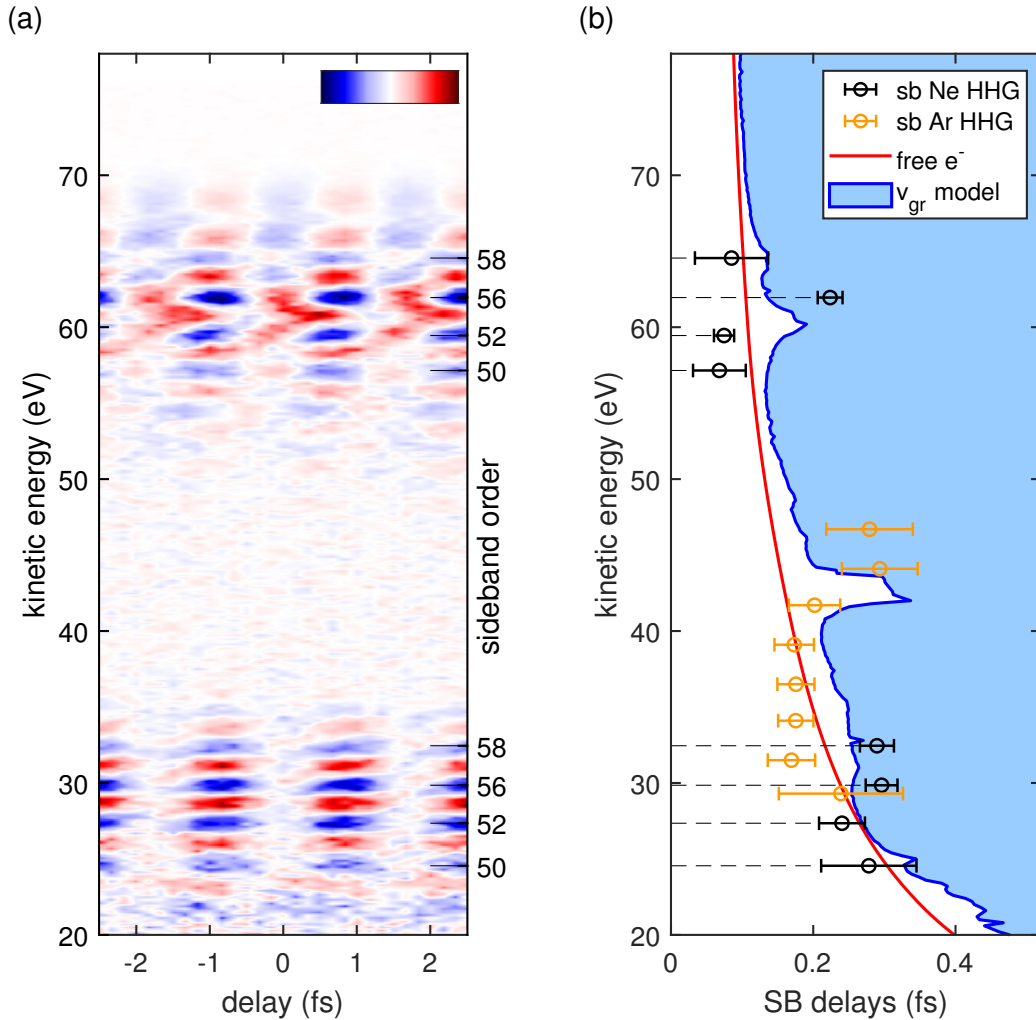


Figure 6.3: **a)** RABBITT spectrogram taken with high harmonics generated in neon. Photoelectrons which form modulated harmonics and sidebands around 60 eV originate from the tungsten valence band, those around 30 eV from the  $4f$  core state. The right ordinate indicates the sideband positions and orders. The dataset was measured in 31 delay steps of 167 as within a total net acquisition time of 145 minutes. **b)** Sideband delays extracted from the spectrogram in a) (black circles) and from the broadband argon harmonics RABBITT spectrogram in Fig. 4.1 (orange circles). The calculated transport delay curve for free electrons (red line) explains the indicated sideband delays well except for a few outliers around 43 and 62 eV. These can be explained by the calculation of the transport delay based on the tungsten final band group velocities, where the blue line indicates the minimum transport delay (maximum group velocity) and the light blue area the entire possible delay range. Note that the absolute sideband delays cannot be determined from the measurement, such that for each dataset a constant delay offset was added. Figure adapted from Ref. [163].

**Final-state effects** can have a significant influence on the photoemission timing as demonstrated in RABBITT experiments on nickel and copper [78, 102, 105, 182]. The magnitude of the reported delays is similar to the  $148 \pm 40$  as that we observed at 62 eV energy.

Having ruled out the first two options the observed surge in photoemission delay must be attributed to a final-state effect. As it will be shown in the next section the measured delays agree well with the final band group velocity model presented in Section 6.1.

### 6.3.1 Final state photoemission delays

In the three-step model of photoemission, the final-state induced delay can be attributed to the transport time of the photoelectron to the surface. This can be modeled by the quotient of the mean emission depth and the band structure dependent group velocity for electrons within the crystal as described in Section 6.1.

The minimum delay obtained from the maximum group velocity at each final energy is indicated by a blue line in Fig. 6.3b, the entire possible delay range in light blue. The group velocity delay curve features a maximum at 60 eV which is in good agreement with the energy of the outlier sideband. The discrepancy in delay magnitude can be attributed to the fact, that the displayed model curve relies on the maximum group velocity and is therefore a lower limit of the expectable delay. It has been observed before, that the photoemission delay at different energies can either follow the group velocity of the final state bands or the free electron behavior within the same measurement [102].

Because the group velocity delay curve exhibits another even more pronounced surge at 43 eV, another RABBITT measurement with high harmonics generated in argon and a broadband XUV mirror was conducted to probe this final energy range. The corresponding spectrogram is depicted in Fig. 4.1 and the delay evaluation procedure including the mirror spectral phase correction in Chapter 4. The resulting sideband delays are displayed in Fig. 6.3b (orange circles) and reproduce well the increase in delay, which is predicted by the group velocity simulation.

Both experimentally observed delay maxima at 43 and 62 eV are shifted by about 2 eV with respect to the model. This could be attributed to a shift in energy of the band structure DFT calculations, which are well known to underestimate band gaps [183].

A closer look at the valence band sidebands in Fig. 6.4a reveals that there is also already a shift in delay within the sideband around 60 eV next to the significantly delayed sideband at 62 eV. This is found by the evaluation of the sideband delay at three different energies separated by 300 meV across the sideband (Fig. 6.4b). The final state related increase in sideband delay at 62 eV already shows up at higher energies of the next lower sideband, thus creating a smoother transition between the valence band photoemission delays. A seemingly similar intra-sideband delay difference in the next higher sideband around 65 eV is at closer inspection insignificant because the shift is small compared to the large error bars.

Fig. 6.4c displays the band structure around the final state resonance. The bands with maximal group velocity at each energy are highlighted in blue and exhibit a shallow segment slightly above 60 eV which leads to the increase in group velocity induced delay in Fig. 6.4b.

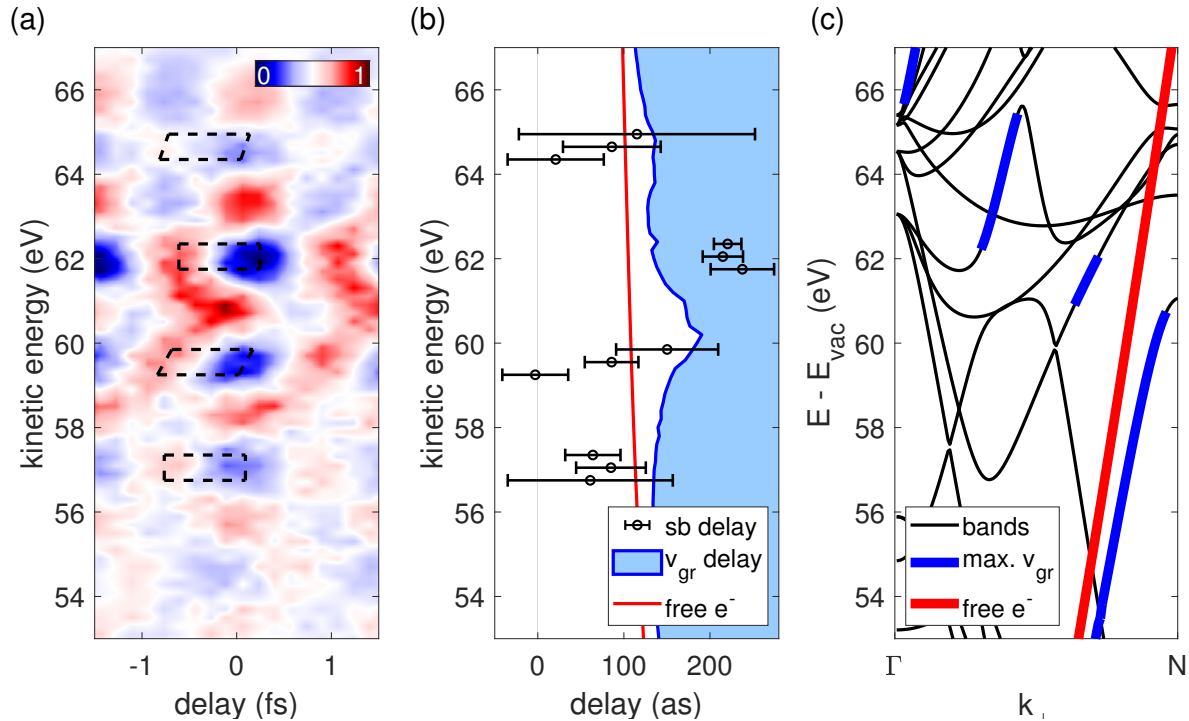


Figure 6.4: **a)** Zoom into the valence band part of the RABBITT spectrogram in Fig. 6.3a. Intra-sideband delays are indicated by the dashed boxes. The sideband slightly below 60 eV exhibits a strong intra-sideband shift. **b)** Delays evaluated at three different energies within the sidebands separated by and integrated over an interval of 300 meV. The increase in delay does not only affect the sideband at 62 eV but is also clearly visible within the next lower sideband. The free-electron and group-velocity based delay models are indicated by a red and blue line respectively. **c)** Band structure of tungsten in emission direction  $\Gamma$ -N together with the free electron dispersion relation (red). The steepest bands at each energy are marked in blue and are comparably shallow around 60 eV and slightly above, which leads to the maximum in group velocity induced delay displayed in b). Figure adapted from Ref. [163].

### 6.3.2 Tungsten $4f$ doublet sideband overlap

So far, it has been neglected that the  $4f$  state in tungsten features a sub-structure: Because it is a deeply bound state it does not experience a strong influence from the periodic structure of a solid but can be treated as a quasi-atomic state and is populated by one spin up and one spin down electron. The two spin states are denoted as  $4f_{5/2}$  and  $4f_{7/2}$ , where the subscript fraction indicates the total angular momentum of the electronic state. As the spin and the orbital momentum interact, these two states will split up in energy and are in the case of the tungsten  $4f$  state separated by 2.2 eV [180]. Classically, this energy splitting can be understood as an energy shift induced by the interaction of the electron spin with the magnetic field created by the electron angular momentum, comparable to an intra-atom Zeeman effect [184].

The doublet structure leads to an overlap of photoelectrons from the different spin states and different high harmonics and could therefore influence the measured sideband delays. In particular, this effect could cover a similar delay surge of the 56<sup>th</sup> 4*f*-electron sideband as it has been observed for the valence electron sidebands (Section 6.3.1). In this case, the increase in delay at 62 eV would have to stem from the XUV spectral phase because it would be independent of the final or initial state. To exclude this scenario, the influence of the doublet structure of the tungsten 4*f* states on the measured sideband delays will be elaborated in this section.

Whereas RABBITT is in principle very well suited to spectrally distinguish photoelectrons from closely neighbored states, there is one important constraint: If the separation between two electronic states is (approximately) a multiple of the IR laser photon energy, the sidebands from one state can overlap with the sidebands or high harmonics of a different order from another state, which makes it very difficult to disentangle their individual contributions.

In the case of tungsten, the separation between the 4*f* doublet states of 2.2 eV is very close to the spacing between the high harmonics of 2.4 eV. Due to the width of the high harmonics and due to the spectrometer resolution, the difference of only 200 meV can currently not be resolved in our experiments. As a consequence, each sideband electron cannot be unambiguously attributed to a specific initial state excited by a specific high harmonic but could either be a 4*f*<sub>7/2</sub> electron excited by the harmonic of order *m* or a 4*f*<sub>5/2</sub> electron excited by the harmonic *m* + 2.

To overcome this kind of problem, a method for the extraction of attosecond delays from spectrally overlapping interferograms was proposed recently [185]. The first step of this approach is to Fourier transform the RABBITT spectrogram along the delay axis. The absolute value of the Fourier transform of the spectrogram in Fig. 6.3a is displayed in Fig. 6.5a and represents the intensity of the individual frequency components in the spectrogram.

As described in Section 4.4 all information that is relevant for the photoemission timing is in the complex-valued  $2\omega_{\text{IR}}$  frequency component  $Z_{2\omega}(E)$  of the spectrogram. Its absolute value indicates the strength of the sideband (or high harmonic) modulation at each final kinetic energy *E* and its phase the sideband delay.

To disentangle the contributions from overlapping spectrograms in  $Z_{2\omega}(E)$  the following expression is fitted to it:

$$Z_{2\omega}(E) = \sum_m A_m \cdot e^{i\phi_m} \cdot P(E - E_m) \quad (6.2)$$

Here, the sum is running over all sidebands and harmonics of order *m* with their modulation amplitude  $A_m$ , their phase  $\phi_m$  and central energy  $E_m$ . The shape of a photoelectron peak excited by a single high harmonic is given by  $P(E)$  (centered around zero kinetic energy in this notation). The line shape can be approximated by the convolution of a high harmonic with the density of states of the probed energy levels (Section 5.2.2). In this case this is the spectral shape of the 4*f* doublet.

The amplitude and phase of the  $2\omega_{\text{IR}}$  component  $Z_{2\omega}(E)$  of the 4*f* part of the spectrogram in Fig. 6.3a are displayed in Fig. 6.5b and c respectively (red line and asterisks). The result

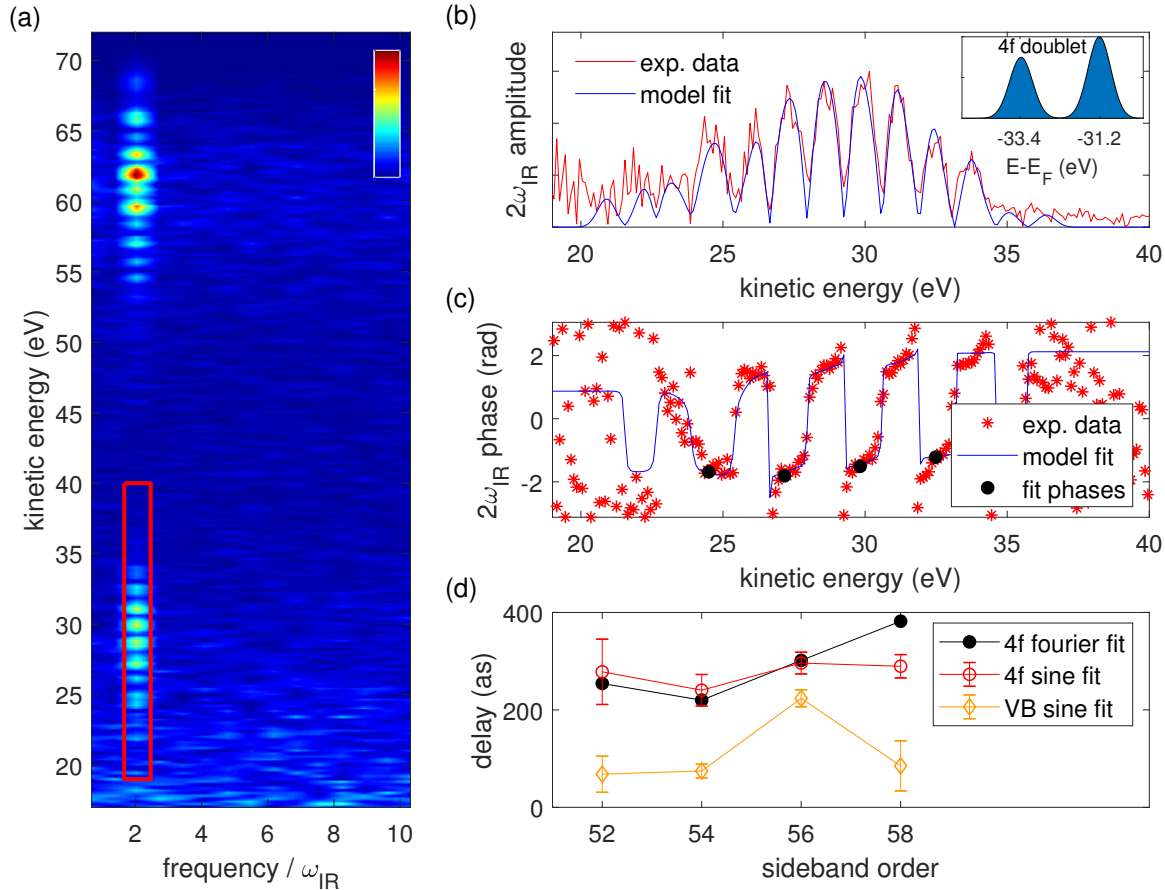


Figure 6.5: **a)** Absolute value of the Fourier transform of the RABBITT spectrogram displayed in Fig. 6.3a. The spectral density features well visible maxima at  $2\omega_{\text{IR}}$ , which correspond to the sideband (and high harmonic) oscillations. The red box indicates the relevant parameter range for the  $4f$ -delay evaluation in **b)** and **c)**. **b)** Spectral density at the sideband oscillation frequency  $2\omega_{\text{IR}}$  in the  $4f$ -photoelectron energy range. Each peak corresponds to an oscillating sideband or high harmonic. The complex-valued experimental data was fitted with a sum of eleven  $4f$ -doublet peaks, whose shape is shown in the inset. The absolute value of the fit result is indicated by the blue line. **c)** Phase of the  $2\omega_{\text{IR}}$  component of the Fourier transformed spectrogram together with the argument of the fit result. The four most prominent sideband phases determined by the Fourier fit are indicated by black dots. **d)** Sideband delays for the  $4f$  photoelectrons obtained from the complex-valued fitting of the Fourier transform together with the sideband delays extracted by sine fits for  $4f$  state and valence band. Figure adapted from Ref. [163].

of the fit with Eq. 6.2 is in both cases indicated by the blue line. For the fit the  $4f$ -doublet photoelectron peak shape  $P(E)$  was modeled by two gaussians (see inset in Fig. 6.5b) whose widths, weights and positions were taken from experimental literature data [180].

The free parameters in the fit were the weights  $A_m$  and phases  $\phi_m$  for a set of eleven individual peaks. The position  $E_m$  of each peak was not fitted individually, but decomposed in  $E_m = E_0 + m \cdot \hbar\omega_{\text{IR}}$  with a fixed IR photon energy and a free energy offset  $E_0$  to be fitted. The fit result reproduces the experimental data well, particularly in the energy range from 23 to 34 eV where there the signal is strongest (Fig. 6.5b and c).

This method for extracting delays from overlapping spectrograms works best for very sharp features of precisely known line shape as it is typically the case for gases rather than solids. This makes it difficult to obtain quantitatively meaningful results for the photoemission from a tungsten crystal from the model. However, the delays obtained by this complex-valued fit approach can help to rule out the possibility, that the overlap of photoelectrons from  $4f$ -doublet structure and the resulting mixture of different initial states and high harmonics significantly changes the sideband delays.

In Fig. 6.5c the actual fit phases  $\phi_m$  of the strongest sidebands are indicated by black dots and in Fig. 6.5d they are compared to the results from the sine fit approach (Section 4.2). For the sideband orders 52 to 56 the values obtained by the two methods agree almost perfectly. Only sideband number 58 is exhibiting a certain deviation. However, it becomes very clear that no sudden surge in delay for the  $4f$  sideband number 56 can be reproduced by this method as it was observed for the valence band electrons (Fig. 6.5d). Consequently, the observed surge in delay of the 56<sup>th</sup> valence band sideband at 62 eV can definitely not be attributed to the XUV spectral phase.

To obtain more reliable results from this promising RABBITT analysis method the exact knowledge of the photoemission spectrum excited by a single high harmonic is crucial. The fabrication of an XUV mirror with a sufficiently small bandwidth to filter out a single high harmonic with a photon energy of 30 to 50 eV is almost impossible, because even well-suited mirror materials absorb a significant amount of XUV and consequently only a relatively low number of mirror layers is contributing to the reflectivity of the mirror.

One possible approach is to combine a mirror with a sharp absorption edge of a transmissive foil filter, such as germanium, titanium or scandium. Together with the detection of the exact XUV spectrum after the multilayer mirror, which was implemented in our setup in the context of this work (Section 3.3), this can help to identify and disentangle photoemission from not entirely suppressed high harmonics outside the mirror bandwidth and will enable more precise results from this Fourier fit method. By this means, it could even be possible to determine individual photoemission delays for the  $4f_{5/2}$  and  $4f_{7/2}$  state or different band types within the valence band in future experiments.

## 6.4 Photoemission delays in tungsten carbide

Thanks to the high energy resolution of the RABBITT technique it allows for distinguishing photoemission spectra from different materials and chemical compounds. There are two main approaches in photoemission spectroscopy to do so:

- i) Use ARPES to identify a material by means of its band structure.
- ii) Probe core-states to determine their material-specific binding energies.

Our experimental setup is perfectly suited for both these techniques because of the angle-resolving electron spectrometer and because of the high photon energies which allow for accessing deeply bound core states.

The angle resolved data displayed in Fig. 6.6a indeed exhibits differences between the valence band structure in the two presented measurements. One of the datasets was measured within a time-resolved measurement run of several hours while regularly cleaning the tungsten crystal. The other one was done without any crystal cleaning procedure and afterwards proved to be covered by a tungsten carbide (WC) layer as it will be elaborated in the rest of this section. Although the dispersion discrepancies in Fig. 6.6a may not be sufficient to unambiguously identify the different materials they are clearly visible.

In the  $4f$ -RABBITT spectrograms the difference between the contaminated and the clean sample is even more striking as displayed in Figs. 6.6b and c: The sample with the tungsten carbide layer exhibits pronounced double peaks for the  $4f$  photoemission, which are separated by 600 meV. This energy difference corresponds perfectly to the chemical shift that the tungsten  $4f$  peaks experience in tungsten carbide [186].

One might expect that the dominant tungsten compound is tungsten oxide rather than carbide because of the inevitably present residual oxygen atoms in the vacuum chamber. This would result in a chemical shift of 3.3 eV [186]. However, because our sample is constantly heated up to 500 to 700°C due to the high impinging average IR laser power and because we are constantly purging the experimental chamber with argon to prevent oxidation, these experimental conditions correspond almost perfectly to those described in literature for tungsten carbide synthesis [187]. The high energy XUV photons additionally contribute carbon atoms to the formation of the WC layer by cracking hydrocarbons which are even in ultra-high vacuum conditions inevitably present to a small extent.

As shown in Fig. 6.6d a fit to the sum of the W and WC sidebands of the carbide-covered spectrogram yields a delay of  $242 \pm 64$  as between photoemission from tungsten and tungsten carbide. This significant difference can be explained by the transport delay of photoelectrons to the crystal surface. As the tungsten carbide layer forms on the surface of the crystal, the mean emission depth is significantly smaller than for the pure tungsten bulk material.

The mean emission depth  $l_{WC}$  of an electron from a WC layer of thickness  $d$  can be calculated from the exponential damping of the primary electrons with the inelastic mean free path  $\lambda$  with the following formula:

$$l_{WC}(d) = \lambda \cdot \frac{1 - e^{-d/\lambda} (1 + d/\lambda)}{1 - e^{-d/\lambda}} \quad (6.3)$$

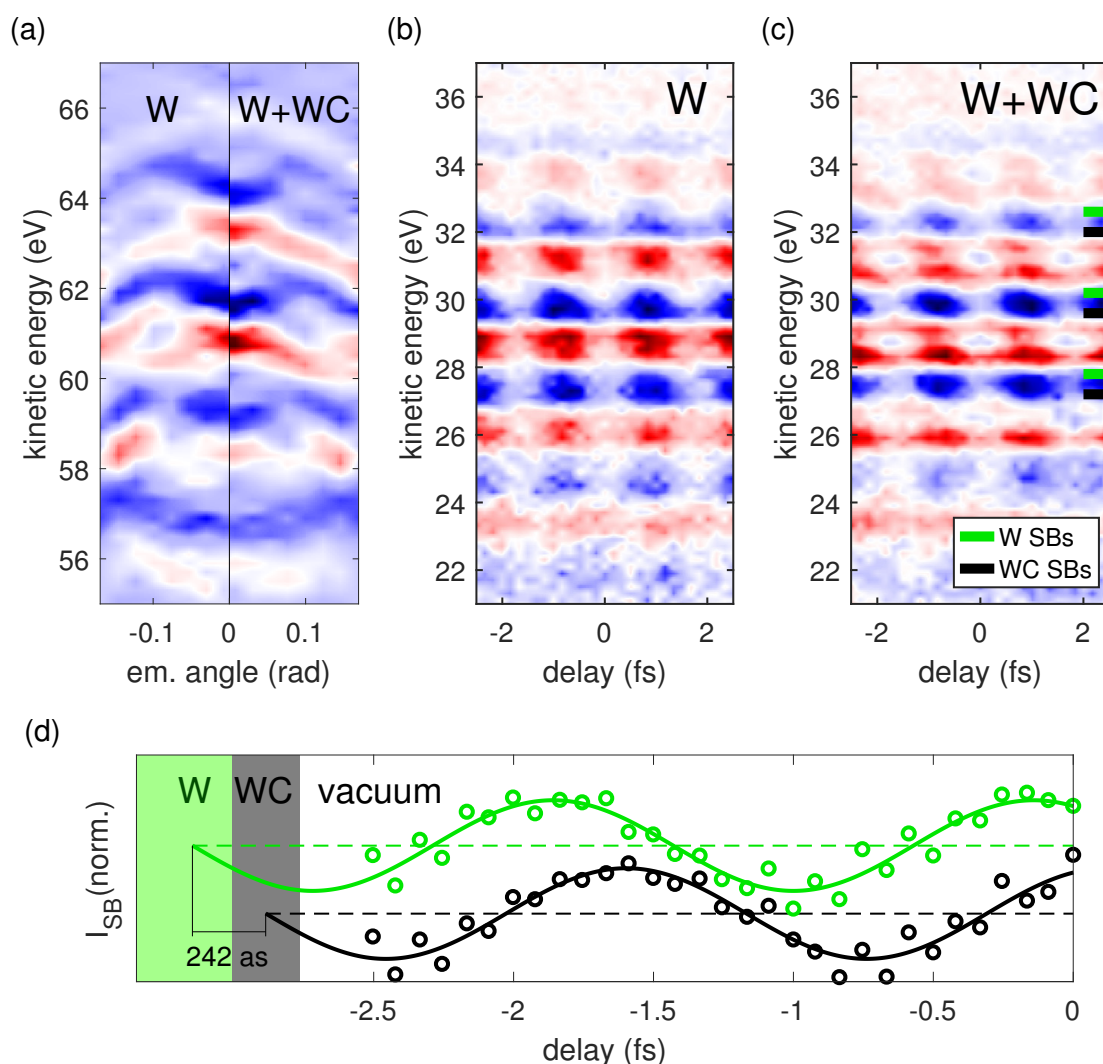


Figure 6.6: **a)** Angle resolved PES data measured on a clean tungsten surface (left) and a tungsten crystal covered with a certain amount of tungsten carbide (right). **b)** RABBITT spectrogram of 4f photoelectrons from tungsten measured within a total net acquisition time of 145 minutes. **c)** RABBITT spectrogram of 4f photoelectrons from tungsten and tungsten carbide (net acquisition time 280 minutes). A 600 meV chemical shift between the two materials leads to a double peak structure. Sideband positions are marked on the right. **d)** Sum of all sidebands indicated in c) in identical colors. The 4f sidebands emitted from the tungsten bulk are delayed by  $242 \pm 64$  as. The relative delay is attributed to the different emission depth of photoelectrons of the W bulk and the WC layer which forms at the surface as schematically illustrated on the left.

For a layer thickness  $d < \lambda$  the mean emission depth is  $l \approx d/2$ , and it converges towards  $\lambda$  for  $d \gg \lambda$ . Because it is almost identical for all chemical elements we use calculated values for the energy-dependent inelastic mean free path in tungsten also for tungsten carbide. The XUV attenuation length in tungsten at the relevant energies is at least one order of magnitude higher than the electron mean free path and its influence can therefore be neglected [154, 177].

The mean emission depth of the bulk material is simply  $l_W = \lambda + d$  such that the difference in emission depth between bulk tungsten and the tungsten carbide top layer is:

$$\Delta l(d) = l_W(d) - l_{WC}(d) = \frac{d}{1 - e^{-d/\lambda}} \quad (6.4)$$

From this formula the thickness of the carbide layer can be derived. The measured sideband delay between W and WC and the classical electron velocity yield a  $\Delta l$  of 7.86 Å. The inelastic mean free path  $\lambda$  at 30 eV is 7.70 Å [177]. From these values and Eq. 6.4 results a mean tungsten carbide layer thickness of  $0.3 \pm 3.7$  Å.

The upper bound thickness of 4 Å is on the order of magnitude of the 3 Å size of the tungsten carbide unit cell [188] which indicates a very thin average coverage of tungsten carbide. The fact that the W and WC peaks in the spectrogram in Fig. 6.6 are of comparable intensity corroborates this finding. If the WC layer were significantly thicker than calculated it would dominate the spectrogram at a mean emission depth of only 7.70 Å.

The findings of this section show how the high energy resolution and the high photon energy provided by our source allow to distinguish different materials determine layer thicknesses and discern a possible contamination of a sample. This could not easily be achieved with the photon energies of most single-pass attosecond pulse train sources and could easily go unnoticed in attosecond streaking experiments due to their broad excitation bandwidth.

# Chapter 7

## Conclusion and outlook

Within the scope of this thesis the generation of high harmonics in an enhancement cavity has enabled the first attosecond PES experiments at MHz pulse repetition rate. The high repetition rate allowed for PES measurements at count rates of up to  $10^6$  detected photoelectrons per second without the interference of space-charge effects. Therefore, the full spectral resolution offered by well-separated high harmonics with a width of a few hundred meV was preserved and has been used to investigate the influence of initial and final states on the photoemission timing.

The combination of angle-resolved photoelectron detection and high energy resolution made it possible to identify the contributions different initial bands. Subsequently, a delay in photoemission of  $39 \pm 18$  as from *d* bands compared to *sp* bands was found in the tungsten valence band. The delay is attributed to the different initial angular momentum of the photoelectrons. So far, this effect had only been investigated in gas atoms or deeply bound states in a solid but not between different band types in the valence band.

Furthermore, the influence of final states on the photoemission timing from tungsten was investigated and a surge in delay of  $148 \pm 40$  as at 62 eV kinetic energy was found. This phenomenon was explained by an electron transport time model based on the group velocities of the final bands. The high photon energies of the MEGAS source allowed for addressing these high kinetic energies as well as referencing their photoemission timing to the deeply bound *4f* core states in tungsten in the first core-state RABBITT experiment on a solid. The transport time model was confirmed by another broadband RABBITT measurement which found a similar increase in photoemission delay at 43 eV kinetic energy in accordance with the model.

The high energy resolution offered by space-charge free RABBITT measurements on solids also allowed for distinguishing photoemission from tungsten and tungsten carbide. A relative delay of  $242 \pm 64$  as was observed and can be explained by geometrical electron transport times. The experimental setup and scientific findings presented in this thesis lay the groundwork for a wide scope of possible future experiments to further explore the electronic properties and dynamics of other solids. Their often complex band structures call for precise characterization of the excitation spectrum and of the response of the system under study.

While the former has been implemented within the scope of this thesis, the latter ideally requires monochromatic excitation to allow for unambiguous and direct identification of initial states, their dispersion and their photoelectron spectrum with high precision. A first step towards monochromaticity has been undertaken in this thesis by employing a narrowband XUV mirror and centering a high harmonic at the maximum reflectivity by means of intracavity blueshift control.

To further improve this approach and suppress out-of-bandwidth high harmonics suitable metal foil filters can be employed. Materials like titanium or tantalum can for example allow for spectral filtering of a single harmonic around 30 eV photon energy. Longer driving laser pulses would additionally result in narrower high harmonics. This can easily be implemented in the HHG system and would further improve the energy resolution, particularly in static monochromatic PES measurements for characterization purposes.

Based on accurately measured lineshapes of the electronic states, the disentanglement of their contributions in more broadband attosecond-resolved PES measurements will become feasible. The Fourier-fit approach for the analysis of overlapping spectrograms, which was also applied in this work, would enable the precise and energy-resolved extraction of photoemission delays between very closely neighbored states or overlapping bands. This will be crucial for the investigation of electron dynamics in materials with complicated band structures.

The angular resolution offered by our electron spectrometer and the sample rotation stage can be employed to investigate and compare the photoemission timing from different parts in the reciprocal space in a crystalline sample. The high flux offered by the MEGAS XUV source will be key for a good signal-to-noise ratio in the evaluation of 4-dimensional datasets, comprising the 2D-crystal momentum parallel to the surface, the photoelectron kinetic energy and the XUV-IR pump-probe delay.

Most materials are more sensitive to high temperatures than tungsten crystals. Therefore, one of the next steps will be to reduce the heat load on the sample. In principle, the IR laser power can be reduced at the cost of RABBITT sideband modulation depth resulting in longer acquisition times. Although this could be affordable at the high flux of our HHG source, a more promising approach is to optimize the spatial profile of the IR focus. This could enable unchanged probe intensities at a fraction of the current average laser power on the sample. In addition, active sample cooling can be implemented.

Because of the striking band structure of topological insulators and the surface sensitivity of photoemission experiments ARPES is perfectly suited for studying these novel materials. Hence, one of the next subjects of study could be to observe angle-resolved electron dynamics in real time in these intensely researched systems with their unique properties and promising applications. Within the framework of the advances and findings presented in this work such an experiment can now be readily realized.

# References

- [1] N. H. Burnett, H. A. Baldis, M. C. Richardson, and G. D. Enright, “*Harmonic generation in CO<sub>2</sub> laser target interaction*”, Applied Physics Letters **31**, 172–174 (1977).
- [2] A. McPherson, G. Gibson, H. Jara, U. Johann, T. S. Luk, I. A. McIntyre, K. Boyer, and C. K. Rhodes, “*Studies of multiphoton production of vacuum-ultraviolet radiation in the rare gases*”, Journal of the Optical Society of America B **4**, 595 (1987).
- [3] P. M. Paul, E. S. Toma, P. Breger, G. Mullot, F. Auge, P. Balcou, H. G. Muller, and P. Agostini, “*Observation of a train of attosecond pulses from high harmonic generation*”, Science **292**, 1689–1692 (2001).
- [4] M. Hentschel, R. Kienberger, C. Spielmann, G. A. Reider, N. Milosevic, T. Brabec, P. Corkum, U. Heinzmann, M. Drescher, and F. Krausz, “*Attosecond metrology*”, Nature **414**, 509–513 (2001).
- [5] M. Drescher, M. Hentschel, R. Kienberger, G. Tempea, C. Spielmann, G. A. Reider, P. B. Corkum, and F. Krausz, “*X-ray pulses approaching the attosecond frontier*”, Science **291**, 1923–1927 (2001).
- [6] T. Remetter, P. Johnsson, J. Mauritsson, K. U. Y. Ni, F. Epine, E. Gustafsson, M. Kling, J. Khan, R. Opez-Martens, K. Schafer, M. Vrakking, and A. L’Huillier, “*Attosecond electron wave packet interferometry*”, Nature Physics **2** (2006).
- [7] M. Uiberacker, T. Uphues, M. Schultze, A. J. Verhoef, V. Yakovlev, M. F. Kling, J. Rauschenberger, N. M. Kabachnik, H. Schröder, M. Lezius, K. L. Kompa, H.-G. Muller, M. J. J. Vrakking, S. Hendel, U. Kleineberg, U. Heinzmann, M. Drescher, and F. Krausz, “*Attosecond real-time observation of electron tunnelling in atoms*”, Nature **446**, 627–632 (2007).
- [8] A. L. Cavalieri, N. Müller, T. Uphues, V. S. Yakovlev, A. Baltuska, B. Horvath, B. Schmidt, L. Blümel, R. Holzwarth, S. Hendel, M. Drescher, U. Kleineberg, P. M. Echenique, R. Kienberger, F. Krausz, and U. Heinzmann, “*Attosecond spectroscopy in condensed matter*”, Nature **449**, 1029–1032 (2007).
- [9] C. Lemell, B. Solleder, K. Tokési, and J. Burgdoerfer, “*Simulation of attosecond streaking of electrons emitted from a tungsten surface*”, Physical Review A **79** (2009).

- [10] M. Schultze, M. Fiess, N. Karpowicz, J. Gagnon, M. Korbman, M. Hofstetter, S. Neppl, A. Cavalieri, Y. Komminos, T. Mercouris, C. Nicolaides, R. Pazourek, S. Nagele, J. Feist, J. Burgdörfer, A. Azzeer, R. Ernstorfer, R. Kienberger, U. Kleineberg, and V. Yakovlev, “*Delay in photoemission*”, *Science* **328**, 1658–62 (2010).
- [11] R. Locher, M. Lucchini, J. Herrmann, M. Sabbar, M. Weger, A. Ludwig, L. Castiglioni, M. Greif, M. Hengsberger, L. Gallmann, and U. Keller, “*Versatile attosecond beamline in a two-foci configuration for simultaneous time-resolved measurements*”, *Review of Scientific Instruments* **85**, 013113 (2014).
- [12] R. Locher, L. Castiglioni, M. Lucchini, M. Greif, L. Gallmann, J. Osterwalder, M. Hengsberger, and U. Keller, “*Energy-dependent photoemission delays from noble metal surfaces by attosecond interferometry*”, *Optica* **2**, 405 (2015).
- [13] M. Isinger, R. J. Squibb, D. Busto, S. Zhong, A. Harth, D. Kroon, S. Nandi, C. L. Arnold, M. Miranda, J. M. Dahlström, E. Lindroth, R. Feifel, M. Gisselbrecht, and A. L’Huillier, “*Photoionization in the time and frequency domain*”, *Science* **358**, 893–896 (2017).
- [14] M. Ossiander, J. Riemensberger, S. Neppl, M. Mittermair, M. Schäffer, A. Duensing, M. Wagner, R. Heider, M. Wurzer, M. Gerl, M. Schnitzenbaumer, J. Barth, F. Libisch, C. Lemell, J. Burgdörfer, P. Feulner, and R. Kienberger, “*Absolute timing of the photoelectric effect*”, *Nature* **561** (2018).
- [15] J. Riemensberger, S. Neppl, D. Potamianos, M. Schäffer, M. Schnitzenbaumer, M. Ossiander, C. Schröder, A. Guggenmos, U. Kleineberg, D. Menzel, F. Allegretti, J. V. Barth, R. Kienberger, P. Feulner, A. G. Borisov, P. M. Echenique, and A. K. Kazansky, “*Attosecond dynamics of sp-band photoexcitation*”, *Physical Review Letters* **123**, 176801 (2019).
- [16] M. Ossiander, F. Siegrist, V. Shirvanyan, R. Pazourek, A. Sommer, T. Latka, A. Guggenmos, S. Nagele, J. Feist, J. Burgdörfer, R. Kienberger, and M. Schultze, “*Attosecond correlation dynamics*”, *Nature Physics* **13**, 280–285 (2016).
- [17] E. Goulielmakis, M. Schultze, M. Hofstetter, V. S. Yakovlev, J. Gagnon, M. Uiberacker, A. L. Aquila, E. M. Gullikson, D. T. Attwood, R. Kienberger, F. Krausz, and U. Kleineberg, “*Single-cycle nonlinear optics*”, *Science* **320**, 1614–1617 (2008).
- [18] K. Zhao, Q. Zhang, M. Chini, Y. Wu, X. Wang, and Z. Chang, “*Tailoring a 67 attosecond pulse through advantageous phase-mismatch*”, *Optics Letters* **37**, 3891–3893 (2012).
- [19] J. Li, X. Ren, Y. Yin, K. Zhao, A. Chew, Y. Cheng, E. Cunningham, Y. Wang, S. Hu, Y. Wu, M. Chini, and Z. Chang, “*53-attosecond x-ray pulses reach the carbon K-edge*”, *Nature Communications* **8** (2017).
- [20] T. Gaumnitz, A. Jain, Y. Pertot, M. Huppert, I. Jordan, F. Ardana-Lamas, and H. J. Wörner, “*Streaking of 43-attosecond soft-x-ray pulses generated by a passively cep-stable mid-infrared driver*”, *Optics Express* **25**, 27506–27518 (2017).

- 
- [21] S. Passlack, S. Mathias, O. Andreyev, D. Mittnacht, M. Aeschlimann, and M. Bauer, “*Space charge effects in photoemission with a low repetition, high intensity femtosecond laser source*”, *Journal of Applied Physics* **100**, 024912 (2006).
- [22] A. Pietzsch, A. Föhlich, M. Beye, M. Deppe, F. Hennies, M. Nagasono, E. Suljoti, W. Wurth, C. Gahl, K. Döbrich, and A. Melnikov, “*Towards time resolved core level photoelectron spectroscopy with femtosecond X-ray free-electron lasers*”, *New Journal of Physics* **10**, 033004 (2008).
- [23] S. Hellmann, K. Rossnagel, M. Marczynski-Bühlow, and L. Kipp, “*Vacuum space-charge effects in solid-state photoemission*”, *Physical Review B* **79** (2009).
- [24] T. Saule, S. Heinrich, J. Schoetz, N. Lilienfein, M. Högner, O. deVries, M. Plötner, J. Weitenberg, D. Esser, J. Schulte, P. Russbueltdt, J. Limpert, M. Kling, U. Kleineberg, and I. Pupeza, “*High-flux ultrafast extreme-ultraviolet photoemission spectroscopy at 18.4 MHz pulse repetition rate*”, *Nature Communications* **10** (2019).
- [25] I. Pupeza, C. Zhang, M. Högner, and J. Ye, “*Extreme-ultraviolet frequency combs for precision metrology and attosecond science*”, *Nature Photonics* (2021).
- [26] M. DiDomenico, “*Small-signal analysis of internal (coupling-type) modulation of lasers*”, *Journal of Applied Physics* **35**, 2870–2876 (1964).
- [27] L. E. Hargrove, R. L. Fork, and M. A. Pollack, “*Locking of He–Ne laser modes induced by synchronous intracavity modulation*”, *Applied Physics Letters* **5**, 4–5 (1964).
- [28] K. Renk, *Basics of Laser Physics: For Students of Science and Engineering*, Graduate Texts in Physics (Springer Berlin Heidelberg, 2012).
- [29] D. Meschede, *Optik, Licht und Laser*, Teubner Studienbücher Physik (Vieweg+Teubner Verlag, 2015).
- [30] R. Holzwarth, T. Udem, T. W. Hänsch, J. C. Knight, W. J. Wadsworth, and P. S. J. Russell, “*Optical frequency synthesizer for precision spectroscopy*”, *Physical Review Letters* **85**, 2264–2267 (2000).
- [31] S. Schilt and T. Südmeyer, “*Carrier-envelope offset stabilized ultrafast diode-pumped solid-state lasers*”, *Applied Sciences* **5**, 787–816 (2015).
- [32] D. J. Jones, S. A. Diddams, J. K. Ranka, A. Stentz, R. S. Windeler, J. L. Hall, and S. T. Cundiff, “*Carrier-envelope phase control of femtosecond mode-locked lasers and direct optical frequency synthesis*”, *Science* **288**, 635–639 (2000).
- [33] M. Zürch, C. Kern, and C. Spielmann, “*XUV coherent diffraction imaging in reflection geometry with low numerical aperture*”, *Optics Express* **21**, 21131–21147 (2013).

- [34] M. Zuerch, J. Rothhardt, S. Hädrich, S. Demmler, M. Krebs, J. Limpert, A. Tünnermann, A. Guggenmos, U. Kleineberg, and C. Spielmann, “*Real-time and sub-wavelength ultrafast coherent diffraction imaging in the extreme ultraviolet*”, *Scientific Reports* **4**, 1–5 (2014).
- [35] D. Gardner, M. Tanksalvala, E. Shanblatt, X. Zhang, B. Galloway, C. Porter, R. Karl, C. Bevis, D. Adams, M. Murnane, and G. Mancini, “*Subwavelength coherent imaging of periodic samples using a 13.5 nm tabletop high-harmonic light source*”, *Nature Photonics* **11** (2017).
- [36] A. Ozawa, J. Rauschenberger, C. Gohle, M. Herrmann, D. R. Walker, V. Pervak, A. Fernandez, R. Graf, A. Apolonski, R. Holzwarth, F. Krausz, T. W. Hänsch, and T. Udem, “*High harmonic frequency combs for high resolution spectroscopy*”, *Physical Review Letters* **100**, 253901 (2008).
- [37] A. Cingöz, D. C. Yost, T. K. Allison, A. Ruehl, M. E. Fermann, I. Hartl, and J. Ye, “*Direct frequency comb spectroscopy in the extreme ultraviolet*”, *Nature* **482**, 68–71 (2012).
- [38] H.-S. Kim, P. Baksh, M. Odstreil, M. Miszczak, J. Frey, L. Juschkin, and W. Brocklesby, “*Lloyd’s mirror interference lithography with EUV radiation from a high-harmonic source*”, *Applied Physics Express* **9**, 076701 (2016).
- [39] P. B. Corkum, “*Plasma perspective on strong field multiphoton ionization*”, *Physical Review Letters* **71**, 1994–1997 (1993).
- [40] J. L. Krause, K. J. Schafer, and K. C. Kulander, “*High-order harmonic generation from atoms and ions in the high intensity regime*”, *Physical Review Letters* **68**, 3535–3538 (1992).
- [41] B. Xue, Y. Tamaru, Y. Fu, H. Yuan, P. Lan, O. D. Mücke, A. Suda, K. Midorikawa, and E. J. Takahashi, “*Fully stabilized multi-TW optical waveform synthesizer: Toward gigawatt isolated attosecond pulses*”, *Science Advances* **6** (2020).
- [42] J. Luo, W. Hong, Q. Zhang, K. Liu, and P. Lu, “*Dramatic cutoff extension and broadband supercontinuum generation in multi-cycle two color pulses*”, *Optics Express* **20**, 9801–9809 (2012).
- [43] A. D. Shiner, C. Trallero-Herrero, N. Kajumba, H.-C. Bandulet, D. Comtois, F. Légaré, M. Giguère, J.-C. Kieffer, P. B. Corkum, and D. M. Villeneuve, “*Wavelength scaling of high harmonic generation efficiency*”, *Physical Review Letters* **103**, 073902 (2009).
- [44] E. L. F. ao Filho, V. M. Gkortsas, A. Gordon, and F. X. Kärtner, “*Analytic scaling analysis of high harmonic generation conversion efficiency*”, *Optics Express* **17**, 11217–11229 (2009).
- [45] J. Tate, T. Augustine, H. G. Muller, P. Salières, P. Agostini, and L. F. DiMauro, “*Scaling of wave-packet dynamics in an intense midinfrared field*”, *Physical Review Letters* **98**, 013901 (2007).

- 
- [46] W. Cao, P. Lu, P. Lan, X. Wang, and G. Yang, “Single-attosecond pulse generation with an intense multicycle driving pulse”, *Physical Review A* **74**, 063821 (2006).
- [47] P. B. Corkum, N. H. Burnett, and M. Y. Ivanov, “Subfemtosecond pulses”, *Optics Letters* **19**, 1870–1872 (1994).
- [48] P. Tzallas, E. Skantzakis, C. Kalpouzos, E. Benis, G. Tsakiris, and D. Charalambidis, “Generation of intense continuum extreme-ultraviolet radiation by many-cycle laser fields”, *Nature Physics* **3**, 846 – 850 (2007).
- [49] T. Hammond, G. Brown, K. T. Kim, D. Villeneuve, and P. Corkum, “Attosecond pulses measured from the attosecond lighthouse”, *Nature Photonics* **10** (2016).
- [50] C. M. Heyl, J. Gdde, A. L’Huillier, and U. Hfer, “High-order harmonic generation with  $\mu\text{j}$  laser pulses at high repetition rates”, *Journal of Physics B: Atomic, Molecular and Optical Physics* **45**, 074020 (2012).
- [51] M. Lewenstein, P. Salires, and A. L’Huillier, “Phase of the atomic polarization in high-order harmonic generation”, *Physical Review A* **52**, 4747–4754 (1995).
- [52] P. Balcou, A. S. Dederichs, M. B. Gaarde, and A. L’Huillier, “Quantum-path analysis and phase matching of high-order harmonic generation and high-order frequency mixing processes in strong laser fields”, *Journal of Physics B: Atomic, Molecular and Optical Physics* **32**, 2973–2989 (1999).
- [53] S. Kazamias, S. Daboussi, O. Guilbaud, K. Cassou, D. Ros, B. Cros, and G. Maynard, “Pressure-induced phase matching in high-order harmonic generation”, *Physical Review A* **83** (2011).
- [54] A. Rundquist, C. G. Durfee, Z. Chang, C. Herne, S. Backus, M. M. Murnane, and H. C. Kapteyn, “Phase-matched generation of coherent soft x-rays”, *Science* **280**, 1412–1415 (1998).
- [55] A. Paul, E. A. Gibson, X. Zhang, A. Lytle, T. Popmintchev, X. Zhou, M. M. Murnane, I. P. Christov, and H. C. Kapteyn, “Phase-matching techniques for coherent soft X-Ray generation”, *IEEE Journal of Quantum Electronics* **42**, 14–26 (2006).
- [56] T. Popmintchev, M.-C. Chen, A. Bahabad, M. Gerrity, P. Sidorenko, O. Cohen, I. P. Christov, M. M. Murnane, and H. C. Kapteyn, “Phase matching of high harmonic generation in the soft and hard x-ray regions of the spectrum”, *Proceedings of the National Academy of Sciences of the United States of America* **106**, 10516–10521 (2009).
- [57] H. Carstens, N. Lilienfein, S. Holzberger, C. Jocher, T. Eidam, J. Limpert, A. Tnnermann, J. Weitenberg, D. C. Yost, A. Alghamdi, Z. Alahmed, A. Azzeer, A. Apolonski, E. Fill, F. Krausz, and I. Pupeza, “Megawatt-scale average-power ultrashort pulses in an enhancement cavity”, *Optics Letters* **39**, 2595–2598 (2014).

- [58] R. J. Jones and J. Ye, “*Femtosecond pulse amplification by coherent addition in a passive optical cavity*”, *Optics Letters* **27**, 1848–1850 (2002).
- [59] R. J. Jason, I. Thomann, and J. Ye, “*Precision stabilization of femtosecond lasers to high-finesse optical cavities*”, *Physical Review A* **69**, 1286 (2004).
- [60] C. Gohle, T. Udem, M. Herrmann, J. Rauschenberger, R. Holzwarth, H. A. Schuessler, F. Krausz, and T. W. Hänsch, “*A frequency comb in the extreme ultraviolet*”, *Nature* **436**, 234–237 (2005).
- [61] R. J. Jones, K. D. Moll, M. J. Thorpe, and J. Ye, “*Phase-coherent frequency combs in the vacuum ultraviolet via high-harmonic generation inside a femtosecond enhancement cavity*”, *Physical Review Letters* **94**, 193201 (2005).
- [62] E. Lorek, E. W. Larsen, C. M. Heyl, S. Carlström, D. Paleček, D. Zigmantas, and J. Mauritson, “*High-order harmonic generation using a high-repetition-rate turnkey laser*”, *Review of Scientific Instruments* **85**, 123106 (2014).
- [63] J. Rothhardt, S. Hädrich, Y. Shamir, M. Tschernajew, R. Klas, A. Hoffmann, G. K. Tadesse, A. Klenke, T. Gottschall, T. Eidam, J. Limpert, A. Tünnermann, R. Boll, C. Bomme, H. Dachraoui, B. Erk, M. Di Fraia, D. A. Horke, T. Kierspel, T. Mullins, A. Przystawik, E. Savelyev, J. Wiese, T. Laarmann, J. Küpper, and D. Rolles, “*High-repetition-rate and high-photon-flux 70 eV high-harmonic source for coincidence ion imaging of gas-phase molecules*”, *Optics Express* **24**, 18133–18147 (2016).
- [64] E. J. Takahashi, Y. Nabekawa, H. Mashiko, H. Hasegawa, A. Suda, and K. Midorikawa, “*Generation of strong optical field in soft X-ray region by using high-order harmonics*”, *IEEE Journal of Selected Topics in Quantum Electronics* **10**, 1315–1328 (2004).
- [65] W. Nagourney, *Quantum Electronics for Atomic Physics and Telecommunication* (Oxford University Press, Oxford, 2014).
- [66] D. C. Yost, A. Cingöz, T. K. Allison, A. Ruehl, M. E. Fermann, I. Hartl, and J. Ye, “*Power optimization of XUV frequency combs for spectroscopy applications invited*”, *Optics Express* **19**, 23483–23493 (2011).
- [67] I. Pupeza, S. Holzberger, T. Eidam, H. Carstens, D. Esser, J. Weitenberg, P. Rußbüldt, J. Rauschenberger, J. Limpert, T. Udem, A. Tünnermann, T. W. Hänsch, A. Apolonski, F. Krausz, and E. Fill, “*Compact high-repetition-rate source of coherent 100 eV radiation*”, *Nature Photonics* **7**, 608–612 (2013).
- [68] T. K. Allison, A. Cingöz, D. C. Yost, and J. Ye, “*Extreme nonlinear optics in a femtosecond enhancement cavity*”, *Physical Review Letters* **107**, 183903 (2011).

- 
- [69] S. Holzberger, N. Lilienfein, H. Carstens, T. Saule, M. Högner, F. Lücking, M. Trubetskov, V. Pervak, T. Eidam, J. Limpert, A. Tünnermann, E. Fill, F. Krausz, and I. Pupeza, “*Femtosecond enhancement cavities in the nonlinear regime*”, *Physical Review Letters* **115**, 023902 (2015).
- [70] T. Saule, “*Cavity-enhanced high harmonic generation for multi-MHz ultra-fast photoemission spectroscopy*”, Ph.D. thesis, Ludwig-Maximilians-Universität München (2018).
- [71] J. Lee, D. R. Carlson, and R. J. Jones, “*Optimizing intracavity high harmonic generation for XUV fs frequency combs*”, *Optics express* **19**, 23315–23326 (2011).
- [72] Y. Mairesse, A. de Bohan, L. J. Frasinski, H. Merdji, L. C. Dinu, P. Monchicourt, P. Breger, M. Kovačev, R. Taïeb, B. Carré, H. G. Muller, P. Agostini, and P. Salières, “*Attosecond synchronization of high-harmonic soft X-rays*”, *Science* **302**, 1540–1543 (2003).
- [73] M. Kotur, D. Guenot, . Jiménez-Galán, D. Kroon, E. Larsen, M. Louisy, S. Bengtsson, M. Miranda, J. Mauritsson, C. Arnold, S. Canton, M. Gisselbrecht, T. Carette, J. Dahlström, E. Lindroth, A. Maquet, L. Argenti, F. Martín, and A. L’Huillier, “*Spectral phase measurement of a fano resonance using tunable attosecond pulses*”, *Nature Communications* **7** (2016).
- [74] S. Baker, J. S. Robinson, C. A. Haworth, H. Teng, R. A. Smith, C. C. Chirilă, M. Lein, J. W. G. Tisch, and J. P. Marangos, “*Probing proton dynamics in molecules on an attosecond time scale*”, *Science* **312**, 424–427 (2006).
- [75] F. Kelkensberg, W. Siu, J. Perez-Torres, F. Morales, G. Gademann, A. Rouzée, P. Johnsson, M. Lucchini, F. Calegari, J. Sanz-Vicario, F. Martín, and M. Vrakking, “*Attosecond control in photoionization of hydrogen molecules*”, *Physical Review Letters* **107**, 043002 (2011).
- [76] W. Siu, F. Kelkensberg, G. Gademann, A. Rouzee, P. Johnsson, D. Dowek, M. Lucchini, F. Calegari, U. De Giovannini, A. Rubio, R. Lucchese, H. Kono, F. Lépine, and M. Vrakking, “*Attosecond control of dissociative ionization of O(2) molecules*”, *Physical Review a* **84** (2011).
- [77] W. Quan, V. V. Serov, M. Wei, M. Zhao, Y. Zhou, Y. Wang, X. Lai, A. S. Kheifets, and X. Liu, “*Attosecond molecular angular streaking with all-ionic fragments detection*”, *Physical Review Letters* **123**, 223204 (2019).
- [78] Z. Tao, C. Chen, T. Szilvási, M. Keller, M. Mavrikakis, H. Kapteyn, and M. Murnane, “*Direct time-domain observation of attosecond final-state lifetimes in photoemission from solids*”, *Science* **353**, 62–67 (2016).
- [79] A. Damascelli, Z. Hussain, and Z.-X. Shen, “*Angle-resolved photoemission studies of the cuprate superconductors*”, *Reviews of Modern Physics* **75**, 473–541 (2003).
- [80] D. Lide, *CRC Handbook of Chemistry and Physics, 89th Edition* (Taylor & Francis, 2008).

- [81] W. Spicer and A. Herrera-Gomez, “*Modern theory and application of photocathodes*”, Proc. SPIE **2022**, 18–33 (1993).
- [82] A. Damascelli, “*Probing the electronic structure of complex systems by ARPES*”, Physica Scripta **T109**, 61 (2004).
- [83] S. Hüfner, *Photoelectron Spectroscopy: Principles and Applications*, Advanced Texts in Physics (Springer, Berlin and Heidelberg, 2003), third revised and enlarged edition ed.
- [84] W. E. Spicer, “*Photoemissive, photoconductive, and optical absorption studies of alkali-antimony compounds*”, Physical Review **112**, 114–122 (1958).
- [85] C. N. Berglund and W. E. Spicer, “*Photoemission studies of copper and silver: Theory*”, Physical Review **136**, A1030–A1044 (1964).
- [86] M. P. Seah and W. A. Dench, “*Quantitative electron spectroscopy of surfaces: A standard data base for electron inelastic mean free paths in solids*”, Surface and Interface Analysis **1**, 2–11 (1979).
- [87] U. Fruehling, M. Wieland, M. Gensch, T. Gebert, B. Schütte, M. Krikunova, R. Kalms, F. Budzyn, O. Grimm, J. Rossbach, E. Plönjes, and M. Drescher, “*Single-shot terahertz-field-driven X-ray streak camera*”, Nature Photonics **3**(2009),523-528 **3** (2009).
- [88] L. V. Keldysh, “*Ionization in the field of a strong electromagnetic wave*”, Soviet Physics JETP **20**, 1307–1314 (1965).
- [89] M. Lewenstein, P. Balcou, M. Y. Ivanov, A. L’Huillier, and P. B. Corkum, “*Theory of high-harmonic generation by low-frequency laser fields*”, Physical Review A **49**, 2117–2132 (1994).
- [90] J. Itatani, F. Quere, G. Yudin, M. Ivanov, F. Krausz, and P. Corkum, “*Attosecond streak camera*”, Physical Review Letters **88**, 173903 (2002).
- [91] M. Kitzler, N. Milosevic, A. Scrinzi, F. Krausz, and T. Brabec, “*Quantum theory of attosecond XUV pulse measurement by laser dressed photoionization*”, Physical Review Letters **88**, 173904 (2002).
- [92] D. J. Kane and R. Trebino, “*Characterization of arbitrary femtosecond pulses using frequency-resolved optical gating*”, IEEE Journal of Quantum Electronics **29**, 571–579 (1993).
- [93] D. J. Kane, “*Recent progress toward real-time measurement of ultrashort laser pulses*”, IEEE Journal of Quantum Electronics **35**, 421–431 (1999).
- [94] Y. Mairesse and F. Quere, “*Frequency-resolved optical gating for complete reconstruction of attosecond bursts*”, Physical Review A **71** (2005).

- 
- [95] P. Eckle, M. Smolarski, P. Schlup, J. Biegert, A. Staudte, M. Schöffler, H. G. Muller, R. Dörner, and U. Keller, “*Attosecond angular streaking*”, *Nature Physics* **4**, 565–570 (2008).
- [96] H. G. Muller, “*Reconstruction of attosecond harmonic beating by interference of two-photon transitions*”, *Applied Physics B* **74**, 17–21 (2002).
- [97] V. Vénier, R. Taïeb, and A. Maquet, “*Phase dependence of  $(N+1)$ -color ( $N>1$ ) IR-UV photoionization of atoms with higher harmonics*”, *Physical Review A* **54**, 721–728 (1996).
- [98] T. E. Glover, R. W. Schoenlein, A. H. Chin, and C. V. Shank, “*Observation of laser assisted photoelectric effect and femtosecond high order harmonic radiation*”, *Physical Review Letters* **76**, 2468–2471 (1996).
- [99] T. Ruchon and A. Camper, “*Notes on attosecond pulse profile measurements with the rabbit technique*”, UVX 2012 - 11e Colloque sur les Sources Coherentes et Incoherentes UV, VUV et X: Applications et Developpements Recents (2013).
- [100] E. P. Wigner, “*Lower limit for the energy derivative of the scattering phase shift*”, *Physical Review* **98**, 145–147 (1955).
- [101] J. Dahlström, D. Guénot, K. Klünder, M. Gisselbrecht, J. Mauritsson, A. L’Huillier, A. Maquet, and R. Taïeb, “*Theory of attosecond delays in laser-assisted photoionization*”, *Chemical Physics* **414**, 53–64 (2013). Attosecond spectroscopy.
- [102] L. Kasmi, M. Lucchini, L. Castiglioni, P. Kliuiev, J. Osterwalder, M. Hengsberger, L. Gallmann, P. Krüger, and U. Keller, “*Effective mass effect in attosecond electron transport*”, *Optica* **4**, 1492–1497 (2017).
- [103] F. Siek, S. Neb, P. Bartz, M. Hensen, C. Strüber, S. Fiechter, M. Torrent-Sucarrat, V. M. Silkin, E. E. Krasovskii, N. M. Kabachnik, S. Fritzsche, R. D. Muiño, P. M. Echenique, A. K. Kazansky, N. Müller, W. Pfeiffer, and U. Heinzmann, “*Angular momentum-induced delays in solid-state photoemission enhanced by intra-atomic interactions*”, *Science* **357**, 1274–1277 (2017).
- [104] M. Swoboda, J. Dahlström, T. Ruchon, P. Johnsson, J. Mauritsson, A. L’Huillier, and K. Schafer, “*Intensity dependence of laser-assisted attosecond photoionization spectra*”, *Laser Physics* **19**, 1591–1599 (2009).
- [105] M. J. Ambrosio and U. Thumm, “*Electronic structure effects in spatiotemporally resolved photoemission interferograms of copper surfaces*”, *Physical Review A* **96**, 051403 (2017).
- [106] L. Cattaneo, J. Vos, M. Lucchini, L. Gallmann, C. Cirelli, and U. Keller, “*Comparison of attosecond streaking and rabbit*”, *Optics Express* **24**, 29060–29076 (2016).

- [107] A. Gebauer, S. Neb, W. Enns, B. Stadtmüller, M. Aeschlimann, and W. Pfeiffer, “*Equivalence of rabbitt and streaking delays in attosecond-time-resolved photoemission spectroscopy at solid surfaces*”, Applied Sciences **9**, 592 (2019).
- [108] J. Schmidt, A. Guggenmos, S. H. Chew, A. Gliserin, M. Högner, M. F. Kling, J. Zou, C. Späth, and U. Kleineberg, “*Development of a 10 kHz high harmonic source up to 140 eV photon energy for ultrafast time-, angle-, and phase-resolved photoelectron emission spectroscopy on solid targets*”, Review of Scientific Instruments **88**, 083105 (2017).
- [109] I. Orfanos, I. Makos, I. Liontos, E. Skantzakis, B. Förg, D. Charalambidis, and P. Tzallas, “*Attosecond pulse metrology*”, APL Photonics **4**, 080901 (2019).
- [110] A. P. Jauho and K. Johnsen, “*Dynamical Franz-Keldysh effect*”, Physical Review Letters **76**, 4576–4579 (1996).
- [111] M. Lucchini, S. A. Sato, A. Ludwig, J. Herrmann, M. Volkov, L. Kasmi, Y. Shinohara, K. Yabana, L. Gallmann, and U. Keller, “*Attosecond dynamical Franz-Keldysh effect in polycrystalline diamond*”, Science **353**, 916–919 (2016).
- [112] A. Schiffrin, T. Paasch-Colberg, N. Karpowicz, V. Apalkov, D. Gerster, S. Muehlbrandt, M. Korbman, J. Reichert, M. Schultze, S. Holzner, J. Barth, R. Kienberger, R. Ernstorfer, V. Yakovlev, M. Stockman, and F. Krausz, “*Optical-field-induced current in dielectrics*”, Nature **493**, 70–74 (2013).
- [113] L.-P. Oloff, M. Oura, K. Rossnagel, A. Chainani, M. Matsunami, R. Eguchi, T. Kiss, Y. Nakatani, T. Yamaguchi, J. Miyawaki, M. Taguchi, K. Yamagami, T. Togashi, T. Katayama, K. Ogawa, M. Yabashi, and T. Ishikawa, “*Time-resolved HAXPES at SACLA: probe and pump pulse-induced space-charge effects*”, New Journal of Physics **16**, 123045 (2014).
- [114] K. T. Kim, D. H. Ko, J. Park, V. Tosa, and C. H. Nam, “*Complete temporal reconstruction of attosecond high-harmonic pulse trains*”, New Journal of Physics **12**, 083019 (2010).
- [115] V. Gruson, L. Barreau, Á. Jiménez-Galan, F. Risoud, J. Caillat, A. Maquet, B. Carré, F. Lepetit, J.-F. Hergott, T. Ruchon, L. Argenti, R. Taïeb, F. Martín, and P. Salières, “*Attosecond dynamics through a fano resonance: Monitoring the birth of a photoelectron*”, Science **354**, 734–738 (2016).
- [116] D. Busto, L. Barreau, M. Isinger, M. Turconi, C. Alexandridi, A. Harth, S. Zhong, R. J. Squibb, D. Kroon, S. Plogmaker, M. Miranda, Á. Jiménez-Galán, L. Argenti, C. L. Arnold, R. Feifel, F. Martín, M. Gisselbrecht, A. L’Huillier, and P. Salières, “*Time–frequency representation of autoionization dynamics in helium*”, Journal of Physics B: Atomic, Molecular and Optical Physics **51**, 044002 (2018).
- [117] H. Wei, T. Morishita, and C. D. Lin, “*Critical evaluation of attosecond time delays retrieved from photoelectron streaking measurements*”, Physical Review A **93**, 053412 (2016).

- 
- [118] S. B. Schoun, R. Chirla, J. Wheeler, C. Roedig, P. Agostini, L. F. DiMauro, K. J. Schafer, and M. B. Gaarde, “*Attosecond pulse shaping around a Cooper minimum*”, *Physical Review Letters* **112**, 153001 (2014).
- [119] W. Heisenberg, “*Über den anschaulichen Inhalt der quantentheoretischen Kinematik und Mechanik*”, *Zeitschrift für Physik* **33**, 879–893 (1925).
- [120] M. I. Stockman, M. F. Kling, U. Kleineberg, and F. Krausz, “*Attosecond nanoplasmonic-field microscope*”, *Nature Photonics* **1**, 539–544 (2007).
- [121] S. H. Chew, F. Süßmann, C. Späth, A. Wirth, J. Schmidt, S. Zherebtsov, A. Guggenmos, A. Oelsner, N. Weber, J. Kapaldo, A. Gliserin, M. I. Stockman, M. F. Kling, and U. Kleineberg, “*Time-of-flight-photoelectron emission microscopy on plasmonic structures using attosecond extreme ultraviolet pulses*”, *Applied Physics Letters* **100**, 051904 (2012).
- [122] T. Fuji, J. Rauschenberger, A. Apolonskiy, V. Yakovlev, G. Tempea, T. Udem, C. Gohle, T. Haensch, W. Lehnert, M. Scherer, and F. Krausz, “*Monolithic carrier-envelope phase-stabilization scheme*”, *Optics letters* **30**, 332–4 (2005).
- [123] T. Saule, S. Holzberger, O. de Vries, M. Plötner, J. Limpert, A. Tünnermann, and I. Pupeza, “*Phase-stable, multi- $\mu\text{J}$  femtosecond pulses from a repetition-rate tunable Ti:Sa-oscillator-seeded Yb-fiber amplifier*”, *Applied Physics B* **123**, 6877 (2017).
- [124] O. de Vries, T. Saule, M. Plötner, F. Lücking, T. Eidam, A. Hoffmann, A. Klenke, S. Hädrich, J. Limpert, S. Holzberger, T. Schreiber, R. Eberhardt, I. Pupeza, and A. Tünnermann, “*Acousto-optic pulse picking scheme with carrier-frequency-to-pulse-repetition-rate synchronization*”, *Optics Express* **23**, 19586–19595 (2015).
- [125] D. Strickland and G. Mourou, “*Compression of amplified chirped optical pulses*”, *Optics Communications* **56**, 219–221 (1985).
- [126] J. Weitenberg, T. Saule, J. Schulte, and P. Russbüldt, “*Nonlinear pulse compression to sub-40 fs at 4.5  $\mu\text{J}$  pulse energy by multi-pass-cell spectral broadening*”, *IEEE Journal of Quantum Electronics* **53**, 1–4 (2017).
- [127] H. Carstens, M. Högner, T. Saule, S. Holzberger, N. Lilienfein, A. Guggenmos, C. Jocher, T. Eidam, D. Esser, V. Tosa, V. Pervak, J. Limpert, A. Tünnermann, U. Kleineberg, F. Krausz, and I. Pupeza, “*High-harmonic generation at 250 MHz with photon energies exceeding 100 eV*”, *Optica* **3**, 366 (2016).
- [128] I. Pupeza, M. Högner, J. Weitenberg, S. Holzberger, D. Esser, T. Eidam, J. Limpert, A. Tünnermann, E. Fill, and V. S. Yakovlev, “*Cavity-enhanced high-harmonic generation with spatially tailored driving fields*”, *Physical Review Letters* **112**, 103902 (2014).

- [129] H. Carstens, S. Holzberger, J. Kaster, J. Weitenberg, V. Pervak, A. Apolonski, E. Fill, F. Krausz, and I. Pupeza, “*Large-mode enhancement cavities*”, *Optics Express* **21**, 11606–11617 (2013).
- [130] R. W. P. Drever, J. L. Hall, F. V. Kowalski, J. Hough, G. M. Ford, A. J. Munley, and H. Ward, “*Laser phase and frequency stabilization using an optical resonator*”, *Applied Physics B* **31**, 97–105 (1983).
- [131] I. Pupeza, X. Gu, E. Fill, T. Eidam, J. Limpert, A. Tünnermann, F. Krausz, and T. Udem, “*Highly sensitive dispersion measurement of a high-power passive optical resonator using spatial-spectral interferometry*”, *Optics Express* **18**, 26184–26195 (2010).
- [132] M. Högner, T. Saule, S. Heinrich, N. Lilienfein, D. Esser, M. Trubetskov, V. Pervak, and I. Pupeza, “*Cavity-enhanced noncollinear high-harmonic generation*”, *Optics Express* **27**, 19675–19691 (2019).
- [133] G. Porat, C. Heyl, S. Schoun, C. Benko, N. Dörre, K. Corwin, and J. Ye, “*Phase-matched extreme-ultraviolet frequency-comb generation*”, *Nature Photonics* **12** (2018).
- [134] D. C. Yost, T. R. Schibli, and J. Ye, “*Efficient output coupling of intracavity high-harmonic generation*”, *Optics Letters* **33**, 1099 (2008).
- [135] C. Zhang, S. B. Schoun, C. M. Heyl, G. Porat, M. B. Gaarde, and J. Ye, “*Noncollinear enhancement cavity for record-high out-coupling efficiency of an extreme-UV frequency comb*”, *Physical Review Letters* **125**, 093902 (2020).
- [136] K. D. Moll, R. J. Jones, and J. Ye, “*Output coupling methods for cavity-based high-harmonic generation*”, *Optics Express* **14**, 8189 (2006).
- [137] M. Högner, T. Saule, and I. Pupeza, “*Efficiency of cavity-enhanced high harmonic generation with geometric output coupling*”, *Journal of Physics B: Atomic, Molecular and Optical Physics* **52** (2019).
- [138] D. Esser, J. Weitenberg, W. Bröring, I. Pupeza, S. Holzberger, and H.-D. Hoffmann, “*Laser-manufactured mirrors for geometrical output coupling of intracavity-generated high harmonics*”, *Optics Express* **21**, 26797–26805 (2013).
- [139] E. Takahashi, Y. Nabekawa, and K. Midorikawa, “*Generation of 10- $\mu$ J coherent extreme-ultraviolet light by use of high-order harmonics*”, *Optics Letters* **27**, 1920 (2002).
- [140] E. J. Takahashi, Y. Nabekawa, and K. Midorikawa, “*Low-divergence coherent soft X-ray source at 13 nm by high-order harmonics*”, *Applied Physics Letters* **84**, 4–6 (2004).
- [141] D. Popmintchev, C. Hernández-García, F. Dollar, C. Mancuso, J. A. Pérez-Hernández, M.-C. Chen, A. Hankla, X. Gao, B. Shim, A. L. Gaeta, M. Tarazkar, D. A. Romanov, R. J. Levis, J. A. Gaffney, M. Ford, S. B. Libby, A. Jaron-Becker, A. Becker, L. Plaja, M. M.

- 
- Murnane, H. C. Kapteyn, and T. Popmintchev, “*Ultraviolet surprise: Efficient soft X-ray high-harmonic generation in multiply ionized plasmas*”, *Science* **350**, 1225–1231 (2015).
- [142] A. Mikkelsen, J. Schwenke, T. Fordell, G. Luo, K. Klünder, E. Hilner, N. Anttu, A. A. Zakharov, E. Lundgren, J. Mauritsson, J. N. Andersen, H. Q. Xu, and A. L’Huillier, “*Photoemission electron microscopy using extreme ultraviolet attosecond pulse trains*”, *Review of Scientific Instruments* **80**, 123703 (2009).
- [143] G. L. Dakovski, Y. Li, T. Durakiewicz, and G. Rodriguez, “*Tunable ultrafast extreme ultraviolet source for time- and angle-resolved photoemission spectroscopy*”, *Review of Scientific Instruments* **81**, 073108 (2010).
- [144] B. Frietsch, R. Carley, K. Döbrich, C. Gahl, M. Teichmann, O. Schwarzkopf, P. Wernet, and M. Weinelt, “*A high-order harmonic generation apparatus for time- and angle-resolved photoelectron spectroscopy*”, *Review of Scientific Instruments* **84**, 075106 (2013).
- [145] H. Wang, Y. Xu, S. Ulonska, J. S. Robinson, P. Ranitovic, and R. A. Kaindl, “*Bright high-repetition-rate source of narrowband extreme-ultraviolet harmonics beyond 22 eV*”, *Nature Communications* **6**, 7459 (2015).
- [146] J. Rothhardt, S. Hädrich, A. Klenke, S. Demmler, A. Hoffmann, T. Gotschall, T. Eidam, M. Krebs, J. Limpert, and A. Tünnermann, “*53 W average power few-cycle fiber laser system generating soft X-rays up to the water window*”, *Optics Letters* **39**, 5224–5227 (2014).
- [147] S. Hädrich, A. Klenke, J. Rothhardt, M. Krebs, A. Hoffmann, O. Pronin, V. Pervak, J. Limpert, and A. Tünnermann, “*High photon flux table-top coherent extreme-ultraviolet source*”, *Nature Photonics* **8**, 779–783 (2014).
- [148] C.-T. Chiang, M. Huth, A. Trützscher, M. Kiel, F. O. Schumann, J. Kirschner, and W. Widra, “*Boosting laboratory photoelectron spectroscopy by megahertz high-order harmonics*”, *New Journal of Physics* **17**, 013035 (2015).
- [149] S. Hädrich, M. Krebs, A. Hoffmann, A. Klenke, J. Rothhardt, J. Limpert, and A. Tünnermann, “*Exploring new avenues in high repetition rate table-top coherent extreme ultraviolet sources*”, *Light: Science & Applications* **4**, e320 (2015).
- [150] A. Ozawa, Z. Zhao, M. Kuwata-Gonokami, and Y. Kobayashi, “*High average power coherent vuv generation at 10 MHz repetition frequency by intracavity high harmonic generation*”, *Optics Express* **23**, 15107–15118 (2015).
- [151] A. K. Mills, S. Zhdanovich, A. Sheyerman, G. Levy, A. Damascelli, and D. J. Jones, “*An XUV source using a femtosecond enhancement cavity for photoemission spectroscopy*”, p. 95121I (2015).

- [152] C. Corder, P. Zhao, J. Bakalis, X. Li, M. D. Kershis, A. R. Muraca, M. G. White, and T. K. Allison, “*Ultrafast extreme ultraviolet photoemission without space charge*”, *Structural Dynamics* **5**, 054301 (2018).
- [153] W. Pupp and H. Hartmann, *Vakuumtechnik - Grundlagen und Anwendungen* (Hanser, München, 1991).
- [154] B. L. Henke, E. M. Gullikson, and J. C. Davis, “*X-ray interactions: Photoabsorption, scattering, transmission, and reflection at  $E = 50\text{-}30,000$  eV,  $Z = 1\text{-}92$* ”, *Atomic Data and Nuclear Data Tables* **54**, 181–342 (1993).
- [155] J. Schmidt, “*Development of an advanced 10 khz high harmonic source and its application to angle- and phase-resolved photoelectron streaking spectroscopy*”, Ph.D. thesis, Ludwig-Maximilians-Universität München (2017).
- [156] A. Technologies, *Laser and Optics User’s Manual* (Agilent Technologies, Santa Clara, California, 2007).
- [157] C. Krüger, J. Fuchs, L. Cattaneo, and U. Keller, “*Attosecond resolution from free running interferometric measurements*”, *Optics Express* **28**, 12862–12871 (2020).
- [158] O. Jagutzki, V. Mergel, K. Ullmann-Pfleger, L. Spielberger, U. Spillmann, R. Dörner, and H. Schmidt-Böcking, “*A broad-application microchannel-plate detector system for advanced particle or photon detection tasks: large area imaging, precise multi-hit timing information and high detection rate*”, *Nuclear Instruments and Methods in Physics Research Section A: Accelerators, Spectrometers, Detectors and Associated Equipment* **477**, 244 – 249 (2002). 5th Int. Conf. on Position-Sensitive Detectors.
- [159] K. Zakeri, T. Peixoto, Y. Zhang, J. Prokop, and J. Kirschner, “*On the preparation of clean tungsten single crystals*”, *Surface Science* **604**, L1 – L3 (2010).
- [160] M. A. Ordal, R. J. Bell, R. W. Alexander, L. A. Newquist, and M. R. Querry, “*Optical properties of Al, Fe, Ti, Ta, W, and Mo at submillimeter wavelengths*”, *Applied Optics* **27**, 1203–1209 (1988).
- [161] M. Högner, T. Saule, and I. Pupeza, “*Efficiency of cavity-enhanced high harmonic generation with geometric output coupling*”, *Journal of Physics B: Atomic, Molecular and Optical Physics* **52** (2019).
- [162] A. Guggenmos, M. Hofstetter, R. Rauhut, B. Nickel, E. Gullikson, and U. Kleineberg, “*Aperiodic multilayer mirrors for attosecond soft X-ray pulses*”, *Proc. SPIE Advances in X-Ray/EUV Optics and Components VII* **8502**, 850204 (2012).
- [163] S. Heinrich, T. Saule, M. Högner, Y. Cui, V. S. Yakovlev, I. Pupeza, and U. Kleineberg, “*Attosecond intra-valence band dynamics and resonant-photoemission delays in  $W(110)$* ”, Manuscript submitted for publication (2021).

- 
- [164] A. Harth, N. Douguet, K. Bartschat, R. Moshhammer, and T. Pfeifer, “*Extracting phase information on continuum-continuum couplings*”, *Physical Review A* **99**, 023410 (2019).
- [165] Y. Yang, F. Wang, C. Li, K. Liu, F. Tang, Q. Tu, X. Zhang, Z. Wang, M. Qin, and Q. Liao, “*Few-photon absorption and emission in the laser-assisted single photoionization*”, *Optics Communications* **475**, 126221 (2020).
- [166] A. Jain, T. Gaumnitz, A. Bray, A. Kheifets, and H. J. Wörner, “*Photoionization delays in xenon using single-shot referencing in the collinear back-focusing geometry*”, *Optics Letters* **43**, 4510–4513 (2018).
- [167] J. P. Long, B. S. Itchkawitz, and M. N. Kabler, “*Photoelectron spectroscopy of laser-excited surfaces by synchrotron radiation*”, *Journal of the Optical Society of America B* **13**, 201 (1996).
- [168] S. Kowalczyk, L. Ley, R. Pollak, and D. Shirley, “*High-resolution XPS spectra of Ir, Pt and Au valence bands*”, *Physics Letters A* **41**, 455 – 456 (1972).
- [169] T. Saule, M. Högner, N. Lilienfein, O. de Vries, M. Plötner, V. S. Yakovlev, N. Karpowicz, J. Limpert, and I. Pupeza, “*Cumulative plasma effects in cavity-enhanced high-order harmonic generation in gases*”, *APL Photonics* **3**, 101301 (2018).
- [170] P. Giannozzi, S. Baroni, N. Bonini, M. Calandra, R. Car, C. Cavazzoni, D. Ceresoli, G. L. Chiarotti, M. Cococcioni, I. Dabo, A. D. Corso, S. de Gironcoli, S. Fabris, G. Fratesi, R. Gebauer, U. Gerstmann, C. Gougoussis, A. Kokalj, M. Lazzeri, L. Martin-Samos, N. Marzari, F. Mauri, R. Mazzarello, S. Paolini, A. Pasquarello, L. Paulatto, C. Sbraccia, S. Scandolo, G. Sclauzero, A. P. Seitsonen, A. Smogunov, P. Umari, and R. M. Wentzcovitch, “*QUANTUM ESPRESSO: a modular and open-source software project for quantum simulations of materials*”, *Journal of Physics: Condensed Matter* **21**, 395502 (2009).
- [171] B. N. Dutta and B. Dayal, “*Lattice constants and thermal expansion of palladium and tungsten up to 878 °C by X-Ray method*”, *Physica Status Solidi (b)* **3**, 2253–2259 (1963).
- [172] N. E. Christensen and B. Feuerbacher, “*Volume and surface photoemission from tungsten. I. calculation of band structure and emission spectra*”, *Physical Review B* **10**, 2349–2372 (1974).
- [173] A. Aharony and O. Entin-Wohlman, *Introduction to Solid State Physics* (World Scientific Publishing, Singapore, 2018).
- [174] N. Lilienfein, C. Hofer, M. Högner, T. Saule, M. Trubetskov, V. Pervak, E. Fill, C. Riek, A. Leitenstorfer, J. Limpert, F. Krausz, and I. Pupeza, “*Temporal solitons in free-space femtosecond enhancement cavities*”, *Nature Photonics* **13** (2019).
- [175] V. S. Yakovlev and N. Karpowicz, “*Angular momentum can slow down photoemission*”, *Science* **357**, 1239–1240 (2017).

- [176] U. Bovensiepen and M. Ligges, “*Timing photoemission—final state matters*”, *Science* **353**, 28–29 (2016).
- [177] H. Shinotsuka, S. Tanuma, C. J. Powell, and D. R. Penn, “*Calculations of electron inelastic mean free paths. XII. data for 42 inorganic compounds over the 50 eV to 200 keV range with the full Penn algorithm*”, *Surface and Interface Analysis* **51**, 427–457 (2019).
- [178] S. Neppel, R. Ernstorfer, E. M. Bothschafter, A. L. Cavalieri, D. Menzel, J. V. Barth, F. Krausz, R. Kienberger, and P. Feulner, “*Attosecond time-resolved photoemission from core and valence states of magnesium*”, *Physical Review Letters* **109**, 087401 (2012).
- [179] A. Thompson, *X-ray Data Booklet* (Lawrence Berkeley National Laboratory, University of California, Berkeley, California, 2009).
- [180] R. J. Colton and J. W. Rabalais, “*Electronic structure of tungsten and some of its borides, carbides, nitrides, and oxides by X-ray electron spectroscopy*”, *Inorganic Chemistry* **15**, 236–238 (1976).
- [181] R. Strayer, W. Mackie, and L. Swanson, “*Work function measurements by field-emission retarding potential method*”, *Surface Science* **34** (1973).
- [182] C. Chen, Z. Tao, A. Carr, P. Matyba, T. Szilvási, S. Emmerich, M. Piecuch, M. Keller, D. Zusin, S. Eich, M. Rollinger, W. You, S. Mathias, U. Thumm, M. Mavrikakis, M. Aeschlimann, P. M. Oppeneer, H. Kapteyn, and M. M. Murnane, “*Distinguishing attosecond electron-electron scattering and screening in transition metals*”, *Proceedings of the National Academy of Sciences of the United States of America* **114**, E5300–E5307 (2017).
- [183] J. P. Perdew, W. Yang, K. Burke, Z. Yang, E. K. U. Gross, M. Scheffler, G. E. Scuseria, T. M. Henderson, I. Y. Zhang, A. Ruzsinszky, H. Peng, J. Sun, E. Trushin, and A. Görling, “*Understanding band gaps of solids in generalized Kohn–Sham theory*”, *Proceedings of the National Academy of Sciences* **114**, 2801–2806 (2017).
- [184] W. Demtröder, *Experimentalphysik 3: Atome, Moleküle und Festkörper; 3rd ed.*, Springer-lehrbuch (Springer, Berlin, 2005).
- [185] I. Jordan and H. J. Wörner, “*Extracting attosecond delays from spectrally overlapping interferograms*”, *Journal of Optics* **20** (2017).
- [186] A. Katrib, F. Hemming, P. Wehrer, L. Hilaire, and G. Maire, “*The multi-surface structure and catalytic properties of partially reduced WO<sub>3</sub>, WO<sub>2</sub> and WC + O<sub>2</sub> or W + O<sub>2</sub> as characterized by xps*”, *Journal of Electron Spectroscopy and Related Phenomena* **76**, 195 – 200 (1995). *Proceedings of the Sixth International Conference on Electron Spectroscopy.*
- [187] R. Koc and S. Kodambaka, “*Tungsten carbide (WC) synthesis from novel precursors*”, *Journal of the European Ceramic Society* **20**, 1859–1869 (2000).

- [188] A. S. Kurlov and A. I. Gusev, *Tungsten Carbides - Structure, Properties and Application in Hardmetals* (Springer Science and Business Media, Berlin, Heidelberg, 2013).



# Danksagung

Mein Dank gilt zuerst Professor Ulf Kleineberg und Professor Ferenc Krausz dafür, mir die Möglichkeit gegeben zu haben, an LMU und MPQ diese Doktorarbeit durchzuführen unter den hervorragenden Bedingungen, die diese Einrichtungen auszeichnet. Die Betreuung von Prof. Kleineberg gab mir gleichermaßen Unterstützung und Freiraum, um selbstständig zu arbeiten, Verantwortung zu übernehmen, Studenten zu betreuen, Projekte zu planen und umzusetzen und Ergebnisse zu präsentieren. Auch Ioachim Pupeza war mit seiner Passion für das MEGAS-Projekt, seiner Energie und seinen Anregungen eine große Hilfe bei dieser Arbeit.

Für die gute Arbeitsatmosphäre und stetige Hilfsbereitschaft, viele unterhaltsame gemeinsame Stunden und hilfreiche Diskussionen und Ratschläge im Laufe meiner Promotion bedanke ich mich ganz herzlich bei den vielen Freunden und Kollegen vom Coulombwall. Zur Entstehung dieser Arbeit haben dabei besonders Christina, Domi, Johannes, Maxi, Niko, Philipp, Tobi und Yang beigetragen.

Ein herzliches Dankeschön geht zudem an Klaus und Katha aus der LMU-Verwaltung sowie an das Team der mechanischen Werkstatt und ihren Leiter Rolf für die jahrelange angenehme, unkomplizierte und reibungslose Zusammenarbeit.

Die Einführung in das kleine Einmaleins der Laserphysik und Photoelektronenspektroskopie verdanke ich Jürgen, der auch in stressigen Zeiten stets ein offenes Ohr und einen hilfreichen Rat für mich parat hatte. Danke auch an Alex und Yang, die mich mit XUV-Spiegeln versorgt haben und auf deren Hilfsbereitschaft und Expertise ich auch darüber hinaus jederzeit zählen konnte. Mit seiner angenehmen, ruhigen und kollegialen Art war Maxi immer ein höchst willkommener Labor- und Diskussionspartner mit profundem Verständnis für alle Themen von Leberwurst bis intra-cavity HHG.

Ein riesiges Dankeschön geht an Tobi, dessen Können und Wissen maßgeblich zum Erfolg dieser Arbeit beigetragen haben und dessen unerschöpfliche Energie, gute Laune und hervorragender Musikgeschmack es schafften, die vielen gemeinsamen Stunden im Labor kurzweilig werden zu lassen.

Mein persönlicher Dank gilt zudem meiner Familie, die mich auf meinem gesamten bisherigen Weg jederzeit und selbstverständlich unterstützt hat, ganz besonders meiner Mutter und meiner Ines.